VILNIUS UNIVERSITY CENTER FOR PHYSICAL SCIENCES AND TECHNOLOGY

Miglė Mackevičiūtė

Efficient and Fast Glass Cutting Using Laser Bursts

DOCTORAL DISSERTATION

Technological Sciences, Material Engineering (T 008)

VILNIUS 2025

The dissertation was prepared between 2021 and 2025 at the Center for Physical Sciences and Technology. The research was partly supported by the Research Council of Lithuania.

Academic supervisor – Dr. Paulius Gečys (Center for Physical Sciences and Technology, Technological Sciences, Materials Engineering, T 008).

This doctoral dissertation will be defended in a public/closed meeting of the Dissertation Defence Panel:

Chairman – Prof. Dr. Domas Paipulas (Vilnius University, Natural Sciences, Physics, N 002).

Members:

Dr. Martynas Beresna (University of Southampton, Technological Sciences, Materials Engineering, T 008),

Assoc. Prof. Dr. Vytautas Jukna (Vilnius University, Natural Sciences, Physics, N 002),

Dr. Evaldas Stankevičius (Center for Physical Sciences and Technology, Natural Sciences, Physics, N 002),

Prof. Dr. Tomas Tamulevičius (Kaunas University of Technology, Technological Sciences, Materials Engineering, T 008).

The dissertation shall be defended at a public/closed meeting of the Dissertation Defence Panel at 11:00 on 24th of October 2025 in the meeting room of the Physics Institute.

Address: Savanorių Ave. 231, 02300 Vilnius, Lithuania

Tel. +370 645 15557; e-mail: office@ftmc.lt

The text of this dissertation can be accessed at the Vilnius University Library, as well as on the website of Vilnius University:

www.vu.lt/lt/naujienos/ivykiu-kalendorius

VILNIAUS UNIVERSITETAS FIZINIŲ IR TECHNOLOGIJOS MOKSLŲ CENTRAS

Miglė Mackevičiūtė

Efektyvus ir greitas stiklo pjovimas lazeriu panaudojant papliūpų režimą

DAKTARO DISERTACIJA

Technologijos mokslai, Medžiagų inžinerija (T 008)

VILNIUS 2025

Disertacija rengta 2021–2025 metais studijuojant doktorantūroje Fizinių ir technologijos mokslų centre, Lazerinių technologijų skyriuje, Lazerinio mikroapdirbimo technologijų laboratorijoje. Mokslinius tyrimus dalinai rėmė Lietuvos mokslo taryba.

Mokslinis vadovas – dr. Paulius Gečys (Fizinių ir technologijos mokslų centras, technologijos mokslai, medžiagų inžinerija, T008).

Gynimo taryba:

Pirmininkas – prof. dr. Domas Paipulas (Vilniaus universitetas, gamtos mokslai, fizika, N 002).

Nariai:

dr. Martynas Beresna (Sautamptono universitetas, Jungtinė Karalystė, technologijos mokslai, medžiagų inžinerija, T 008),

doc. dr. Vytautas Jukna (Vilniaus universitetas, gamtos mokslai, fizika, N 002),

dr. Evaldas Stankevičius (Fizinių ir technologijos mokslų centras, gamtos mokslai, fizika, N 002),

prof. dr. Tomas Tamulevičius (Kauno technologijos universitetas, technologijos mokslai, medžiagų inžinerija, T 008).

Disertacija ginama viešame Gynimo tarybos posėdyje 2025 m. spalio mėn. 24 d. 11 val. FTMC Fizikos instituto salėje. Adresas: Savanorių pr. 231, 02300 Vilnius, Lietuva, tel. +370 645 15557; el. paštas: office@ftmc.lt

Disertaciją galima peržiūrėti Vilniaus universiteto bibliotekoje ir VU interneto svetainėje adresu:

https://www.vu.lt/naujienos/ivvkiu-kalendoriu

ABBREVIATIONS

a.u. Arbitrary Units

BiBurst Burst-in-a-Burst Regime

BS Borosilicate

BUC Bottom-Up Cutting

DOE Diffractive Optical Element

FS Fused Silica

FWHM Full Width at Half Maximum

MF Multifilamentation
NA Numerical Aperture
OM Optical Microscope
OP Optical Profilometer

PMMA Poly-Methyl Methacrylate SEM Scanning Electron Microscope

SLG Soda-Lime Glass

SLM Spatial Light Modulator TDC Top-Down Cutting

WATDC Water-Assisted Top-Down Cutting

TABLE OF CONTENTS

INTR	ODUC	CTION	9
THE	AIM A	AND RESEARCH OBJECTIVES OF THE THESIS	10
PRAC	CTICA	L VALUE AND NOVELTY	10
STAT	ГЕМЕ	NTS TO DEFEND	11
APPR	ROBA	ΓΙΟΝ	11
AUTI	HOR'S	CONTRIBUTION	15
CO-A	UTHO	DR'S CONTRIBUTION	15
1.	LITE	RATURE OVERVIEW	16
	1.1.	Light absorption	16
	1.2.	Laser-induced material damage	18
	1.3.	Fused silica and soda-lime glass	19
	1.4.	Beam propagation	20
		1.4.1. Gaussian beam	20
		1.4.2. Filamentation via self-focusing	22
		1.4.3. Bessel beam	25
	1.5.	Mechanical glass cutting	26
	1.6.	Laser-based glass cutting	29
		1.6.1. Controlled fracture	29
		1.6.2. Laser scribe and break	30
		1.6.3. Top-down cutting	33
		1.6.4. Bottom-up cutting	35
	1.7.	Comparison of the cutting methods	36
	1.8.	Burst mode	40
	1.9.	Polarization-related effects	43
2.		ERIMENTAL METHODS AND CHARACTERIZATION	17
IEC		JES	
	2.1.	Laser microprocessing setup	4 /

		2.1.1. Laser sources	. 48
		2.1.2. Beam characterization	. 51
	2.2.	Laser processing methods	. 52
		2.2.1. Bottom-up cutting approach	. 52
		2.2.1.1. Chamfer formation	. 53
		2.2.2. Modifications formation via single-shot	. 54
		2.2.3. Laser scribing and separation	. 55
		2.2.3.1. Separation stress simulation	. 56
	2.3.	Characterization methods	. 57
		2.3.1. Sample quality	. 57
		2.3.2. Process productivity	. 57
		2.3.3. Evaluation of single-shot modifications	. 59
		2.3.4. Characterization tools	. 60
3.	BOT	BOTTOM-UP CUTTING	
	3.1.	Cutting results	. 62
	3.2.	Cutting with variable parameters	. 67
	3.3.	Applications	. 69
	3.4.	Subtractive laser glass cutting overview	. 71
	3.5.	Summary	. 73
4.	SING	SLE-SHOT MODIFICATIONS	. 75
	4.1.	Longitudinal modifications	. 75
		4.1.1. Longitudinal length	. 76
		4.1.2. Modification position	. 80
	4.2.	Transverse modifications	. 83
		4.2.1. Polarization	. 84
		4.2.2. Burst parameters	. 89
	4.3.	Summary	. 95
5.	SOD	A-LIME GLASS SCRIBING	. 98
	5.1.	Single-pass scribing	. 98
		5.1.1. Scanning speed and pulse duration	. 99

	5.1.2. Focus position	104	
5.2.	Double-pass scribing	106	
5.3.	Comparison of different glass cutting methods	111	
5.4.	Summary	113	
MAIN RES	SULTS AND CONCLUSION	115	
REFEREN	CES	117	
SANTRAU	KA	134	
PADĖKA		147	
CURRICULUM VITAE14			

INTRODUCTION

Due to its optical transparency, mechanical strength, thermal and chemical stability, and electrical insulating properties, glass is indispensable for architecture, medicine, communication, technology, and other industries [1]. Prior to integration into functional systems, glass needs to be processed. However, the brittleness of glass complicates the machining process [2,3].

The most established way of cutting glass is the mechanical scribe and break, which offers rapid, cost-effective, and kerf-free separation of samples [4]. Despite this, the conventional method is limited to simple contours, results in tool wear and large edge chippings. Alternative mechanical methods, such as wire sawing and waterjet cutting, are suitable for processing complex geometries but are relatively slower. Precision, high quality, speed, and complex geometries can be achieved by cutting glass with lasers.

Laser cutting is typically performed using a top-down cutting (TDC) approach, where the beam is focused on the top surface of the sample, and the material is removed downwards. However, alternative methods can be applied to glasses that are optically transparent to the wavelength of the laser source. High-intensity pulses focused to a micrometer-sized spot induce nonlinear absorption within a localized volume, and by shifting the focal position, the material can be damaged at various depths. Therefore, glasses can be machined with the beam focused to the bottom surface and the material removed upwards. Bottom-up cutting (BUC) is more efficient than TDC and allows for the creation of straight walls [5]. Alternatively, glass can be scribed by forming volumetric elongated modifications using Bessel beams or filamentation. Although limited to simple contours, the laser scribe and break technique allows for reaching scribing speeds of m/s [6].

Laser machining technology is advancing due to developments in ultrashort laser sources. One of which is the MHz and GHz burst and burst-in-a-burst mode operation, which has been shown to improve the machining of metals [7,8], semiconductors [9,10], polymers [11,12], and dielectrics [13,14]. Most works use the classical top-down approach. However, there is a lack of studies investigating the impact of burst mode on the BUC of glass, volumetric modification formation via self-focusing, and filament-scribing.

In this work, we explored the laser burst modes for glass processing using a low numerical aperture (NA) system. The work is performed using a fast beam scanning system consisting of galvanoscanners and a telecentric f-theta lens. In the first part, we developed ultrashort laser burst mode BUC technology and optimized the process parameters for rapid and efficient sodalime glass (SLG) processing. The results were compared to subtractive laser glass-cutting studies, including TDC, water-assisted top-down cutting (WATDC), and BUC. Furthermore, extensive cutting capabilities were demonstrated. In the second part, the burst and burst-in-a-burst (BiBurst) modes were used to form modifications inside the fused silica (FS) and SLG via self-focusing. We examined the impact of laser parameters on the modification longitudinal length and position, as well as the transverse length and its angle. In the third part, the modifications formed via self-focusing using the BiBurst regime were applied to scribe 1.1 mm-thick SLG samples. To the best of our knowledge, we demonstrated the fastest scribing speed recorded to date.

THE AIM AND RESEARCH OBJECTIVES OF THE THESIS

This work aimed to investigate the impact of laser burst mode on bottom-up cutting of glass, filament-induced volumetric modifications, and its application in scribing. The objectives of the research were to (i) develop laser bottom-up cutting technology for the highest throughput of soda-lime glass processing using bursts; (ii) evaluate the influence of laser burst parameters on filament-induced single-shot modifications in fused silica and soda-lime glass; (iii) investigate the scribing and separation of 1.1 mm-thick soda-lime glass using filament-induced polarization-controlled cracks.

PRACTICAL VALUE AND NOVELTY

A novel implementation of the bottom-up cutting approach for soda-lime glass, using the GHz burst regime, was investigated. The bottom-up cutting with $\lambda=1030$ nm, GHz bursts of picosecond pulses was over an order of magnitude more efficient compared to the studies using the classical top-down approach with a single-pulse regime. The high efficiency was achieved due to the material being removed via cracking, indicated by the μ m-sized ablation products. The bottom-up cutting with GHz bursts was of similar efficiency to that achieved using nanosecond pulses at 532 nm wavelength. However, operating at the fundamental wavelength of the laser is more advantageous, as it allows exploiting the full power of the laser without the need for harmonic conversion and avoids the risk of nonlinear crystal damage, thereby enhancing system reliability.

Variable process parameter fabrication was demonstrated and validated for glass cutting. By adjusting the number of pulses per burst, it was possible to combine high-throughput and high-quality processing for the same workpiece.

Volumetric single-shot modifications with cracks were formed in fused silica and soda-lime glasses using low focusing conditions (NA ~0.04) and laser bursts. A novel method for controlling the direction of cracks via laser polarization was established and applied to scribe 1.1 mm-thick soda-lime glass. The distance between the modifications and, thus, the scribing speed were increased by aligning the cracks along the scribing line. Stable separation of samples scribed at speeds of up to 10 m/s was achieved using a galvanoscanner and a telecentric f-theta lens system. To the best of our knowledge, we demonstrated the fastest scribing speed recorded to date.

STATEMENTS TO DEFEND

- 1. Soda-lime glass can be efficiently processed with GHz laser bursts of picosecond pulses while maintaining high surface quality by employing a bottom-up cutting approach with a higher number of pulses per burst to induce controlled cracking in the bulk, combined with the use of fewer pulses per burst near the top and bottom surfaces to achieve precise ablation.
- 2. Ultrashort laser filamentation using burst (GHz or MHz) and burst-in-a-burst regimes under weak focusing conditions (NA ~0.04) can create elongated volumetric modifications in fused silica (<1.4 mm) and sodalime glass (<0.9 mm), featuring polarization-controlled transverse cracks.
- 3. Deflection of a weakly focused laser beam using galvanometer scanners and a burst-in-a-burst laser regime for filamentation-induced elongated volumetric modifications, with the polarization-determined transverse orientation set along the scanning direction, enables high-speed (up to 10 m/s) single-pass scribing of 1.1 mm-thick soda-lime glass.

APPROBATION

The main results of the research stated in this thesis were published in 3 scientific peer-reviewed papers [A1–A3] and presented at 5 international conferences [D1–D5].

Scientific papers directly related to the thesis (peer-reviewed and indexed in Clarivate Analytics Web of Science (WoS)):

- A1. **M. Mackevičiūtė**, A. Kondratas, J. Dudutis, and P. Gečys, "Ultrafast soda-lime glass scribing via self-filamentation of laser bursts," J. Manuf. Process. **150**(April), 740–750 (2025).
- A2. **M. Mackevičiūtė**, J. Dudutis, and P. Gečys, "A comparative study on MHz and GHz bursts addressing the polarization-based control of laser-induced modifications in fused silica," Opt. Laser Technol. **181**(September 2024), 111289 (2025).
- A3. **M. Mackevičiūtė**, J. Dudutis, and P. Gečys, "Fast and efficient bottom-up cutting of soda-lime glass using GHz bursts of short laser pulses," Opt. Lasers Eng. **183**(May), 108490 (2024).

Other scientific papers (peer-reviewed and indexed in Clarivate Analytics Web of Science (WoS)):

- B1. J. Monzac, S. Smartsev, J. Huijts, L. Rovige, I. A. Andriyash, A. Vernier, V. Tomkus, V. Girdauskas, G. Raciukaitis, M. Mackevičiūtė, V. Stankevic, A. Cavagna, J. Kaur, A. Kalouguine, R. Lopez-Martens, and J. Faure, "Differential pumping for kHz operation of a laser wakefield accelerator based on a continuously flowing hydrogen gas jet," Rev. Sci. Instrum. 96, (2025).
- B2. L. Martelli, O. Kononenko, I. A. Andriyash, J. Wheeler, J. Gautier, J.-P. Goddet, A. Tafzi, R. Lahaye, C. Giaccaglia, A. Flacco, V. Tomkus, M. Mackevičiūtė, J. Dudutis, V. Stankevic, P. Gečys, G. Račiukaitis, H. Kraft, X. Q. Dinh, and C. Thaury, "Physics of high-charge laser-plasma accelerators for few-MeV applications," Phys. Rev. Appl. 23, 034033 (2025).
- B3. J. Monzac, S. Smartsev, J. Huijts, L. Rovige, I. A. Andriyash, A. Vernier, V. Tomkus, V. Girdauskas, G. Raciukaitis, M. Mackevičiūtė, V. Stankevic, A. Cavagna, J. Kaur, A. Kalouguine, R. Lopez-Martens, and J. Faure, "Optical ionization effects in kHz laser wakefield acceleration with few-cycle pulses," Phys. Rev. Res. 6(4), 043099 (2024).

- B4. V. Tomkus, **M. Mackevičiūtė**, J. Dudutis, V. Girdauskas, M. Abedi-Varaki, P. Gečys, and G. Račiukaitis, "Laser-machined two-stage nozzle optimised for laser wakefield acceleration," J. Plasma Phys. **90**(1), 1–11 (2024).
- B5. J. L. Henares, P. Puyuelo-Valdes, C. Salgado-López, J. I. Apiñaniz, P. Bradford, F. Consoli, D. de Luis, M. Ehret, F. Hannachi, R. Hernández-Martín, A. Huber, L. Lancia, M. Mackeviciute, A. Maitrallain, J.-R. Marquès, J. A. Pérez-Hernández, C. Santos, J. J. Santos, V. Stankevic, M. Tarisien, V. Tomkus, L. Volpe, and G. Gatti, "Proton and helium ions acceleration in near-critical density gas targets by short-pulse Ti:Sa PW-class laser," J. Plasma Phys. 89(6), 1–14 (2023).
- B6. J. Dudutis, **M. Mackevičiūtė**, J. Pipiras, R. Stonys, V. Stankevič, G. Račiukaitis, P. Gečys, Transversal and axial modulation of axicongenerated Bessel beams using amplitude and phase masks for glass processing applications, Opt. Express, **30**(2), 1860-1874 (2022).

Other scientific papers (conference proceedings)

C1. U. Chaulagain, S. Karatodorov, M. Raclavsky, S. Lorenz, M. Lamac, M. Albrecht, V. Tomkus, J. Dudutis, **M. Mackevičiūtė**, P. Gečys, and J. Nejdl, "Tomographic characterization of gas jets for laser-plasma acceleration with increased sensitivity," in *International Conference on X-Ray Lasers 2020*, D. Bleiner, ed. (SPIE, 2021), (July), p. 9.

International conference presentations (presenter underlined)

- D1. M. Mackevičiūtė, J. Dudutis, P. Gečys, Soda-lime glass machining with GHz bursts using a bottom-up technique, 17th International Conference on Laser Ablation (COLA2024), Crete, Greece, September 29–October 4 (2024). Poster.
- D2. M. Mackevičiūtė, J. Dudutis, P. Gečys, Efficient bottom-up laser cutting of soda-lime glass using GHz bursts, 25th International Symposium on Laser Precision Microfabrication (LPM2024), San Sebastian, Spain, June 11–14 (2024). Oral.
- D3. M. Mackevičiūtė, J. Dudutis, P. Gečys, Investigation of single-shot intra-volume modifications in fused silica formed using GHz and MHz

- laser bursts, Lasers in Manufacturing conference (LiM 2023), Munchen, Germany, June 26–29 (2023). Oral.
- D4. M. Mackevičiūtė, J. Dudutis, P. Gečys, MHz and GHz laser burst modes for intra-volume glass modification, 24th International Symposium on Laser Precision Microfabrication (LPM2023), Hirosaki, Aomori, Japan, June 13–16 (2023). Oral.
- D5. M. Mackevičiūtė, J. Dudutis, L. Zubauskas, E. Daknys, E. Markauskas, R. Gvozdaitė, G. Račiukaitis, P. Gečys, Quality and flexural strength of laser-cut glass, 23rd International Symposium on Laser Precision Microfabrication (LPM2022), Dresden, Germany, June 7–10 (2022). Poster.

Other presentations (presenter underlined)

- E1. M. Mackevičiūtė, J. Dudutis, P. Gečys, Soda-lime stiklo apdirbimas lazeriu nuo apatinės bandinio pusės pasitelkiant GHz papliupų režimą, 14th Conference of Doctoral Students and Young Scientists (FizTech2024), Vilnius, Lithuania, October 15–17 (2024). Oral.
- E2. <u>M. Mackevičiūtė</u>, J. Dudutis, P. Gečys, Bottom-up laser glass cutting using GHz bursts, 13th International Summer School on Trends and new developments in Laser Technology, Dresden, Germany, August 26–30 (2024). Oral.
- E3. M. Mackevičiūtė, J. Dudutis, P. Gečys, Vienašūvių modifikacijų formavimas lydytame kvarce naudojant MHz ir GHz papliūpas, 13th Conference of Doctoral Students and Young Scientists (FizTech2023), Vilnius, Lithuania, October 18-19 (2023). Oral.
- E4. <u>M. Mackevičiūtė</u>, J. Dudutis, V. Stankevič, V. Tomkus, G. Račiukaitis, Laser processing of glass nozzles for gas targets, Workshop of Laser particle accelerators, their applications, and possibilities of experiments in the ELI infrastructure, Vilnius, Lithuania, March 23 (2023). Oral.
- E5. <u>M. Mackevičiūtė</u>, J. Dudutis, L. Zubauskas, E. Daknys, E. Markauskas, R. Gvozdaitė, G. Račiukaitis, P. Gečys, Comparison of quality and flexural strength of laser-cut glass, 7th Venice International School on

Lasers in Materials Science (SLIMS 2022), Isola di San Servolo, Venice, Italy, July 3–9 (2022). Oral and poster.

E6. M. Mackevičiūtė, J. Dudutis, P. Gečys, Investigation of rear side glass milling using nanosecond laser pulses, 65th International Scientific Conference for Students of Physics and Natural Sciences (Open Readings 2022), virtual conference, March 15–18 (2022). Poster.

Lithuanian patents

F1. V. Tomkus, J. Dudutis, G. Račiukaitis, **M. Mackevičiūtė**, "Elektronų injektavimo ir greitinimo būdas ir įrenginys, skirti lazeriniams plazmos greitintuvams", Nr. 7099 B (2024).

AUTHOR'S CONTRIBUTION

The author has carried out most of the experimental work, data analysis, and visualization stated in this thesis and has prepared the manuscripts for the scientific papers [A1–A3]. The author also contributed to publications [B1–B5, C1] by providing gas injection nozzles to international research groups, utilizing the glass processing technology developed during this thesis.

CO-AUTHOR'S CONTRIBUTION

- Dr. Paulius Gečys supervised all the research.
- Dr. Juozas Dudutis advised on many aspects of the research, helped with the beam characterization measurements, and applied the inert and subcritical models for the separation stress simulation.
- Aleksandras Kondratas characterized volumetric modifications formed in soda-lime glass and evaluated the separation stress and the quality of the separated soda-lime glass samples.
- Dr. Julijanas Želudevičius helped with the temporal characteristic measurements of the burst modes.
- Light Conversion provided the lasers used in this thesis.

1. LITERATURE OVERVIEW

1.1. Light absorption

Dielectrics can absorb light via linear or nonlinear absorption mechanisms. For lower peak intensities, the photons with energies exceeding the bandgap are absorbed exponentially through the medium, with laser intensity I following the Beer-Lambert law [15]:

$$I(z) = I_0 \exp(-\alpha_a z), \tag{1}$$

where I(z) is the laser intensity after traveling the distance z, I_0 – initial laser intensity, and α_a – absorption coefficient (i.e., $\delta_{\rm opt} = 1/\alpha_a$ is the optical penetration depth). The absorption coefficient could be calculated with the formula below:

$$\alpha_a = \frac{4\pi\kappa}{\lambda},\tag{2}$$

where λ is the laser wavelength and κ is the extinction coefficient (imaginary part of the complex refractive index).

High intensity laser pulses with photon energies lower than the dielectric bandgap can be absorbed via nonlinear ionization mechanisms, which can be separated into photoionization and impact ionization [16]. For the strong field, photoionization occurs via tunneling, and for the weak field, it occurs via multiphoton ionization. During multiphoton ionization, the photons are absorbed at the same time, with the sum of their energies exceeding the bandgap. The condition for the multiphoton absorption is described by the formula below:

$$KE_{ph} \ge E_g,$$
 (3)

where K is the multiphoton ionization order, $E_{\rm ph}$ – photon energy, and $E_{\rm g}$ – material bandgap. The multiphoton absorption rate $W_{\rm MPA}(I)$ has a power law dependence on laser intensity I, described by the following formula:

$$W_{\text{MPA}}(I) = \sigma_K I^K, \tag{4}$$

where σ_K is the cross-section for the K^{th} order multiphoton absorption [17]. Multiphoton ionization occurs for higher energy photons (shorter laser wavelength) and relatively low peak intensities [18]. At higher intensities, the contribution of tunneling ionization becomes more significant, as the potential barrier is distorted, allowing the electrons to tunnel from the valence to the conduction band [19]. Notably, the tunnel ionization rate has a much weaker dependence on laser intensity compared to the multiphoton ionization [17]. The dominant photoionization mechanism can be defined with the Keldysh parameter γ [20]:

$$\gamma = \frac{\omega\sqrt{2mE_{\rm g}}}{eE_{\rm o}},\tag{5}$$

where ω is the optical frequency, E_0 is the amplitude of the driver field, and e and e and e are the electron charge and mass, respectively. The multiphoton ionization dominates when e >> 1, while the tunnel ionization is more prominent for e << 1 [21]. Both processes are observable when the Keldysh parameter is e -1. For most investigations of dielectric machining, the multiphoton ionization dominates, as the tunnel ionization requires an extremely strong laser electromagnetic field [22].

The photoionization does not require initial free electrons. However, avalanche ionization can only occur with seed electrons in the conduction band, which can be generated from the linear or nonlinear photoionization absorption by defects or impurities, or from nonlinear photoionization absorption by valence electrons [23]. The free electrons absorb photons via inverse bremsstrahlung, increasing their kinetic energy. When the electron kinetic energy is higher than the bandgap, it can collide with a valence band electron, bringing it to the conduction band. This process is known as impact ionization, and the recurrence of it - avalanche ionization. In avalanche ionization, each electron excites another electron to a conduction band. Therefore, it is typically assumed that the impact ionization grows exponentially [24]. The avalanche ionization only becomes significant for a sufficient number of high-energy electrons in the conduction band [24]. For ultrashort pulses on the order of tens of femtoseconds, there is not enough time for a sufficient number of high-energy electrons to accumulate in the conduction band, making avalanche ionization negligible [24]. As a result, multiphoton photoionization dominates for ultrashort pulses with relatively low intensity [25]. Higher intensity shortens the time for required seed electrons with high kinetic energy to build up, allowing avalanche ionization to dominate [26]. Therefore, the avalanche ionization dominates for longer pulse durations and higher intensities.

1.2. Laser-induced material damage

The electrons pass their energy to other electrons via collisions on the timescale of several tens of femtoseconds [26]. At that time, the temperature of the electrons is high while the lattice stays cold. The relaxation to the thermal equilibrium and energy transfer from the excited electrons to the lattice occur via the electron-phonon collisions [24]. Although the characteristic timescale of electron-phonon collisions is a few femtoseconds, the energy relaxation time increases to picoseconds due to the large mass difference between an ion and an electron [26]. After this, the electrons and the lattice go into thermal equilibrium, which is typically considered to occur around 10 ps [27].

For the ns-scale or longer pulses, energy is transferred from electrons to phonons during the duration of a pulse, resulting in heat diffusion over a volume larger than the focal region [28]. Therefore, nanosecond pulses result in larger damage zones compared to shorter pulses [29]. Furthermore, longer pulses induce larger thermal stresses, which can exceed the fracture threshold [30,31]. This would allow material to be removed with high efficiency, as only 50 J is required to fracture 1 cm³ of fused silica (FS), whereas vaporization requires 18.3 kJ [32].

For the short (fs to ps) pulses, the electrons are driven to much higher temperatures (tens of eV, where 1 eV = 11600 K) during the pulse duration, while the lattice remains relatively cold [28]. The energy transfer from excited electrons to the lattice can lead to heating rates exceeding 10^{14} K/s, resulting in material melting, vaporizing, or, in more extreme cases, the formation of a supercritical fluid [19]. Shorter pulses also result in smaller heat-affected zones compared to the longer pulses, which is more favorable for precise machining [33,34]. Furthermore, the ablation threshold increases with pulse duration, scaling as $\sqrt{\tau_p}$ in the 20 ps – 10 ns range, a behaviour attributed to thermal diffusion [35]. For $\tau_p < 20$ ps, the ablation threshold continues to decrease but at a slower rate due to the decreasing impact of the avalanche ionization.

It is commonly considered that material damage occurs when the free electron density reaches the critical density n_{crit} [36]. At this point, a highly absorbing plasma is formed, resulting in most of the laser energy being transmitted to the material [27]. For the soda-lime glass (SLG) and FS samples

used in the experimental part, the critical density is $\sim 10^{21} \, \text{cm}^{-3}$ for the wavelength of 1030 nm, calculated with the equation given below [26]:

$$n_{crit} = \varepsilon_0 \varepsilon_r \frac{m_e \omega^2}{e^2},\tag{6}$$

where ε_0 is the vacuum permittivity, ε_r – relative permittivity (dielectric constant), and m_e is the effective mass of the free electrons.

1.3. Fused silica and soda-lime glass

FS and SLG are among the most commonly used glass materials in optical and industrial applications, each exhibiting distinct physical and chemical properties that significantly influence their response to laser processing. FS is composed of SiO₂, while SLG contains more components (listed in Table 1). FS typically has a higher cost than SLG due to its more complex manufacturing process. However, FS offers superior chemical and thermal resistance, as well as high transparency across the UV, visible, and IR spectral regions, making it ideal for high-end applications such as high-precision or high-power optical systems, manufacturing of semiconductors, spacecraft and satellite components, and medical devices. In contrast, SLG is more affordable and is commonly used in everyday applications such as containers and packaging, windows, doors, and glassware [37]. The parameters for FS and SLG are given in Table 1.

FS exhibits a higher linear refractive index than SLG, resulting in greater Fresnel reflections at the surface of a material. SLG has an absorption coefficient of 0.58 cm⁻¹, resulting in 94% internal transmission for a 1030 nm wavelength beam passing through a 1 mm-thick sample. In contrast, FS has an absorption coefficient ~4 orders of magnitude lower, resulting in nearly zero losses as the beam passes through the same thickness. Additionally, the damage threshold of FS is slightly higher than that of SLG, indicating that it requires greater energy density to cause damage.

The thermal properties of materials play a crucial role in laser processing. Thermal expansion refers to the change in length or volume of a material when it is subjected to changes in temperature. The SLG has a higher thermal expansion coefficient, meaning it undergoes greater dimensional changes when heated. Consequently, higher thermal stresses develop during processing, particularly due to the temperature gradients between heated and unheated regions. Additionally, FS has higher thermal diffusivity, which

Table 1. Parameters of FS and SLG. The internal transmission T_i was calculated as T_i =exp($-\alpha_a z$), with z equal to 1 mm. AOI corresponds to the angle of incidence.

	FS	SLG
Composition	SiO ₂	SiO ₂ , Na ₂ O, CaO, MgO, and
		Al ₂ O ₃ [38]
n_0	1.45 (1030 nm) [39]	1.51 (1030 nm) [37]
n_2	2.19 · 10 ⁻²⁰ m ² /W	1.25 · 10 ⁻²⁰ m ² /W
	(1030 nm) [40]	(800 nm) [41]
Surface reflection	3.3% (1030 nm) [39]	4.2% (1030 nm) [37]
(at 0 deg AOI)		
Internal transmission, T _i	100% (1030 nm)	94% (1030 nm)
(1 mm-thick sample)		
Absorption coefficient, α _a	$10^{-5} \text{ cm}^{-1} (\lambda = 1 \mu\text{m}) [42]$	$0.58 \text{ cm}^{-1} (\lambda = 1030 \text{ nm}) [37]$
Damage threshold, F _{th}	1054 J/cm ² (20 ns) [29]	923 J/cm ² (20 ns) [29]
	3.6 J/cm ² (500 fs) [29]	2.9 J/cm ² (500 fs) [29]
Thermal expansion	0.5 · 10 ⁻⁶ K ⁻¹ [38]	9 · 10 ⁻⁶ K ⁻¹ [38]
Thermal diffusivity, D	0.8 mm ² /s [43]	0.5 mm ² /s [44]
Softening temperature	1600 °C [42]	720 °C [38]

allows heat to spread more rapidly and uniformly across the material. In contrast, the heat in SLG is more localized, which, combined with its higher thermal expansion coefficient, leads to higher thermal stresses and an increased likelihood of cracking. Due to its lower thermal expansion and ability to dissipate heat more rapidly, FS is more resistant to temperature changes. FS also has a higher softening temperature, meaning it requires higher temperatures to transition from a solid to a more fluid state. This gives FS a greater capacity to withstand laser processing at higher intensities without deforming or losing its structural integrity.

1.4. Beam propagation

In this subsection, the most common beam types used in laser glass cutting will be discussed. The scheme of the Gaussian beam, filamentation due to self-focusing, and the Bessel beam formed with an axicon is shown in Figure 1.

1.4.1. Gaussian beam

The Gaussian distribution is the most common for lasers, with the intensity $I(\mathbf{r})$ defined as:

$$I(r) = I_0 \exp\left(-\frac{2r^2}{w(z)^2}\right),\tag{7}$$

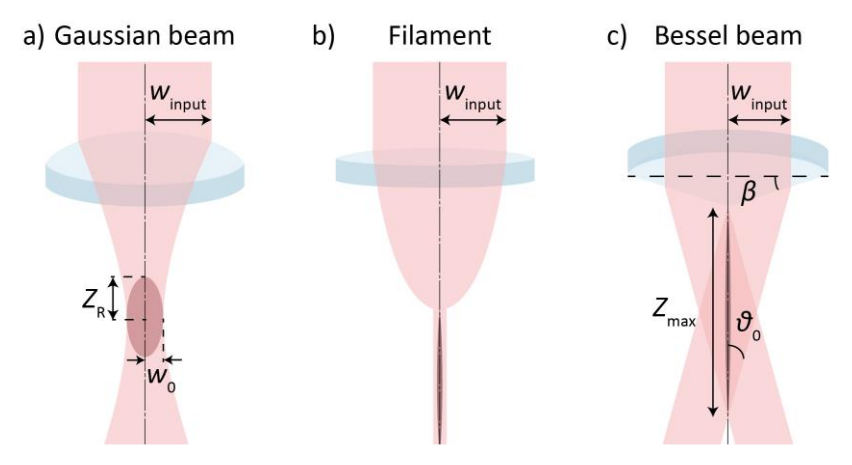


Figure 1. Schematic drawing of Gaussian (a), filament (b), and Bessel (c) beams.

where I_0 is the peak intensity at the center of the beam (r = 0), r is the radial distance from the beam center, and w(z) is the beam radius measured at $1/e^2$ intensity level at the distance z from the beam waist along the propagation axis. The beam radius w(z) along the propagation can be calculated with the following formula:

$$w(z) = w_0 \sqrt{1 + \left(\frac{z}{z_R}\right)^2},\tag{8}$$

where w_0 is the beam radius at the focus position (measured at $1/e^2$ intensity level), and z_R is the Rayleigh length. The Rayleigh length describes a distance from the focus position at which the beam radius increases by a factor of $\sqrt{2}$, calculated by:

$$z_R = \frac{\pi w_0^2}{M^2 \lambda},\tag{9}$$

where M^2 is the beam quality parameter indicating how closely the real beam approximates the perfect Gaussian beam, and λ is the laser wavelength in a propagating medium. Therefore, the beam radius at a specific z position can be easily calculated using the waist radius, M^2 , and the laser wavelength. The beam radius at the focal position w_0 can also be calculated as:

$$w_0 = M^2 \frac{\lambda f}{\pi w_{input}},\tag{10}$$

where f is the focal length of a lens, w_{input} is the beam radius (measured at $1/e^2$ intensity level) before the focusing lens.

1.4.2. Filamentation via self-focusing

The aforementioned formulas for Gaussian beams are correct when assessing the linear propagation. However, high peak intensities can induce nonlinear optical effects, altering the beam propagation. In 1995, Braun *et al.* observed a high-intensity collimated beam diameter shrinking to $100 \, \mu m$ and maintaining its diameter for $20 \, m$ in air [45]. This was the first observation of filaments formed via self-focusing. This sub-subsection will discuss the formation and properties of filamentation.

Ultrashort pulse lasers make it possible to achieve such high peak intensities that the beam and the medium begin to interact nonlinearly. The refractive index of a medium can be described by a formula [46]:

$$n = n_0 + n_2 I, (11)$$

where n_0 is the linear and n_2 – nonlinear refractive indices. Both n_0 and n_2 depend on the medium and laser wavelength. However, n_2 can also depend on the pulse duration and polarization state [47,48]. Specifically, n_2 is approximately 33% lower for circular polarization compared to that of linear polarization [48]. The n_2 is typically positive and in the order of 10^{-20} m²/W for glasses [40,47,49]. This means that the refractive index n increases with higher peak intensities. For the Gaussian beam, this results in the highest refractive index at the center of the beam. Therefore, the beam wavefront undergoes changes similar to those induced by a convex lens, with the difference that it is a cumulative effect [46]. The phenomenon of self-focusing starts to occur when the peak power P_p exceeds the critical P_{cr} [50]:

$$P_{cr} = \frac{\pi (0.61)^2 \lambda^2}{8n_0 n_2}. (12)$$

The critical power for self-focusing in dense transparent dielectrics is in the range of MW, while for gases, GW are needed due to ~3 orders of magnitude

lower nonlinear refractive index [46]. The peak power of ~1 MW is reached with $E = 1 \mu J$ and $\tau_p = 1 ps$ ($P_p = 0.94 E/\tau_p$).

A collimated beam with a peak power higher than the critical will focus at the distance L_c , which can be calculated using the semi-empirical formula of Dawes and Marburger [51]:

$$L_{\rm C} = \frac{0.367\pi n_0 w_{input}^2}{\lambda \sqrt{\left[\sqrt{(P_{\rm p}/P_{\rm cr})} - 0.852\right]^2 - 0.0219}}.$$
 (13)

Due to self-focusing, the beam diameter is constantly decreasing. As the beam cannot be focused indefinitely, certain mechanisms must counteract the self-focusing. The most important mechanisms are the multiphoton absorption and the associated plasma defocusing [52]. As the beam diameter decreases, the peak intensity increases. At considerably high intensity, multiphoton ionization starts to occur. The ionization of the medium initially occurs at the center of the beam, where the intensity is highest. The generated free electrons result in a local reduction in the refractive index, creating an effect similar to that of a diverging lens, leading to beam defocusing [46]. If, after absorption, the beam power remains higher than the P_{cr} , the self-focusing repeats. As a result, high peak intensity (10¹³⁻¹⁴ W/cm²) narrow diameter (~40–100 μm in air [45,53,54], and \sim 1–10 µm in glass [55–57]) beams can be maintained over long distances (up to meters in air [45,58], and up to centimeters in glass [59]). The filament length is smaller in condensed matter compared to gases due to (i) lower critical power and, thus, more than 2 orders of magnitude higher electron density leading to larger energy loss during propagation, (ii) larger group velocity dispersion broadening the pulse duration and, thus, decreasing peak power during propagation [60].

In practice, it is suggested that the peak power must exceed 3–5 times the critical power $P_{\rm cr}$ for stable filament formation to occur [18,59]. Within the range $P_{\rm cr} \le P \le 5P_{\rm cr}$, the focusing-defocusing cycles are typically not observable, and the beam propagates in a sub-diffractive regime, with the filament diameter gradually increasing along the propagation path [18]. However, if the peak power significantly exceeds the $P_{\rm cr}$, the beam can evolve into multiple refocusing cycles or be broken into several filaments [61]. In practice, the latter case is more common, as fluctuations in intensity lead to self-focusing when the local power exceeds the critical power for self-focusing [60]. If the power of an individual filament becomes smaller than the

 $P_{\rm cr}$, its energy is transferred to a joint energy reservoir, which leads to a new distribution of filaments [46]. The number of filaments N tends to decrease with propagation distance due to energy losses, often leading to a state in which only a single filament remains [46].

Multifilamentation (MF) caused by input noise exhibits strong shot-to-shot variability due to its sensitivity to initial perturbations. Maintaining a stable and controllable filamentation pattern is crucial for MF to be employed in practical applications. In 2001, Fibich et al. suggested that MF can arise from the vectorial effects, specifically those related to polarization [62]. Their simulations indicated that linear polarization can break the axial symmetry of the beam. As a result, the beam was shown to split into two filaments positioned either along or perpendicular to the direction of linear polarization [62]. Linear polarization can produce a deterministic MF pattern. while it is unlikely to be caused by a circular or slightly elliptical polarization [63]. Furthermore, the linear and circular polarizations remain unchanged along the filament, while the orientation and shape of the elliptical polarization vary [64]. Nonlinear interaction induces different phase and amplitude changes between polarization components, causing the polarization ellipse to rotate along the filament. Polarization-induced MF is deterministic with filaments of comparable power, while noise-induced filaments have a high-power central filament and significantly less-powerful off-axis filaments [65].

Dubietis *et al.* have shown that even a small input beam ellipticity of 1.09 can result in a reproducible MF pattern consisting of a central filament and (or) pair of identical filaments along the major and (or) minor axes of the ellipse and (or) quadruple of identical filaments along the bisectors of the major and minor axes [66]. Majus *et al.* have shown that highly elliptical beams turn into reproducible MF arrays with periods independent on ellipticity [67]. The study has revealed that higher input beam peak intensity results in reduced periods of the MF array or even its conversion from one-dimensional to two-dimensional. Deterministic MF arrays could be formed with a metallic periodic mesh [68], circular or rectangular diaphragms [69], a microlens array [70], or by interfering two laser pulses [71]. Hao *et al.* demonstrated that MF can be switched to a single filamentation by using a diaphragm of a small diameter [69].

Liu *et al.* have demonstrated that the peak intensity and thus the excited electron density in the filaments are clamped above a threshold input pulse energy [72]. Increasing the input energy above the threshold results in energy redistribution and MF formation [60,72]. The intensity clamping is observed in all optical media [60]. However, the value of the clamped intensity depends

on the focusing conditions [53,73]. Théberge *et al.* have observed that the peak plasma density increased by 3 orders of magnitude when the focusing length was reduced from 380 cm to 10 cm [53].

In order to damage a material, the electron density needs to reach the critical value, which is $\sim 10^{21}$ cm⁻³ for FS and SLG. For tight geometrical focusing, the damage threshold intensity can be reached earlier than the self-focusing starts to noticeably affect the propagation of a pulse [60]. As most of the energy is deposited into the material, the rest of the energy is insufficient to refocus, causing the beam to quickly diverge after the focus [74]. For weak focusing or collimated beams, a less dense electron plasma is needed to counteract self-focusing and diffraction. The electron density typically reaches 10^{18-20} cm⁻³, which is lower than the critical density for damage [46]. Therefore, no damage in the bulk of FS is induced by filaments using weak focusing despite the peak powers reaching from 12 MW to \sim GW [59,75].

However, under the proper conditions, the filament can propagate inside the material, inducing its damage [76,77]. Different studies suggest avalanche ionization to be an essential mechanism for permanent bulk damage [59,75,78]. With proper focusing conditions, the beam converges to a diameter with an intensity high enough for multiphoton ionization to produce sufficient electron densities to trigger the avalanche ionization and induce damage [78]. Furthermore, Sun et al. have demonstrated that an optimal pulse duration exists for achieving the highest plasma density, supposedly due to the different contribution of an avalanche ionization [79]. For ultrashort pulses (< 100 fs), avalanche ionization has a low impact as only a few cycles can be repeated, while longer pulses result in lower peak powers and, thus, a weaker self-focusing effect [79].

1.4.3. Bessel beam

The Gaussian–Bessel beams will be briefly discussed as they are commonly used in glass processing [80–82]. An ideal Bessel beam can maintain its shape and intensity along the propagation direction over infinite distances, assuming infinite energy [83]. In practice, Bessel-Gauss beams are used, having finite propagation lengths [84]. The Bessel-Gauss beams can be formed with conical lenses (axicons) [85], spatial light modulators (SLM) [86,87], diffractive optical elements (DOE) [88], or a setup consisting of a circular slit and lens [84].

The length of a non-diffractive zone of a Bessel beam formed with an axicon can be calculated with the radius of the incident beam (w_{input}) and the half-angle of the cone (9_0) [89]:

$$z_{max} = \frac{w_{input}cos\theta_0}{\sin\theta_0}.$$
 (14)

The half-angle can be calculated using the base angle of an axicon (β) [90]:

$$\vartheta_0 = \arcsin\left(n\sin(\beta)\right) - \beta. \tag{15}$$

The radius of a central core of the Bessel beam (ρ_0) at the zero-intensity point can be evaluated with the formula given below [91]:

$$\rho_0 \sim \frac{2.4\lambda}{2\pi \sin \theta_0}.\tag{16}$$

One can see that the radius of a central spot can be controlled with the base angle of an axicon, while the propagation length can be adjusted by varying the radius of the incident beam. The extremely small central spot radius of Bessel-Gauss beams can be maintained over long distances. For example, a typical FS axicon with a base angle of 2 deg will produce a beam with a central spot radius of 25 μ m propagating over a 64 mm length, when using λ = 1030 nm and w_{input} = 1 mm. By comparison, the Rayleigh length of a Gaussian beam with a waist radius of 25 μ m will only reach 1.9 mm (calculated with equation (9) using M^2 = 1 and λ = 1030 nm). Furthermore, the Bessel beams exhibit a more uniform intensity distribution along the propagation axis compared to the Gaussian beam. Therefore, the Bessel beams are more suitable for high-aspect ratio structures or hole formation. Furthermore, the self-recovery feature of the Bessel beams allows the beam to be efficiently delivered to the target surface even when the beam is disturbed by an obstacle [92].

1.5. Mechanical glass cutting

The most established way of cutting glass is mechanical scribing and breaking, depicted in Figure 2(a–c) [4]. This conventional method is limited to simple contours; however, it offers rapid, cost-effective, and kerf-free separation of samples. In the first step, a fissure is formed along the glass surface with a carbide [4] or diamond wheel [93]. At the second step, the glass is separated thermally or mechanically by inducing tensile stresses along the fissure. The recommendation is to form the median crack with a length covering at least 10% of the glass thickness [94]. The median crack length can be increased

with higher pressure and sharper wheel [4]. However, this also leads to larger lateral cracks which can extend transversely, resulting in chippings [95,96]. Therefore, thicker samples are expected to have poorer quality.

While the scribe and break method is well established, the cutting line deviation from the scribing line due to non-optimal scribing conditions remains a significant issue [96]. Furthermore, the contact processing methods result in tool wear, which affects the quality of the samples [94]. The service life of the roller can be extended by using a lubricating liquid, which also provides a more uniform distribution of force [97]. However, this also leads to the contamination of the samples and increased machining costs due to the need for recycling and waste disposal [98].

The alternative mechanical technique of disk sawing utilizes a metal or SiC disk attached to a spindle and powered by a motor [99]. The cutting can be performed either by moving the cutting disk or by bringing the sample to it. The disk sawing machine and sawing blades are shown in Figure 2(d–e). To minimize the temperature effects, the disk and the samples can be placed in a liquid bath of water, oil, or alcohol [99]. The simple, cheap, and reliable method allows multiple glass sheets to be cut at once at the expense of reduced speed [99]. However, there are some drawbacks to this method: (i) the trajectory is limited to the straight cuts, (ii) the generated heat leads to plastic deformations, and (iii) additional grinding and polishing are required after the cutting [99]. Furthermore, the cutting width (kerf) depends on the disk thickness and can reach ~mm [99].

Cutting kerfs down to 0.3 mm and complex contour cutting can be achieved with diamond wire sawing [100]. The wire sawing system is shown in Figure 2(f). Here, an abrasive wire (Figure 2(h)) interacts with the sample as it is constantly moved with the help of pulleys and guides depicted in Figure 2(g) [101]. Although this method allows cutting complex contours, the cutting speed is low (5–10 μ m/s), and the vibrations of the wire always cause subsurface damage [102].

A high-pressure jet of water expelled through a narrow nozzle at extreme speed can be used for glass cutting. The material is removed due to erosion as particles of high kinetic energy impact the sample [103]. Waterjet cutting allows complex trajectory cuts as the nozzles (Figure 2(j)) can be precisely moved along the desired paths using the CNC systems (Figure 2(i)) [104]. The cutting does not produce heat-affected zones, as all the heat is carried away by water [105]. Furthermore, waterjet cutting results in lower internal stresses compared to a more traditional disk cutting [99]. The process can be done with or without abrasive particles. However, smoother cut sections are produced

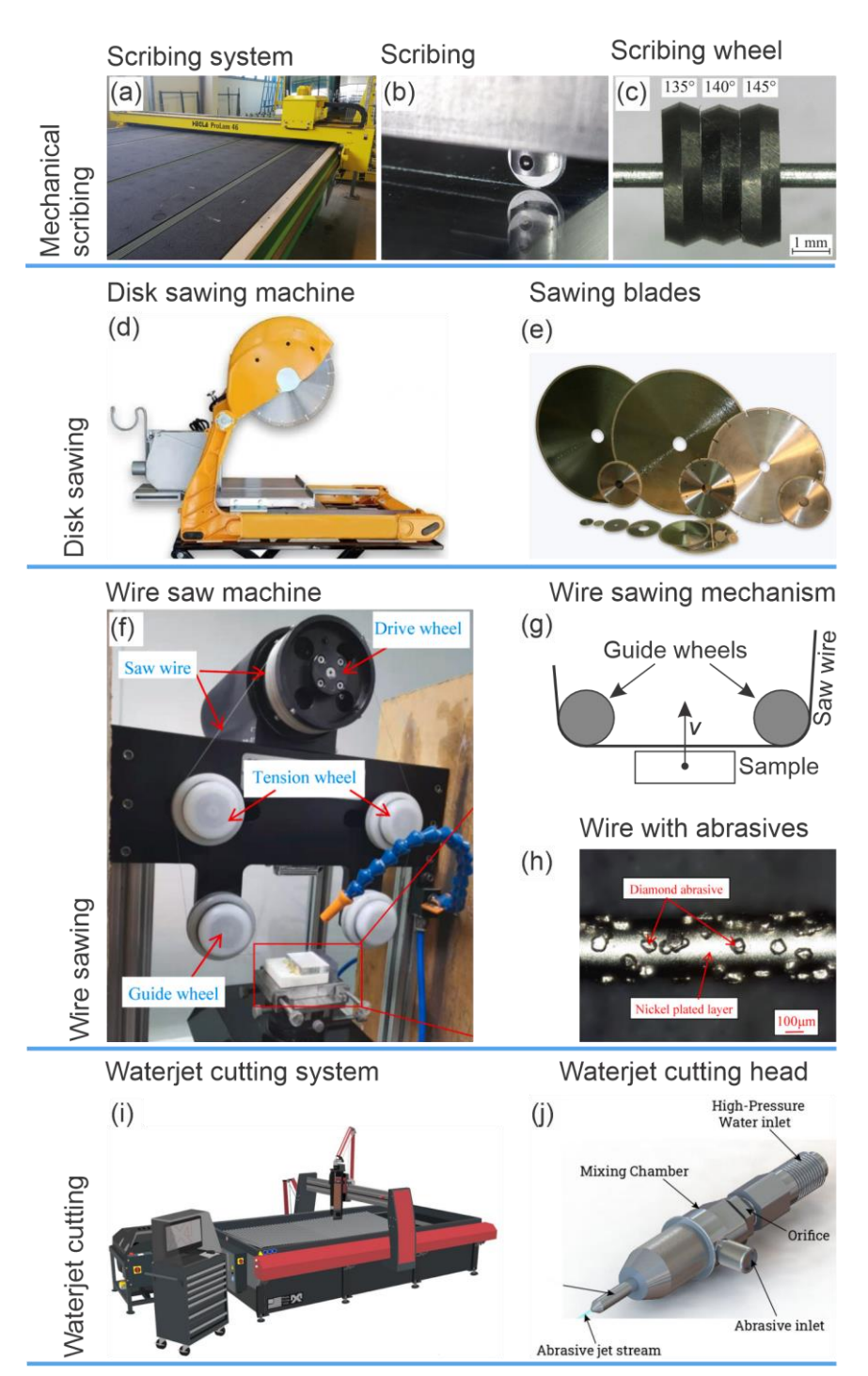


Figure 2. Mechanical glass processing methods of mechanical scribing (a–c) [4], disk sawing (d, e) [106], wire sawing (f–h) [107], and waterjet cutting (i, j) [108]. The images (a–c) were reproduced from [4] with permission from SNCSC, and images (f, h) were reprinted from [107], Copyright © 2021, with permission from Elsevier.

when using abrasive material ($R_q = 25.4 \,\mu\text{m}$) compared to the cutting with only deionised water ($R_q = 127 \,\mu\text{m}$) [109]. The method allows forming surface roughness in the range of 2.1–22.5 $\,\mu\text{m}$ (R_a) [103,110]. The primary disadvantages of the waterjet are: expensive equipment, high noise level, long processing time, and the need for additional grinding and cleaning [99,105].

1.6. Laser-based glass cutting

One of the first industrial applications of lasers was glass cutting [105]. Firstly, the laser scribe and break, then controlled fracture and ablative methods were developed [105]. Laser cutting is a non-contact method allowing precise, high-quality cuts to be produced. Different laser cutting methods shown in Figure 3 will be thoroughly discussed in the following subsubsections.

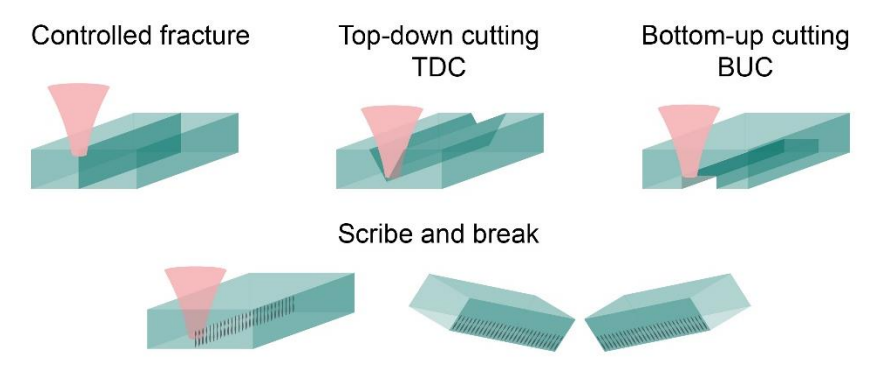


Figure 3. Laser-based glass cutting techniques.

1.6.1. Controlled fracture

Glass cutting via controlled fracture using a CO₂ laser was first introduced by Lumley in 1969 [105]. The laser is used to heat the glass sample and induce compressive stresses near the laser spot. As the beam is scanned, the material behind it begins to cool, compressive stresses relax, and tensile stresses start to form near the surface. A crack is formed if the tensile stresses exceed the failure stress [111]. The crack grows from the top to the bottom as the remaining stresses throughout the sample thickness are compressive [112]. As the tensile stresses form after a laser passes, the crack tip follows the laser spot

at a certain distance [112]. The area between the crack tip and the laser spot is dominated by compressive stresses, ensuring stable crack propagation [112].

The specimen size affects the cutting process. Thicker samples require higher power [105]. Furthermore, narrow specimens can be cut at higher speeds due to the better release of compressive stresses around the crack tip, resulting in higher tensile stresses and faster crack propagation [112].

The process is typically performed below the glass transition temperature [105]. Therefore, it is faster and more efficient compared to the ablative processes [105]. The method allows for cutting 1 mm-thick SLG samples at 30 mm/s [113].

Most glasses highly absorb the 10.6 μ m wavelength (CO₂ laser), resulting in an optical penetration depth of a few μ m [114]. As the laser pulses are absorbed at the surface of the sample, the glass separation can be performed for thicknesses limited to 3 mm [115]. For thicker samples, a 1 μ m wavelength laser source can be used as it is mainly transmitted in most glasses and results in volumetric absorption. For example, the optical penetration depth is 17.2 mm for SLG as the absorption coefficient is $\alpha_a = 0.58$ cm⁻¹ at 1030 nm wavelength ($\delta_{opt} \approx \alpha_a^{-1}$) [114]. This allows the processing of cm-thick glasses [114]. Furthermore, the stability and uniformity of tensile stresses result in smaller cut path deviations and better surface quality compared to the CO₂ laser [115]. The cutting process can further be enhanced by focusing the laser at multiple positions, resulting in more uniform laser pulse absorption throughout the sample thickness [30,102,116].

The controlled fracture method enables the separation of cm-thick samples at ~mm/s speed and the formation of smooth sidewall surfaces [30,112]. However, the separation path deviation is a problem of high significance [30,112]. This processing uncertainty results in many broken parts and limited complexity trajectories [91].

1.6.2. Laser scribe and break

Similar to the mechanical method, laser scribing and breaking offers m/s speed [6,117], is kerf-less, is limited to simple contours, and consists of two steps. The separation step is identical to the mechanical method, as it is performed by inducing tensile stresses mechanically or thermally [93,110]. The scribing step can be performed by ablating a groove [118], forming elongated volumetric modifications in the glass [119,120], or both [121,122]. It is more common to form elongated modifications, as longer modifications reduce the flexural strength of a sample [5]. Lower separation stress means a reduced risk of unwanted cracking or chipping, higher control and

repeatability of the separation line, and a higher chance of clean separation with smoother edges.

By forming modifications along the thickness of the sample, single-pass scribing of ultrathin (0.1 mm) and thick (10 mm) samples can be performed [123,124]. The elongated volumetric modifications can be formed by: (i) focusing the beam multiple times at different depths using high NA, (ii) focusing a Gaussian beam with low NA, (iii) using a nonlinear self-focusing regime, (iv) using Bessel beams [91]. The most common are filamentation and Bessel beams due to their non-diffractive properties, allowing for the formation of high-aspect-ratio modifications. The following paragraphs will thoroughly discuss scribing via filamentation and Bessel beams.

The system for filamentation scribing is quite straightforward as it only requires a laser, lens, and beam or sample positioning system. Filament scribing has high potential, as beam scanning speeds of up to tens of meters per second could be achieved with a system consisting of a f-theta lens and fast beam scanners. However, due to the µm-sized transverse damage zones [122,125], the modifications must be positioned close to each other, limiting the scanning speed. Faster scanning could be achieved with a higher pulse repetition rate, as the scanning speed equals the distance between the shots multiplied by the pulse repetition rate. As the filamentation requires high pulse peak powers, this method would require a laser source capable of delivering short, high-energy pulses at a high pulse repetition rate. Alternatively, faster scribing could potentially be achieved by increasing the size of the damage zone. However, no studies have shown a significant increase in the damage width of modifications formed in glass via filamentation.

The modifications induced by filamentation are formed at a distance from the front surface of a sample. This occurs because, after reaching the threshold, some distance is needed for the Kerr effect to build up [126]. As the highest tensile stresses are formed at the tensioned surface, it is favorable for the modifications to reach the surface [38]. Butkus *et al.* have demonstrated that filaments near the front surface of a sample can be created using an additional water layer, where the Kerr effect is built up [76]. Another solution is to position the modifications close to the bottom surface and then tension it in the separating step.

J. Li *et al.* investigated different filament scribing configurations in 1 mm-thick glass – V-shaped grooves formed either at the front or the bottom surfaces, without or with filament-induced modifications reaching the groove, and the sole filament-induced modifications inside the glass not reaching any surface [122]. In addition, single-pulse and burst regimes were tested for the

filament array formation. The results have shown that the sole V-shaped grooves on the bottom or top surfaces and the sole internal filament array formed with a single-pulse regime resulted in non-reproducible fracturing, weakly guided cleaving, and irregular facets. However, the V-shaped grooves with a filament array formed using single-pulse and burst regimes, as well as the sole filament array formed using bursts, resulted in reproducible fracturing and guided cleaving.

The glass scribing with Bessel beams has been studied by different scientific groups [91,124,127,128]. Here, the system is more complicated compared to filamentation, as an axicon and an additional beam expanding system are needed to optimize the length and radius of the Bessel zone for a specific sample. Thus, different thickness samples would require altering the system. Scanning is typically performed with mechanical sample positioning stages. However, the speed of the positioning stages is limited as the highspeed motion of the stages reduces accuracy due to the increasing effects of friction, backlash, and mechanical vibrations [129]. Galvanometer and polygonal beam scanning systems can offer higher processing speeds without compromising accuracy. However, Bessel beams are prone to misalignment, and beam scanning could result in tilt-induced aberrations, deteriorating the circular central spot [130]. Although a galvanometer scanner system with a low half-angle Bessel beam can be suitable for ablation and polishing, the scribing process could be more complicated, as crack angles might depend on the XY position due to differences in the transverse shape of the beam [90].

Attention to the glass scribing with Bessel beams significantly increased after Dudutis *et al.* demonstrated the formation of modifications with controllable transverse cracks [89]. The axicon used in the study exhibited an elliptical shape near the oblate tip surface, resulting in an elliptical central core of a Bessel beam. The cracks aligned along the major axis of the central core of the beam. However, some studies indicate that the cracks could align along the side lobes of the generated beam instead of the elliptical central core [88,131].

Different approaches have been suggested for crack control. For example, the aforementioned axicon with an elliptically-shaped tip can be rotated around its optical axis [89]. The tilting of an axicon is also a reliable way to induce ellipticity, as not only does it induce asymmetry, but tuning the tilt can also generate symmetric beams [127,132]. Jenne *et al.* have demonstrated that modulated beams, controlling the crack angle, can also be formed using DOE or SLM [88]. The SLM offers high flexibility as it can control the intensity, phase, and polarization of light. Despite this, SLMs are expensive, inefficient, and have a low damage threshold [88]. Therefore, high-power material

processing is commonly performed using non-flexible DOE, manufactured according to the experiments with SLMs [133]. The crack angle can also be controlled with amplitude and phase masks [134]. However, both mask types reduce beam energy due to blocking part of the beam or non-perfect beam shaping efficiency [134]. In 2023, B. Stepak *et al.* demonstrated that omnidirectional cracks start to align along the scanning line despite the trajectory [12]. The cracks turned from directional to omnidirectional when using the MHz burst regime with a pulse duration exceeding 2 ps [12].

The cracks aligned along the scribing line extend the damage area, weakening the sample across the scribing line [89]. As a result, the modification center-to-center distance can be increased, allowing for high scribing speeds to be achieved while maintaining a stable glass separation. The lowest sample separation stress was shown to be reached when the modification center-to-center distance is between half and full length of a crack [134]. The cracks in SLG reached 200 μ m with a longitudinal length of 1.1 mm when using 1064 nm wavelength 300 ps pulses at 2 mJ [135]. This enabled the scribing of 1 mm-thick SLG samples with modifications formed at 125 μ m distance, reaching the scribing speed of 125 mm/s and a sample separation stress of 11 MPa [135].

The simulations of nonlinear absorption of the Bessel beam have indicated that picosecond pulses are more efficiently absorbed by BK7 and FS compared to the femtosecond pulses if sufficient energies are used [136]. The study investigating elongated nanostructure formation in FS confirms this, as increasing the pulse duration from femtoseconds to picoseconds resulted in the void transforming from uniform to fragmented [137]. Mever et al. showed that the samples were uncleavable when using 50 fs pulses, while picosecond pulses were suitable for scribing 10 mm-thick SLG samples [123]. However, bursts with femtosecond pulses have shown promising results, as each pulse undergoes fewer perturbations during nonlinear propagation, and the total energy deposition in the material is enhanced due to accumulation effects [138]. The MHz burst with femtosecond pulses was used to form cracks with lengths up to 10 µm in 0.5 mm-thick Eagle glass [138]. A study comparing MHz and GHz burst modes for scribing has shown that, under optimized conditions, the GHz bursts result in better sidewall quality and, thus, a more controlled cutting process [139].

1.6.3. Top-down cutting

The material removal from the top surface towards the bottom through the full thickness of a sample is called top-down cutting (TDC). First, the beam is

focused on the top surface of a sample. For a single shot, a parabolic-shaped crater will be formed with a Gaussian beam for fluence higher than the ablation threshold [140]. However, the crater becomes V-shaped after multiple consecutive shots due to the enlarged beam spot area on the sidewalls and increased Fresnel reflections, resulting in lower fluence [141,142]. Scanning the beam in one direction produces a groove, while repeating the scanning increases its depth. However, the depth of the groove is limited due to the V-shaped form. Therefore, only thin glasses can be cut this way [143]. By repeating the scanning in a parallel-shifted trajectory, the groove can be widened, allowing for an increase in depth [144]. However, as more material is removed, the beam gets defocused. Therefore, when cutting thicker materials, the fluence on the interaction zone decreases, eventually leading to inefficient or no ablation. To overcome this, the beam waist position in the Z axis can be lowered after each scanning sequence [5]. Alternatively, the beam can be focused more loosely to increase the Rayleigh length. However, this reduces the maximum fluence in the waist position. Another possibility is to use the non-diffractive beams [145].

The TDC produces sidewalls with an 8-28 deg taper angle (shown in Figure 4(o)) [144,146]. Therefore, a cut through a 1 mm-thick sample would require the cutting widths of 0.3-1 mm. Because of this, the top-down approach is typically used for 1 mm and thinner glasses [5,144]. It should be noted that the taper angle of the sidewalls can be controlled with the angle of incidence of the beam. This is implemented in helical drilling systems, offering independent adjustment of the hole diameter and the angle of incidence of the beam using Dove prism or wedge systems [147–149]. However, this approach is typically used for circular hole formation, rather than cutting applications. Hoang Le et al. have suggested using the precess module with a telecentric f-theta lens, which enables the formation of complex shapes [150]. Although the system equipped with a precess module demonstrated a reduction in taper angle to 2 deg, the scanning speed of the module was limited to 50 mm/s, resulting in a slow machining speed [150]. Hao et al. suggested forming the initial groove with a laser and using a mechanical drill to form steep walls [151]. However, the additional step complicates the machining setup and increases the processing time.

The TDC results in larger damage widths on the bottom surface compared to the top surface [5]. Furthermore, the V-shaped grooves cause parallel to the cut edge and periodical band-like defects at the bottom surface, as shown in Figure 4(d) [144]. The beam refracting from the sidewalls was shown to be the primary cause of the damage lines in laser-cut samples [144]. These

damages could be mitigated by optimizing the polarization angle, immersing the bottom surface of the sample in the liquid, or tilting the sample [152,153].

Most scientific works use the TDC due to its versatility, as various materials can be processed [154]. However, the material removal efficiency is limited due to the interaction of the laser pulse with the plasma and the removed material [155–157]. The plasma not only absorbs the subsequent pulses but also increases the plasma expansion towards the laser source, preventing laser penetration to the sample [156]. Thus, plasma with an elongated shape is formed [156].

Some TDC issues can be mitigated by submerging the sample into still water or forming a flowing water layer on top of the sample with the method called water-assisted top-down cutting (WATDC) [144,158]. Water helps to reduce debris shielding as the ablated material is removed more efficiently due to increased pressure of plasma, stronger shockwaves, and the impact of the cavitation bubbles [5]. In addition, steeper sidewalls are produced [159], allowing the usage of narrower cutting widths [5]. Furthermore, the excessive heat is more efficiently removed from the interaction zone, as water has a higher specific heat capacity than air. As a result, higher cutting throughput can be achieved as higher power can be applied without shattering the sample [160]. Additionally, better heat dissipation results in higher flexural strength of the samples [5]. Finally, water can also serve as a buffer layer for inducing filamentation, used for cutting [141].

1.6.4. Bottom-up cutting

Transparent materials with good front surface quality and low reflectance can be machined by focusing the beam to the bottom surface. The method is called bottom-up cutting (BUC), as material removal begins at the bottom towards the front. By focusing the beam to the bottom surface of the sample, the beam interaction with already milled walls is avoided, allowing for the formation of straight walls [5,161]. For this reason, thicker materials do not require such a drastic increase in cutting width as the TDC. Therefore, the bottom-up approach is also applied to materials thicker than 1 cm [162,163]. It should be noted that BUC is not limited to straight walls, as slanted and even perpendicular channels can be formed [161,162,164].

BUC is energetically more efficient than TDC due to several factors. First, the beam interaction with the ablation products is mitigated as gravity and generated shockwaves enhance the removal of the ablated particles [5]. Second, plasma formed at the bottom surface heats the surrounding material, increasing the absorption and allowing more energy to be coupled into the

sample [32]. In addition, the absorption front moves towards the laser source, creating partially confined superheated material in the bulk of the material [165]. Finally, the damage threshold of the bottom surface is lower [166]. As the beam travels from a lower (air) to a higher (glass) refractive index medium, the reflected light suffers a phase change of π with respect to the incident light. This results in partially destructive interference of the incident and reflected pulses at the front surface. However, no phase change is induced at the bottom surface as the beam travels from a higher (glass) to a lower (air) refractive index medium. Therefore, the transmitted and reflected pulses form a constructive interference at the bottom surface. The ratio between the damage thresholds of the front $F_{\text{th,front}}$ and bottom $F_{\text{th,bottom}}$ surfaces can be described as [166]:

$$\frac{F_{th,front}}{F_{th,bottom}} = \frac{4n^2}{(n+1)^2},\tag{17}$$

where n is the refractive index of a medium. For a wavelength of 1030 nm, the damage threshold of the front surface is 1.45 and 1.4 times higher than that of the bottom for SLG (n = 1.51) and FS (n = 1.45), respectively.

The bottom-up approach using nanosecond pulses is a common method for processing glass, as it enables the machining of complex shapes at high processing speeds. Due to high thermal stresses, glass fractures into particles whose size increases with vertical speed and can reach up to 240 μ m [31]. This allows for processing glass at a high efficiency of 0.13 mm³/J and achieving 9 mm/s cutting speed for 1 mm thick SLG samples [110,167]. However, ~100 μ m length chippings are formed on both surfaces while the sidewall quality reaches $R_a = 1.4 \mu$ m ($\lambda = 532 \mu$ m) and $R_a = 3.2 \mu$ m ($\lambda = 1030 \mu$ m) [5,110]. The quality can be enhanced at the expense of cutting speed by using shorter pulses, as picosecond pulses resulted in smaller chippings and R_a of 1 μ m for 1030 nm wavelength [5].

1.7. Comparison of the cutting methods

The quality of the glass samples processed with different methods can be seen in Figure 4. The images indicate that the largest chippings are formed with waterjet, diamond saw, and ns-BUC methods (Figure 4(b, c, g)). Despite the visually more appealing images shown in Figure 4(a), the mechanically scribed samples also exhibited poor surface quality, as indicated by

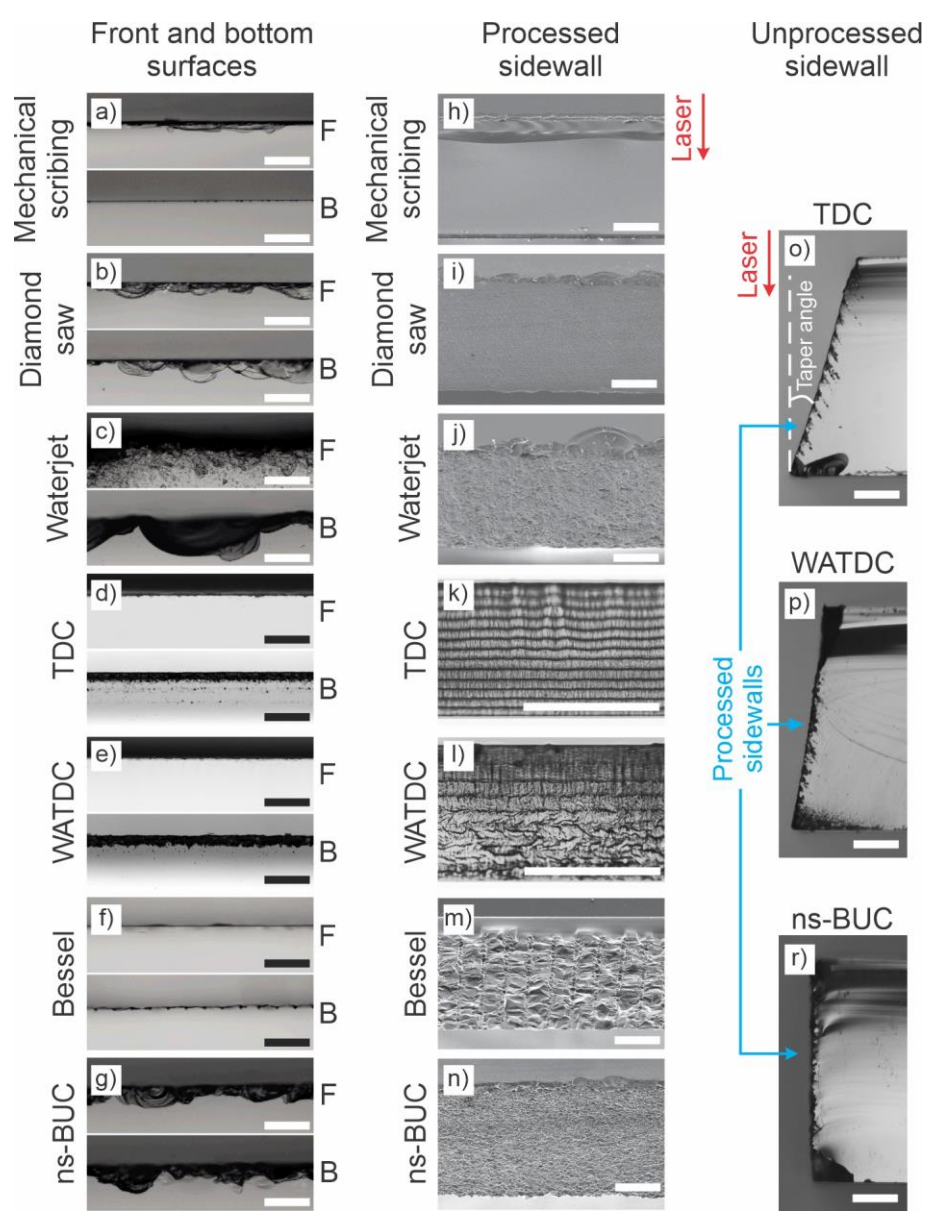


Figure 4. Images of the front and bottom (a–g), processed (h–n), and unprocessed (o–r) sidewall surfaces of the glass samples processed with different cutting methods. The letters F and B on the right of the (a–g) images indicate the front and the bottom surfaces, respectively. The scale bars are 200 μm-length. The images (a–c, f, g, h–j, m, n) were adapted from [110], (d, e, o–r) adapted from [5], and (k, l) adapted from [168]. All images are licensed under the CC BY 4.0.

quantitative chipping measurements performed on 60 samples [110]. The samples processed with Bessel scribing, TDC, and WATDC had the smallest

chippings on the top and bottom surfaces (Figure 4(d-f)). However, the bottom surface of the TDC and WATDC had additional periodical surface damage (Figure 4(d, e)) due to light refraction at the tapered sidewall, which is shown in Figure 4(0, p) [5]. The damaged lines were more pronounced in the samples processed with TDC than in those machined with WATDC. The processed sidewalls of the samples machined with a wateriet, diamond saw, and BUC exhibited a uniformly rough surface throughout the sample depth (Figure 4(i, j, n)). The TDC and WATDC sidewalls had periodically recurring ridges (Figure 4(k, 1)) whose period depended on the distance between the scanning lines and the taper angle of the edge [168]. Notably, no periodic ridges were observed when lower scanning line distances were used [168]. The sidewall of the sample processed with a mechanical scribe and break method featured ~200 um depth median cracks beneath the scribed surface. with a damage-free zone extending beyond (Figure 4(h)). In contrast, the modified zone covered most of the sidewall of the Bessel-scribed sample, with the damage-free zone taking up only a thin layer (Figure 4(m)).

The images of the unprocessed sidewalls (Figure 4(o–r)) show the tapered edge of the processed side with angles of 16 deg and 10 deg for the TDC and WATDC methods, respectively [5]. It is worth noting that the samples cut with a waterjet (Figure 4(c, j)) also produced a taper angle of 4–5 deg [110].

A summary of different glass cutting methods is shown in Table 2. The wire saw, waterjet, TDC, and BUC methods allow the cutting of complex trajectories. However, waterjet and TDC result in V-shaped sidewalls. Therefore, the cutting width must be increased for thicker samples. In contrast, the wire saw and bottom-up approaches allow the forming of straight walls. Despite this, all of the methods allowing the formation of complex trajectories have a non-zero cutting width. Kerf-less cutting can be achieved with controlled fracture and scribe and break approaches. However, these methods are limited to simple contours.

The fastest glass processing reaching m/s is achieved with scribing. However, the mechanical approach leads to large chippings, which significantly increase for thicker glasses. Laser-based scribing can be used to enhance the quality.

In 2020, a study measured the flexural strength of 1 mm-thick SLG samples processed using various glass cutting techniques with a four-point bending setup [110]. These included Bessel scribing with 300 ps pulses at a 1064 nm wavelength, BUC using 12.5 ns pulses and a 532 nm wavelength, BUC followed by additional polishing, mechanical scribing, disk sawing, and waterjet cutting. In most cases, the flexural strength depended on the side of

Table 2. Comparison of different glass cutting methods.

	Method	Advantages	Drawbacks				
	Mechanical scribe	Fast	Simple trajectories				
	& break	Low surface roughness	Two-step				
		Kerf-less	Cutting path deviation				
		cm-thick glass	Tool wear				
			Need for lubricating liquid				
			Need for waste disposal				
_	Disk sawing	cm-thick glass	Simple trajectories				
ica			~mm kerf				
han			Plastic deformations				
Mechanical			Need for grinding and polishing				
_			Tool wear				
	Wire sawing	Complex trajectories	Slow				
		cm-thick glass	Subsurface damage due to vibrations				
			Tool wear				
	Waterjet	Complex trajectories	Taper angle				
		cm-thick glass	Need for grinding and polishing				
			Loud				
	Controlled fracture	Low surface roughness	Simple trajectories				
		Kerf-less	Cutting path deviation				
		cm-thick glass					
	Laser scribe &	Fast	Simple trajectories				
sed	break	Kerf-less	Two-step				
Laser-based		cm-thick glass	Low pitch (filamentation)				
			Complex system (Bessel)				
	Top-down cutting	Complex trajectories	Taper angle				
	(TDC)		< 1 mm thick glass				
	Bottom-up cutting	Complex trajectories	Only for transparent glasses with				
	(BUC)	cm-thick glass	good surface quality				
		No taper angle					

the samples that was subjected to tension. In the bending setup, tensile stresses are generated at the tensioned surface and linearly decrease from this surface to the middle of the samples, where they transition to compressive stresses. Therefore, the surface with better quality will have higher flexural strength. This is observed for Bessel scribed samples for which the cracks reached the bottom surface, but were formed $\sim\!100\!-\!200~\mu m$ below the front surface (seen in Figure 4(m)). This resulted in flexural strengths of 65 and 121 MPa for the bottom and front surfaces, respectively. The difference was also significant for mechanically scribed samples, as the flexural strengths were 165 and 123 MPa for the bottom and front surfaces, respectively. This is attributed to the fact that more defects are formed at the front surface due to scribing (as seen in Figure 4(a, h)). The lowest flexural strengths for either the top or

bottom surfaces were recorded for the samples processed using waterjet (59 MPa), Bessel scribing (65 MPa), and BUC (80 MPa). The mechanical scribing, diamond saw (129 MPa), and additionally polishing samples cut with BUC (148 MPa) resulted in the highest flexural strengths.

The flexural strength of the processed samples was shown to increase with the inclusion of an additional polishing step, which helped reduce surface defects [110]. The strength of samples can also be enhanced by forming chamfers (Figure 5). Samples with sidewalls perpendicular to the front or bottom surfaces are more prone to cracking and chipping upon impact, as stress accumulates at the edges [133]. Therefore, reducing edge angles helps protect the glass and is highly beneficial.

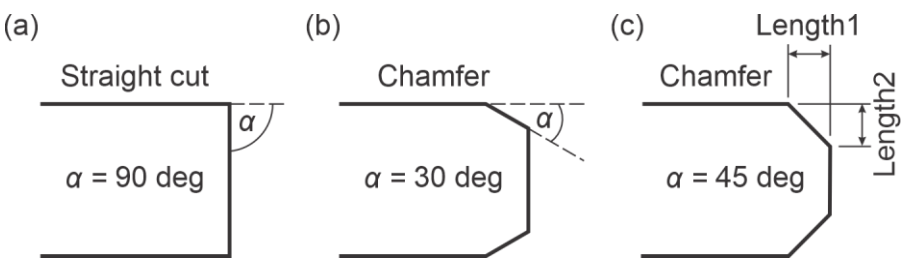


Figure 5. Schemes of straight cut (a), 30 deg chamfered edge (b), and 45 deg chamfered edge (c) geometries.

1.8. Burst mode

Pulsed lasers emit pulses at a repetition rate f_{rep} , where a $f_{\text{rep}} = 100 \text{ kHz}$ results in pulses repeating every 10 µs (shown in Figure 6(a)). In this work, the classical pulsed regime will be referred to as the single-pulse regime. New advances in ultrashort lasers enable new features such as MHz and GHz burst mode operation. The schematics of burst regimes are shown in Figure 6(b). Here, the burst repetition rate f_B specifies how often a pulse packet (burst) repeats. The burst consists of a number of intra-burst pulses repeating at the MHz or GHz intra-burst pulse repetition rate $f_{B\text{-intra}}$. The intra-burst pulses repeat every 470 ps for a burst with $f_{B\text{-intra}} = 2.1 \text{ GHz}$, and every 16 ns for $f_{B\text{-intra}} = 62.5 \text{ MHz}$. State-of-the-art laser sources are capable of emitting even more complicated burst-in-a-burst regimes with GHz bursts inside the MHz bursts depicted in Figure 6(c).

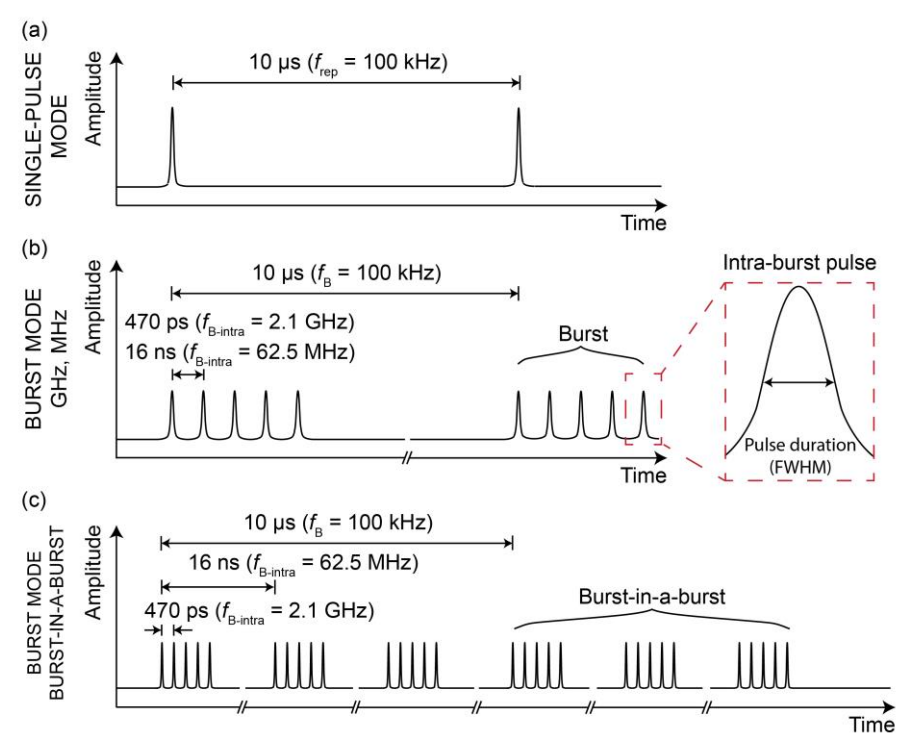


Figure 6. Temporal characteristic scheme of a single-pulse (a), burst (b), and burst-in-a-burst (c) regimes. The scheme depicts regimes with single-pulse and burst repetition rates of 200 kHz and intra-burst repetition rates of 2.1 GHz (for GHz burst) and 62.5 MHz (for MHz burst). Part (b) depicts GHz and MHz bursts consisting of 5 pulses, and part (c) illustrates a burst-in-a-burst regime with GHz bursts consisting of 5 pulses repeated 3 times at a MHz rate.

The burst modes are characterized by the burst and intra-burst pulse repetition rates, number of pulses in a burst, amplitude slope of intra-burst pulses (envelope or shape of a burst), pulse duration, and burst energy.

The burst mode has been highly explored in laser machining after Kerse *et al.* published "ablation cooled" material removal using MHz and GHz bursts [7]. The authors have shown that a high repetition rate allows ablating the material before the residual heat deposited by the previous pulses is diffused. Thermal relaxation time is proportional to δ^2/D , where δ represents the longitudinal or transverse length of interest where thermal diffusion occurs, and D is thermal diffusivity [7,169]. Assuming a characteristic length of 1 μ m and using the thermal diffusivity values for SLG and FS from Table 1, the resulting thermal relaxation time is estimated to be in the range of 1–2 μ s. By using bursts with shorter duration between the intra-burst pulses, the heat

does not have time to diffuse from the 1 μ m² area. The impact of burst mode on glass processing will be discussed in the following paragraphs.

The milling efficiency of FS via the top-down approach increased twice with MHz bursts and 7 times using GHz bursts compared to the single-pulse regime [169,170]. More pulses per burst resulted in a lower damage threshold and increased surface roughness [169]. The surface roughness indicated that with a low number of pulses per burst, the material is removed via gentle ablation. In contrast, a high number of intra-burst pulses resulted in coarse ablation dominated by breaking out of the surface [169]. The improved material removal rate and higher surface roughness for a higher number of intra-burst pulses were also demonstrated for SLG and sapphire samples [171].

Top-down percussion drilling using burst regimes has attracted much attention in recent years, as high-aspect-ratio drilling has been demonstrated in SLG, FS, sapphire, borosilicate (BS), and silicon [172,173]. At the same burst energy, burst repetition rate, and focusing conditions, the single-pulse regime allowed for reaching ~ 0.2 mm, MHz burst mode -0.4 mm, and the GHz mode – 1 mm depth holes in FS [14]. The GHz bursts improved the quality of the holes and allowed for reaching the highest aspect ratios of 150 [14]. It was shown that the number of pulses per GHz burst has no significant impact on the quality and morphology of holes [174]. However, a smaller number of intra-burst pulses resulted in deeper holes, while a higher number of intra-burst pulses resulted in a higher drilling rate [174]. The pumpprobe experiments have shown that with the GHz burst mode, the drilling stops as soon as the plume reaches the bottom surface [175]. Therefore, the diameter of the outlet is smaller than that of the inlet. This restriction can be overcome by adding a material layer underneath the bottom surface, allowing the hole to maintain a similar diameter along its full length [175].

A recent study has demonstrated that high aspect ratio holes can be efficiently produced in silica glass using double Bessel pulses consisting of picosecond and microsecond pulses [176]. Pump-probe experiments revealed that the picosecond pulse creates an elongated high-absorption zone lasting at least 1.8 ns. Another study has shown that by using 5 ps pulses, the filament-induced plasma absorption in silica glass reaches its peak at a pump-probe delay of 4 ps, which fluctuates and lasts for approximately 800 ps, after which it starts to decay with a decay time constant of around 5 ns [36]. The decay was approximately $5 \cdot 10^4$ times slower than that of the plasma filament formed with femtosecond pulses, attributed to the high electron density [36]. The eventual disappearance of the zone indicated that the changes in material property were transient. This high-absorption zone is attributed to the presence

of excited electrons, self-trapped excitons, and color centers [176,177]. Ultrahigh-speed machining of high aspect ratio holes in transparent materials is made possible by the efficient absorption of the microsecond pulse within this transient high-absorption zone induced by the picosecond pulse [176]. Absorption of the µs pulses by the plasma filament was observed when the delay between pulses did not exceed 360 ns [36].

The burst mode can also enhance the formation of volumetric modifications. The length of a crack formed in SLG with high NA increased from $20~\mu m$ to $50~\mu m$ by changing the single-pulse regime to a MHz burst consisting of 4 pulses [178]. Additionally, the MHz burst has been shown to increase the longitudinal length of modification formed in SLG via filamentation [179].

The numerical simulations and experimental results presented by Mishchik *et al.* have shown that the burst mode enhances energy deposition via Bessel beam due to accumulation effects [138]. The burst modes are also shown to improve the quality of Bessel-scribed samples. J. Liu *et al.* have demonstrated the sidewall surface of $R_a = 0.16 \,\mu\text{m}$ for 1 mm-thick SLG samples scribed with MHz bursts consisting of 2 pulses [180]. P. Balage *et al.* have shown that the GHz burst allows reaching $S_a = 0.6 \,\mu\text{m}$ and $S_a = 0.3 \,\mu\text{m}$ in 1 mm-thick SLG and 0.3 mm-thick BS glasses, respectively [139]. Furthermore, the authors have shown that GHz bursts result in better surface quality compared to MHz bursts. J. Li *et al.* have shown that the MHz burst mode enhances the edge quality and flexural strength for filament-scribed samples [122].

B. Stepak *et al.* used a DOE shaper to form a Bessel-like zone in the glass [12]. It was shown that longer pulse durations and a higher number of pulses per MHz burst result in omnidirectional cracks. The omnidirectional cracks began to align along the scanning line for low modification center-to-center distances, allowing for the cleaving of glasses (BK7, SLG) and polymers (PMMA, PET).

1.9. Polarization-related effects

Numerous studies have demonstrated the impact of linear polarization on transparent material machining. Some studies report that modifications extend along the polarization direction [181], while others reveal structures oriented perpendicular to it [182]. This subsection provides a comprehensive review of these studies to enhance the understanding of the underlying phenomenon.

Femtosecond pulses enable the formation of polarization-dependent periodic self-organized sub-wavelength structures in transparent materials [182]. The first report on nanogratings is considered to be the study

done in 1999 by Kazansky et al., where anisotropic scattering from the femtosecond-irradiated area was observed [183]. However, only in 2003, with the application of the scanning electron microscope (SEM), were the first images of the periodic structure obtained [184]. The structures were formed in the focal plane perpendicular to the laser propagation, with the nanograting array oriented perpendicular to the linear polarization. Scientific works demonstrate that the nanogratings can cause the formation of local stress up to several GPa [185,186]. The stress distribution is asymmetric and dependent on the polarization angle with respect to the writing direction [187,188]. The phenomenon was assumed to be caused by the expansion of each structure in the nanograting, creating pressure on its edges [188]. The highest stresses in FS were formed with polarization set perpendicular, and therefore, the nanogratings were oriented along the scanning line [188]. The full understanding of the nanograting formation mechanism is not yet clear. However, some models and hypotheses have been proposed. Shimotsuma et al. have suggested that nanogratings form when the multiphoton absorption induced electron plasma interferes with the incident light [184]. Taylor et al. have suggested that the microscopic defects result in spherical nanoplasmas, which start to elongate perpendicularly to the polarization due to field enhancement at the edges [182]. The nanogratings are suggested to be formed due to the interference between the incident beam and the light scattered from the induced plasma planes [182].

Nanogratings formed in transparent materials such as FS, BK7, LiF, and sapphire can function as microlenses [189]. Guo *et al.* demonstrated that microlenses fabricated using femtosecond pulses affect the beam divergence only along the direction of the linear polarization used during their formation [190]. In contrast, microlenses created with picosecond pulses influence the beam divergence both along and perpendicular to the direction of the polarization. This difference was attributed to distinct carrier excitation mechanisms: multiphoton ionization (femtoseconds) generates free carriers in a more controlled, polarization-dependent way, while avalanche ionization (picoseconds) results in isotropic carrier distributions due to inverse bremsstrahlung collisions.

Li *et al.* have formed nanoholes elongated perpendicular to the polarization [191]. The nanoholes were formed in a glass substrate coated with titanium oxide using femtosecond pulses via a far-field-induced near-field breakdown method. The process starts with the formation of a nanohole via multiphoton absorption. At the edges of the hole, the optical near-fields are formed. The near-fields from the opposite edges will be constructively enhanced if the hole is sufficiently small (diameter << λ). The light intensity

enhancement is reduced from 1.3 to 1.15 times as the diameter of a nanovoid increases from 40 to 200 nm [192]. Once the seed is formed, the energy of the second pulse will be deposited in an elongated zone perpendicular to the polarization due to a larger near-field enhancement. With each subsequent shot, the cross-section of the nanohole becomes more elongated perpendicularly to the linear polarization [191,193]. Li *et al.* have demonstrated the dicing of crystals and glasses by utilizing an SLM to form an elongated beam and by generating high aspect-ratio nanostructures with polarization-controlled cross-sections [193].

Guay et al. have formed craters in poly-methyl methacrylate (PMMA) polymer, which were elongated along the linear polarization [194]. The authors suggested that polarization-dependent ablation occurs due to the interaction of the laser pulse with the plasma created by the leading edge of the pulse. This interaction results in local field enhancements parallel and perpendicular to the laser polarization for overcritical and undercritical plasma densities, respectively. Simulations of laser-induced damage in FS also showed an elongation of the plasma cross-section perpendicular to the polarization direction, attributed to field enhancement effects [195]. The asymmetry becomes more pronounced at higher NA [195].

L. Rapp *et al.* used single femtosecond pulses (140 fs) shaped into high-angle Bessel beams with SLM to create high aspect ratio (100:1) voids in sapphire crystal [181]. The cross-section of the void was asymmetric, with the major axis oriented along the linear polarization. The anisotropy of the sapphire sample did not influence the asymmetry of a void, as the major axis of the cross-section followed the rotation of the polarization, while the sample rotation had no effect. In addition, the authors reported that the channels formed with a longer pulse duration of 3 ps exhibited circular cross-sections regardless of the polarization angle.

In later experiments, L. Rapp *et al.* investigated crack formation and cleaving of the sapphire samples [196]. The study was conducted using the same laser system, except that higher pulse energies were employed to form cracks. The polarization impact on cracks was inspected for the femtosecond pulses. Despite the angle of linear polarization, the cracks were always oriented along the crystallographic axis. The cracks were either one-directional or two-directional. Unidirectional cracks formed only when the sample was translated along one of the crystallographic axes, with the polarization set orthogonally to the translation direction. The three main parameters controlling the crack direction for femtosecond pulses were shown to be the crystallographic axes, polarization angle, and scanning direction. The authors have demonstrated that the crack morphology strongly depends

on the pulse duration—short pulses of up to 650 fs create one-directional cracks, while long pulses result in cracks with up to three different directions. Increasing the pulse energy to $60~\mu J$ resulted in longer cracks; however, no impact on crack morphology was observed.

Yamada et al. used low NA to induce refractive index changes in silica glass via filamentation [197]. The samples were polished and etched to reveal the cross-sections of the refractive-index changes. The cross-sections of the modified zones were asymmetric, with the long axis of the ellipse parallel to the polarization. The authors proposed interpreting the beam propagation as self-trapping within a waveguide, demonstrating that the effective beam widths vary depending on the polarization orientation. Yu et al. have also shown that the filament-induced damage depends on polarization [198]. Using femtosecond pulses, the authors investigated the damage cross-sections in FS. The damage was elliptically shaped near the filament starting point, with the long axis oriented along the laser polarization. The damage zone turned into a circle at the bottom of the filament. Furthermore, they have shown that loosening the focusing conditions results in almost circular damage, regardless of the polarization. The elliptical shape was attributed to the polarization vector effect during the self-focusing of light. The same effect was addressed in Sub-subsection 1.4.2, where it was noted that linear polarization can result in a MF pattern, with beams split into two filaments positioned either along or perpendicular to the linear polarization [54].

The elongation along the polarization was also seen for 3D polymerized suspended bridges when using a high NA of 1.4 [199]. The elongation along the polarization direction in high NA focusing can be predicted using vectorial Debye theory and may also be influenced by polarization-dependent differences in refractive index and absorption arising from angle-dependent Fresnel coefficients [199]. The authors suggested that heat conduction is also responsible for the effect. Under the external field, heat conduction becomes anisotropic as electrons preferentially move along the field direction [199]. The oscillating high-frequency field results in suppressed heat diffusion along the polarization and, thus, an elongated heat-affected zone [200]. The same explanation was used to account for the observed variations in the period, width, and tilt of nanogratings formed in FS with NA of 0.4 and 0.6 [201].

2. EXPERIMENTAL METHODS AND CHARACTERIZATION TECHNIQUES

2.1. Laser microprocessing setup

The research was carried out with the experimental setup depicted in Figure 7. The laser source provided linear polarization, which was altered with the optical waveplates. In the experiments, $\lambda/2$ and $\lambda/4$ waveplates were used to adjust the linear polarization angle or convert it to circular polarization. The beam diameter was increased with either a variable beam expander (S6EXZ5310/328, Sill optics) or a Galilean telescope created from planoconcave and plano-convex lenses (focal lengths of f = -50 mm and f = 75 mm). The beam of ~ 8 mm diameter was focused using an f = 100 mm telecentric f-theta lens, resulting in a system numerical aperture (NA) of approximately 0.04. The laser beam position in the X and Y axes within the 70 x 70 mm² scan field was controlled with different IntelliSCAN 14 series (Scanlab) galvanometric scanners. For an f = 100 mm telecentric f-theta lens, the beam scanning speeds were limited to 9 m/s (Section 3, excluding Subsection 3.2), 6 m/s (Subsection 3.2), or 10 m/s (Sections 5 and 3). The sample could be moved along the X and Y axes within a 300 mm range using linear stages (8MTL165-300, Standa). The position of the scanners and

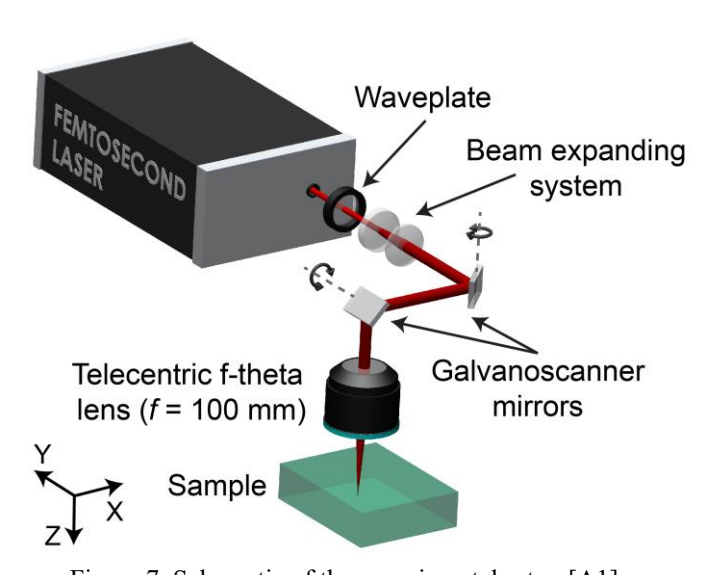


Figure 7. Schematic of the experimental setup [A1].

telecentric f-theta lens in the Z axis was changed using the linear stage (PRO165LM, Aerotech).

In BUC (Section 3) and scribing (Section 5) experiments, the samples were positioned in such a way that there would be an air gap between the rear surface of the samples and the positioning stages. The debris produced in BUC was removed with the help of a fume extraction system (AD Oracle iQ, Bofa International Ltd).

2.1.1. Laser sources

The research was conducted with three different (#1–3) Carbide series (Light Conversion) lasers using parameters listed in Table 3. The pulse duration τ_p , central wavelength λ , and beam quality parameter M^2 were specified at the single-pulse regime by the laser manufacturer. The average power was measured using a Centuri (Ophir) power meter with a thermopile sensor 30(150)A-BB-18 (Ophir). The sensor can measure the average power of up to 30 W. For higher powers, the burst repetition rate was lowered with a pulse picker integrated into the laser. In that case, the burst energy E_B was calculated by dividing the measured power by the corresponding burst repetition rate f_B

Table 3. Parameters of the laser sources used for experimental parts. Rectangles of a distinct shade of gray separate the three different (#1–3) laser sources. Here τ_p is pulse duration specified at the full width at half maximum (FWHM) intensity level at a single-pulse regime, λ – central wavelength, $P_{\rm ave}$ – average power of a laser source, $f_{\rm B}$ – burst repetition rate, $E_{\rm B}$ – energy of a burst or a BiBurst, $f_{\rm B-intra}$ – intra-burst pulse repetition rate.

	Laser	τ _p , ps	P _{ave} , W	f _в , kHz	<i>E</i> _B , μJ	Intra-burst period $(f_{\text{B-intra}})$	Burst regimes	Experiment	Section
[²≈ 1.1	#1	5–20	<36	200	<180	404 ps (2.5 GHz)	P25N1, P30N1	BUC (SLG)	3 (excl. 3.2)
7, 1	#1 15		34	200	170	404 ps (2.5 GHz)	P40N2	BUC (SLG)	3.2
nn				600	57	16 ns (62.5 MHz)	P1N1	Top chamfer	
1030 nm, $\mathrm{M}^2\approx$				600	57		P2N2	Bottom chamfer	
Carbide, $\lambda = 1$	#2	0.221	<17	100	<170	465 ps (2.2 GHz) 16 ns (62.5 MHz)	P(1–20)N1, P1N(1–20)	Single-shot modifications (FS)	4
	#3	0.176–8	<35	100	<350	470 ps (2.1 GHz) 15.8 ns (63.3 MHz)	P10N(1-10)	Single-shot modifications (SLG)	4
	#3	0.176–4	<30	100	200; 300	470 ps (2.1 GHz) 15.8 ns (63.3 MHz)	P10N5	Scribing (SLG)	5

(fundamental burst repetition rate divided by the pulse picker number).

The laser source provided GHz and MHz burst modes, as well as a burst-in-a-burst (BiBurst) regime, featuring GHz bursts within MHz bursts. The intra-burst pulse period was 404–470 ps and ~16 ns for GHz and MHz bursts, respectively. In the standard laser mode, the bursts consisted of up to 10 pulses. However, non-standard regimes with more than 10 pulses per burst were accessed for lasers #1 and #2 in experiments presented in Section 3 (BUC) and part of Section 4 (single-shot modifications formed in FS).

For simplicity, the number of pulses per GHz and MHz burst will be written next to P and N letters, respectively. For a BiBurst regime, the letter N represents the number of pulse packets repeating at a MHz rate. Therefore, a pulse packet of 10 pulses separated at the ps-scale (GHz burst), repeating 5 times at the ns-scale (MHz burst), will be written as P10N5.

In this work, the term single-pulse refers to the P1N1 regime, while the term single-shot denotes a single irradiation, consisting of either one pulse (for single-pulse), a burst (for GHz or MHz burst), or a BiBurst.

The temporal characteristics of bursts were measured using a high-speed detector (D-15ir, Picometrix) and an oscilloscope (DPO72004C, Tektronix). Oscillograms of P10N1, P1N10, P25N1, P30N1 bursts, and P10N5 BiBurst regimes are shown in Figure 8. For the standard laser burst and BiBurst regimes consisting of up to 10 pulses per MHz or GHz burst, the oscillogram amplitudes of the intra-burst pulses were quasi-equal except for the last pulse or pulse packet, having 3 times higher amplitude (Figure 8(a-c)). This phenomenon was a characteristic of the used laser source burst envelope shape parameter set and remained constant for the standard burst regimes. The nonstandard bursts consisted of varying amplitude intra-burst pulses (Figure 8(d, e)). Furthermore, an additional pre-burst was formed before the original. The pre-burst consisted of 10 and 15 pulses for burst regimes of P25N1 and P30N1, respectively. The time between the last intra-burst pulses of the additional and the original bursts was 16 ns. As the effects of the additional burst and varying amplitude intra-burst pulses are unknown, most results in this work are provided regarding only the full burst energy. In the case of a BiBurst, its total energy will also be referred to as the burst energy.

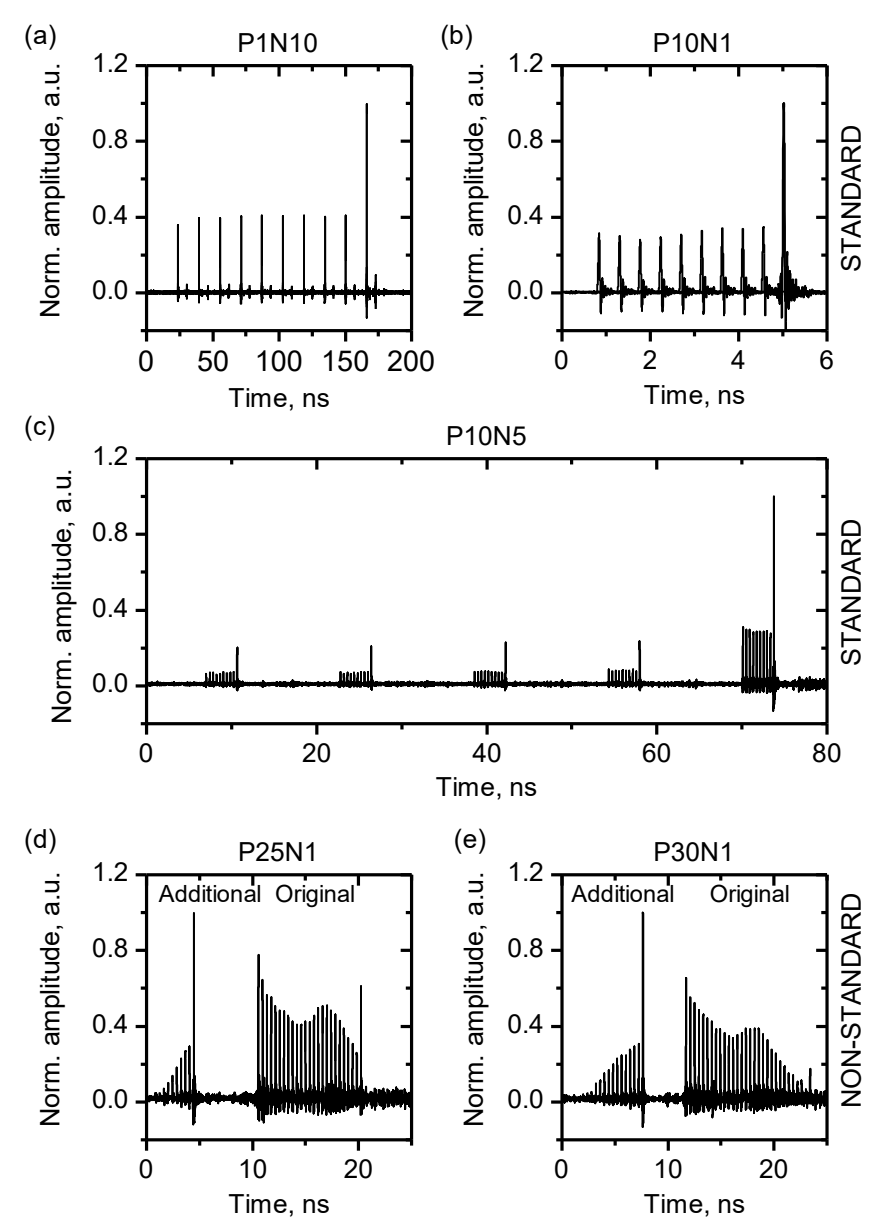


Figure 8. Temporal characteristics of standard P1N10 (a), P10N1 (b) burst and P10N5 (c) BiBurst and non-standard P25N1 (d), P30N1 (e) burst regimes. The measurements correspond to the laser sources #1 (d, e), #2 (a, b), and #3 (c). The original and additional pre-bursts are indicated in the text above [A1–A3].

2.1.2. Beam characterization

The spatial intensity distribution of the laser beam in the XY plane after the focusing lens was measured at different Z positions around the focus (Figure 9) using a beam profiling camera (Beamage 4-M, Gentec-eo). The Z=0 mm position was defined as the point where the beam exhibited the lowest ellipticity, calculated by dividing the beam diameter along the major axis by the one along the minor axis. The effective pixel size of 5.5 μ m was

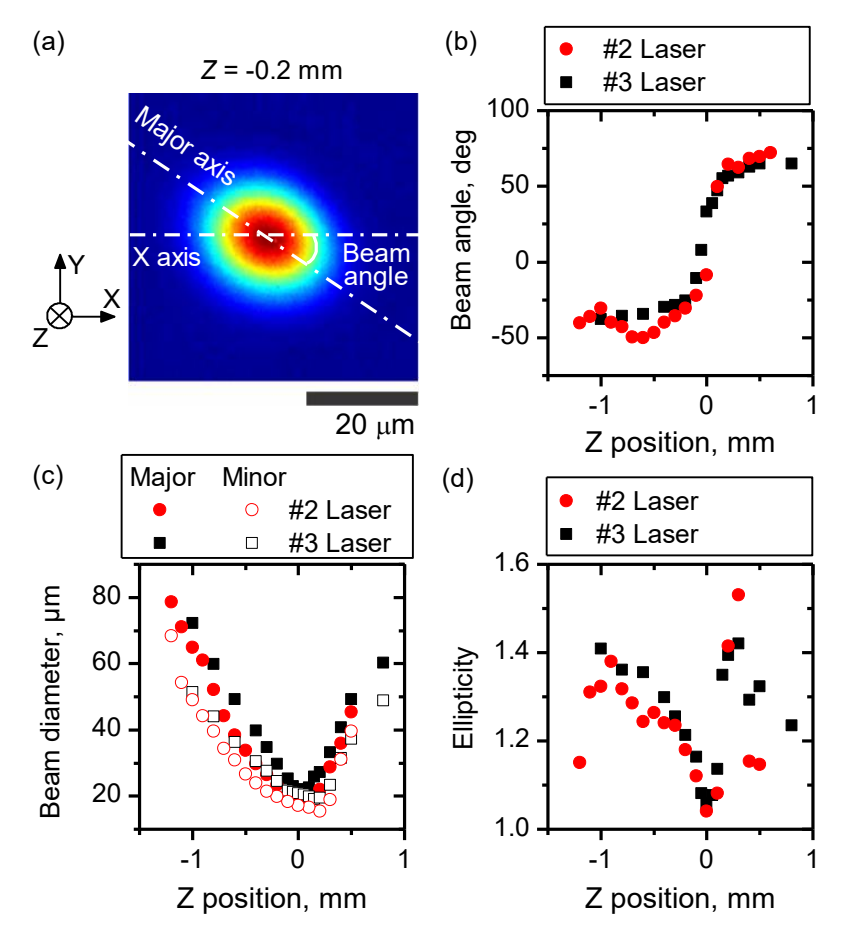


Figure 9. Spatial characterization of the #2 and #3 laser beams. The spatial distribution of the #3 laser beam in the XY plane at Z position of 0.2 mm before the focal point (a). The image contains dashed lines marking the system X axis and major and minor axes of a beam. Laser beam major axis orientation (b), beam diameter along the major and minor axes at the $1/e^2$ intensity level (c), and ellipticity (d) dependence on Z position. The measurement was taken after the focusing lens, with Z positions above the focus set to negative and those below the focus set to positive [A1, A2].

reduced with an additional imaging system, which increased the beam size on the camera 16 and 22 times for single-shot experiments in FS (#2 laser) and SLG (#3 laser), respectively. The presented beam diameters were corrected to match the real dimensions, taking into account the image magnification factor. The beam angle was measured from the system X axis to the beam major axis (Figure 9(a)). The angles with the beam major axis, measured clockwise from the system X axis, were set as negative, and those measured counterclockwise from the X axis were set as positive. This ensured that the angles ranged between -90 deg and 90 deg. The beam major axis was oriented at around -40 ± 10 deg before the focus and at around 60 ± 10 deg after the focus (Figure 9(b)).

The ellipticity reached 1.5 at Z positions ± 1 mm around the focus (Figure 9(d)). Below the focus, the ellipticity increases, reaching a peak at Z = 0.3 mm, after which it starts to decrease. The focus position (Z = 0 mm) was defined as the point of minimum ellipticity. However, due to beam astigmatism, the focus positions of the major and minor axes differ. Consequently, below Z = 0 mm, the beam diverges along one axis while converging along the other, resulting in a peak in ellipticity at Z = 0.3 mm. Beyond this point, both axes diverge, causing the ellipticity to decrease.

The beam diameters were $\sim 20~\mu m$ (at $1/e^2$ intensity level) at the Z position corresponding to the lowest ellipticity (Figure 9(c)).

2.2. Laser processing methods

2.2.1. Bottom-up cutting approach

The BUC experiments were conducted on $100 \times 100 \times 4.8 \text{ mm}^3$ SLG samples by cutting 20 mm diameter circles using a spiral scanning algorithm depicted in Figure 10(a). In the XY plane, the laser beam was scanned continuously inwards and outwards with respect to the circle center, with an additional repetition of the inner and outer circles. In the following text, the distance between the sequential craters in a scanning trajectory and scanning lines will be referred to as pitch.

The cutting width (kerf) was slightly changed depending on the pitch value. The kerf had to be a multiple of the pitch to sustain the continuous beam scanning without any jumps. Therefore, the kerf value was equal to 200 μm or slightly higher, with the least difference of the pitch multiple and 200 μm . The maximum kerf value of 225 μm was used with a 45 μm pitch. The 200 μm kerf was chosen as it was wide enough for the dust to escape without clogging the channel.

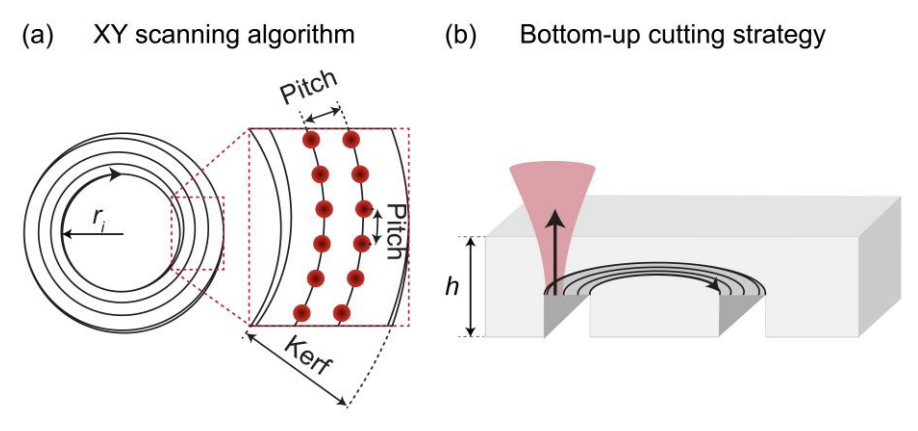


Figure 10. Beam scanning algorithm (a) and cutting strategy (b) [A3].

At first, the laser beam waist was positioned lower than the bottom surface of the sample to prevent sample cracking and further destruction. The additional offset depended on the burst energy and varied between 50 µm and 1.2 mm. After positioning the beam waist, scanning was carried out continuously while the laser focus was simultaneously raised at a constant vertical speed (Figure 10(b)). Higher vertical speed has been shown to result in the removal of larger particles [31], which in turn contributes to higher cutting speeds.

2.2.1.1. Chamfer formation

BUC with chamfer formation was conducted on 2.3 mm-thick SLG samples by cutting 32 mm diameter circles and forming chamfers with $\alpha = 45$ deg (Figure 5) and 300 μ m width (Length1 in Figure 5) and depth (Length2 in Figure 5). The sample cutting and chamfer formation scheme is shown in Figure 11. The beam is scanned in a spiral algorithm shown in Figure 10(a). First, the bottom chamfer is formed using parameters for high-quality ablation. Once the bottom chamfer is complete, the sample is cut through its

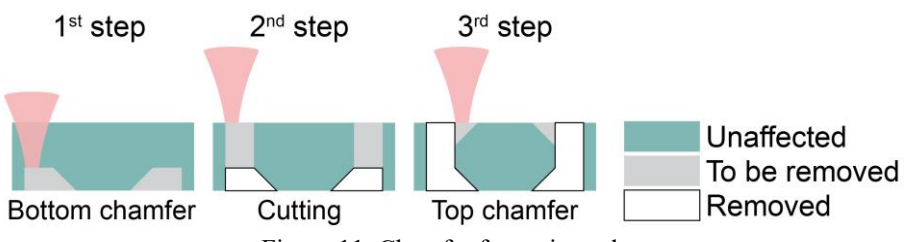


Figure 11. Chamfer formation scheme.

full thickness using the parameters for the high-throughput regime. Finally, the top chamfer is formed with parameters optimized for high quality.

The chamfers were formed by increasing the inner diameter of the scanning zone after each layer. After each scanning layer, the Z position was lifted upwards or downwards for the bottom and top chamfers, respectively. It should be noted that the bottom chamfer was created by additionally ablating the cutting area to enhance the initiation of the following cutting process. Therefore, a greater volume was removed to form the bottom chamfer (8.1 mm³) than for the top chamfer (4.5 mm³).

2.2.2. Modifications formation via single-shot

 $100 \times 100 \times 4.8 \text{ mm}^3 \text{ SLG}$ and $150 \times 150 \times 6.3 \text{ mm}^3 \text{ FS}$ glasses were used for single-shot modification experiments. An additional set of FS samples, sized $20 \times 1 \times 6.3 \text{ mm}^3$ with polished sidewalls, was used to evaluate longitudinal modifications.

The modifications were formed with a single irradiation, consisting of either one pulse (for single-pulse), a burst (for GHz or MHz burst), or a BiBurst. These single-shot modifications were formed by focusing the beam at depths of 1.45 mm (for FS) and 1 mm (for SLG) (Figure 12). The focus position Z_f , defined by linear optics, was calculated by multiplying the mechanical shift in the Z axis by the refractive index of a sample ($n_{FS} = 1.45$ or $n_{SLG} = 1.51$).

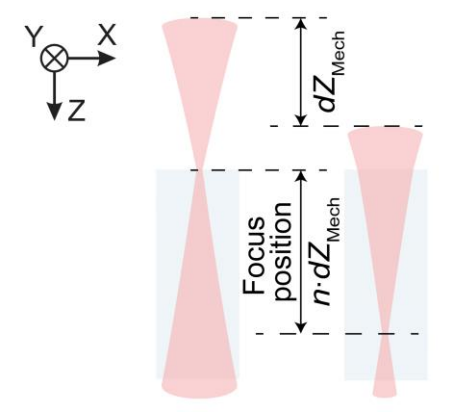


Figure 12. The focus position (Z_f) scheme for modification formation. Here, the refractive index of a sample is denoted as n, and the mechanical shift in the Z axis – $dZ_{Mech}[A1]$.

2.2.3. Laser scribing and separation

The scribing experiments were conducted using the P10N5 BiBurst regime on $76 \times 25 \times 1.1 \text{ mm}^3$ SLG samples by focusing the beam to a specific depth and scanning it over a 25 mm-length line positioned in the middle of the 76 mm side at a speed of v_{scan} . The focus position given in this work corresponds to the physical distance from the front surface of the sample to the beam waist (as shown in Figure 12). The related mechanical shift of the stage was adjusted considering the refraction of light at the air-glass boundary.

For every parameter set, 5 samples were separated with a four-point bending setup (Figure 13(a)). Samples were positioned by orienting the modified part towards the tensioned zone and centering the modification line between the supports. The inner supports were lowered at a constant speed, applying a loading rate of 0.39 MPa/s to the samples. The peak breaking force F was recorded using a digital dynamometer (FMI-B50C1, Alluris). The separation stress was calculated using the formula below [202]:

$$\sigma_b = \frac{3F(L-l)}{2hh^2},\tag{18}$$

where L and l are distances between the outer and inner supports, respectively, h denotes the sample thickness, and b – the width of the sample.

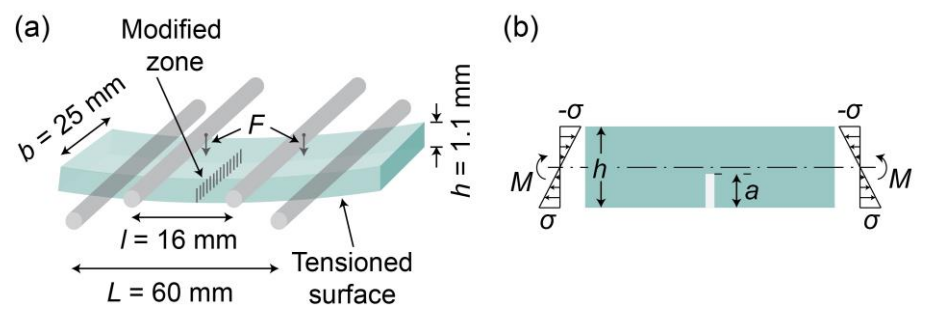


Figure 13. Four-point bending setup used in the separation step (a) and scheme for the separation stress simulation (b). Crack depth is denoted as a, h is sample thickness, M – torque, and σ – induced stress (tensile on the bottom and compressive on the top) [A1].

2.2.3.1. Separation stress simulation

The separation stress was simulated relying on bending a single-edge-notched specimen depicted in Figure 13(b). For such a configuration, the stress intensity factor in the opening mode K_I is given by [203]:

$$K_I = \sigma_b Y \sqrt{\pi a},\tag{19}$$

where σ_b defines the applied bending stress and a is the depth of a crack (equal to the longitudinal length). The geometry factor Y can be calculated as [203]:

$$Y = \sqrt{\frac{2h}{\pi a} tan \frac{\pi a}{2h}} \frac{0.923 + 0.199 \left(1 - sin \frac{\pi a}{2h}\right)^4}{cos \frac{\pi a}{2h}},$$
 (20)

where h defines the sample thickness.

In the inert condition, it was assumed that a glass sheet is separated when the stress intensity factor is equal to the critical value $K_{\rm Ic}$, which is 0.75 MPa m^{1/2} for SLG [38]. Therefore, the separation stress was calculated as:

$$\sigma = \frac{K_{Ic}}{Y\sqrt{\pi a}}. (21)$$

To take into account the sub-critical crack growth at $K_{th} < K_{I} < K_{Ic}$ [204], the propagation of a crack was numerically simulated according to [205]:

$$a = a_i + v_0 \left(\frac{K_I}{K_{Ic}}\right)^n \Delta t, \tag{22}$$

where a_i is the initial depth of a crack at a calculation step, $v_0 = 6$ mm/s, and n = 16 in ambient air [38]. The time interval Δt was 0.1 ms. The stress increased linearly over time at a rate of 0.39 MPa/s. Simulations were terminated when the critical stress intensity value was reached. The threshold stress intensity factor K_{th} was equal to 0.2 MPa m^{1/2} [38].

2.3. Characterization methods

2.3.1. Sample quality

The edge quality of the cut and scribed and separated samples was evaluated by measuring the length of the largest chipping on the top and bottom surfaces using an optical microscope (OM). The top surface corresponded to the one directly facing the incident beam.

The sidewall surface quality of the processed samples was assessed by measuring average roughness (R_a) and waviness (W_a) with an optical profilometer (OP). The linear profiles were measured using cut-off wavelengths of 0.8 µm (for R_a < 2 µm) and 2.5 µm (R_a > 2 µm) and an evaluation length of 18 mm, following the recommendations in ISO 4287:1997.

For the samples processed with BUC, one sample was investigated for each different parameter set. For the scribed samples, 5 samples were analyzed for every parameter set, from which mean and standard deviation values were calculated. Figures representing the quality of the scribed and separated samples are presented in the (mean \pm a standard deviation) format.

2.3.2. Process productivity

The BUC was evaluated by calculating the cutting speed v and linear cutting efficiency η :

$$v = \frac{2\pi r_i}{t},\tag{23}$$

$$\eta = \frac{v}{P_{\text{ave}}},\tag{24}$$

where r_i is the inner radius of the cut (Figure 10(a)), h – the thickness of the sample (Figure 10(b)), t – cutting time, and P_{ave} – laser average power. It should be noted that t corresponded to the time measured from the start to the end of the cut.

Linear cutting efficiency represents the number of millimeters of material that can be cut per second using 1 W of laser power for a sample of a specific thickness, indicating how efficiently the laser energy is converted into cutting

performance. The units of linear cutting efficiency (mm/ $(W \cdot s)$) are simplified to mm/J (millimeters per joule).

Most glass processing studies cannot be compared by cutting speed or linear cutting efficiency, as various thickness samples are cut. Alternative figures of merit, taking into account the sample thickness, were used to extend the comparison. The relative cutting speed $v_{\rm rel}$ and efficiency $\eta_{\rm rel}$ were calculated using the formulas provided below:

$$v_{rel} = vh, (25)$$

$$\eta_{rel} = \frac{vh}{P_{2ve}} = \eta h. \tag{26}$$

The relative cutting speed represents the area of a cut edge produced in a unit of time (Figure 14), and the relative cutting efficiency – the area of a cut edge produced with a unit of energy [206].

For scribing, the process productivity was assessed by using the scribing speed instead of the cutting speed. The scribing speed corresponds to the scanning speed for single-pass and half of it for double-pass scribing. The productivity parameters (v, η , $v_{\rm rel}$, $\eta_{\rm rel}$) used to compare the cutting methods were recalculated for scribing by substituting the cutting speed with the scribing speed.

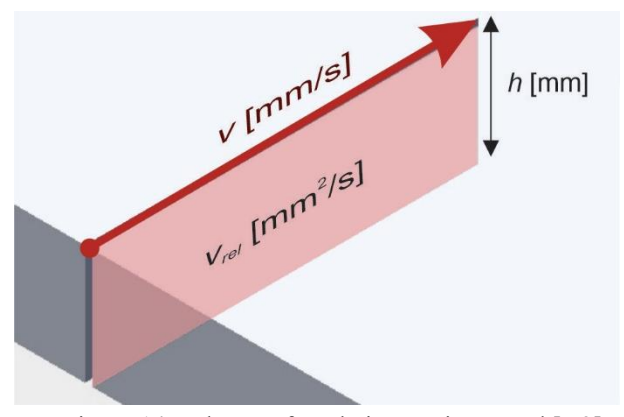


Figure 14. Scheme of a relative cutting speed [A3].

2.3.3. Evaluation of single-shot modifications

Single-shot modifications were inspected with an OM in the transmission regime. Two different modification dimensions were measured: transverse $(L_{\rm T})$ and longitudinal $(L_{\rm L})$ lengths, as illustrated in Figure 15. Transverse modifications (the full extent of cracks) were measured in the plane perpendicular to the beam propagation direction (from the top surface of the sample). The angle α of transverse modifications was measured from the X axis, as illustrated in Figure 15(b). The axis corresponds to the X-direction of both the galvanoscanner and the positioning stages of our system, illustrated in Figure 7. Angles clockwise from the system X axis were set as negative, and counterclockwise from the X axis — positive. It should be noted that transverse lengths and angles varied along the Z axis. Therefore, measurements of transverse angle and length were taken at the Z position where the transverse modification reached its maximum length.

The measurement of longitudinal lengths (the full extent of longitudinal modification) differed for SLG and FS glass samples. For FS samples with polished sidewalls, the longitudinal modifications were evaluated in a plane parallel to the beam propagation direction (from the side surface), as shown

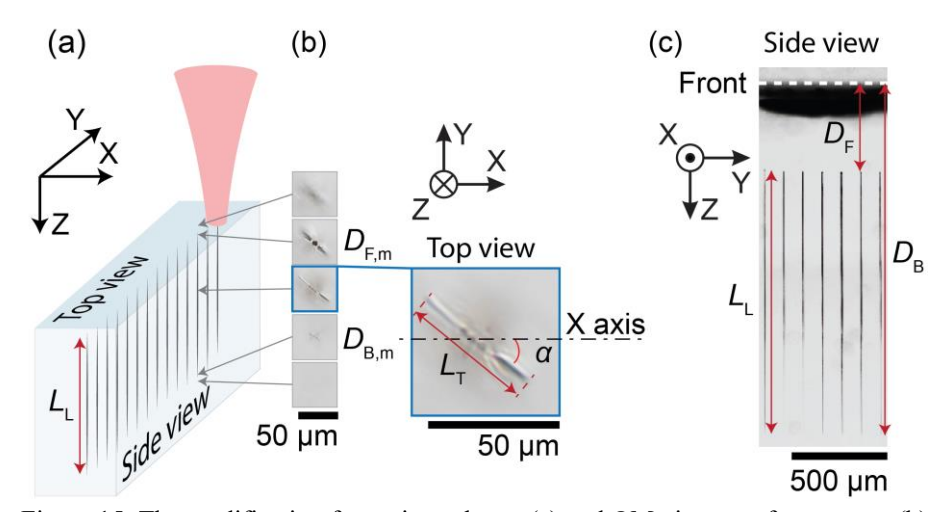


Figure 15. The modification formation scheme (a) and OM pictures of transverse (b) and longitudinal (c) modifications. The longitudinal length is denoted as $L_{\rm L}$, transverse length $-L_{\rm T}$, transverse modification angle $-\alpha$, and distance from the sample top surface to the modifications front $-D_{\rm F}$, and to the modifications bottom $-D_{\rm B}$. $D_{\rm F,m}$, and $D_{\rm B,m}$ are OM Z positions corresponding to the front and bottom of the longitudinal modification. The black dashed line in (b) part denotes the system X axis, and the white dashed line in (c) – the front surface of the sample [A2].

in Figure 15(c). The same measurement method could not be applied to the SLG samples, as their sidewalls had a ground finish. Therefore, for the SLG samples, the measurement was done in the plane perpendicular to the beam propagation direction (from the top surface) using the fine-focus knob method [207]. The simplified measurement scheme is shown in Figure 15(b). The front ($D_{F,m}$) and bottom ($D_{B,m}$) positions of the visible modification were measured by adjusting the Z position with a focus motor (PS3H122R, Prior Scientific). The front position corresponds to the focal plane where the leading edge of the modification first became visible. In contrast, the bottom position corresponds to the focal plane at which the modification is no longer observed. The longitudinal lengths were calculated as the difference between these two positions, multiplied by the refractive index of the sample to account for the difference between the optical path length within the sample and the actual physical depth inside the material.

The depth of field of a 20x objective was 1.2 μ m (1.8 μ m in SLG), while the minimal mechanical step in the Z axis was 2 nm. Therefore, the accuracy of the measured longitudinal length was limited by the depth of the field. It should be mentioned that the longitudinal lengths of the modifications, which were split into a few parts, were measured from the front of the first part to the bottom of the last part.

The distance from the sample top surface to the modification front (D_F) was measured from the side surface for FS. The distance between the modification bottom to the sample front surface (D_B) was calculated by the sum of D_F and L_L . The D_B , D_F , and L_L parameters marked on an OM picture of a sample can be seen in Figure 15(c).

For each parameter set, 10 modifications (for FS and transverse parameters in SLG) or 2 modifications (for longitudinal lengths in SLG) were measured and averaged. Figures are presented in either (mean) or (mean \pm a standard deviation) format.

2.3.4. Characterization tools

A summary of the measuring tools used for each experimental part is presented in Table 4. The surface chippings of the processed samples and the single-shot modification position, length, and angle were measured with an OM. The sidewall surface roughness R_a and waviness W_a were measured using an OP. The particles generated during the BUC process were evaluated with a SEM (Prisma E, Thermo Fisher Scientific).

Table 4. Measuring tools and objectives used for different experimental parts. Here, OM corresponds to the optical microscope and OP-to the optical profilometer.

Measurement (Section)	Measured	Instrument,	Objective		
	parameters	(Model,	(NA, resolution)		
	(Material)	Company)			
Transverse single-shot	Length, angle				
modifications	(FS, SLG)		20x (0.45 NA, 0.24 μm/pixel)		
(Subsection 4.2)		OM (Eclipse			
Longitudinal single-shot	Length (SLG)	LV100NDA,			
modifications	Length (FS)	Nikon)	5x (0.15 NA,		
(Subsection 4.1)			0.96 μm/pixel)		
Scribing and BUC	Chippings (SLG)		υ.96 μπ/ριχει)		
(Sections 5 and 3)	Sidewall surface	OP (S Neox,	20x (0.45 NA,		
(Sections 3 and 3)	quality (SLG)	Sensofar)	1.4 µm/pixel)		

3. BOTTOM-UP CUTTING

In this section, laser burst regimes are used for the BUC of SLG samples. The experimental setup is illustrated in Figure 7. The BUC method is described in Sub-subsection 2.2.1 and the process evaluation is described in Sub-subsections 2.3.1 and 2.3.2. Results provided in this section were published in [A3] research paper.

3.1. Cutting results

The BUC optimization was done for P25N1 and P30N1 burst regimes using different pulse durations (5–20 ps), burst energies (<180 μ J), pitches (5–45 μ m), and vertical speeds (<0.3 mm/s). Pitch and vertical speed were optimized for every pulse duration and burst energy combination, requiring approximately 8 experiments. Optimal pitch allowed for reaching the highest vertical speed, resulting in the shortest cutting duration. This subsection presents the results using the optimized parameters.

The optimal pitch dependence on the burst energy for different pulse durations and burst regimes is shown in Figure 16. The pitch was changed by 5 µm for every set. The value of the optimal pitch increased with the burst energy. Larger energy pulses affect a greater area of the sample [208]; thus, a larger distance is needed to sustain the overlapping of the laser-affected areas. It should be noted that the optimal pitch value may not have been reached for

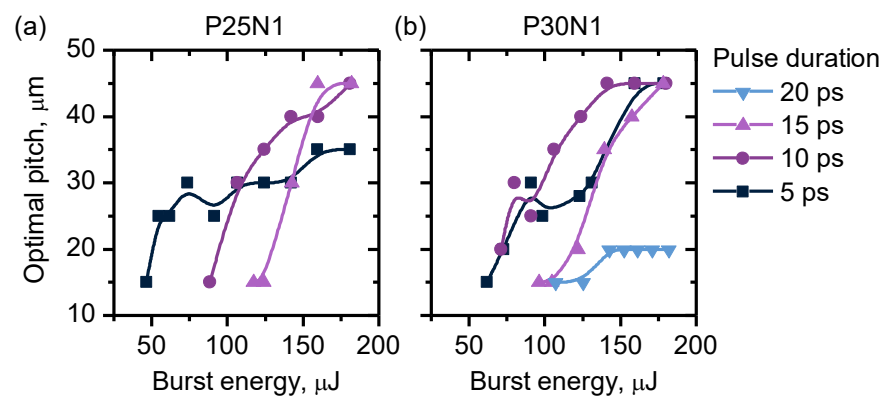


Figure 16. Optimal pitch dependence on burst energy for P25N1 (a) and P30N1 (b) burst regimes using different pulse durations. The lines are added to guide the eye [A3].

some regimes at the highest burst energies because of the maximum pitch value of 45 μ m. This limitation arises from the maximum scanning speed of galvanometer scanners, which is equal to 9 m/s, and the burst repetition rate of 200 kHz. Therefore, more advanced scanners could potentially allow for reaching shorter cutting durations.

The dependence of cutting speed on the burst energy is shown in Figure 17. For longer pulses, higher burst energy was needed to achieve the highest cutting speed. Due to the limited burst energy, it is unclear whether this tendency repeats for the P30N1 regime with pulse durations of 15 and 20 ps. The highest cutting speed of 4.2 mm/s was achieved with 180 μJ energy bursts using the P30N1 regime and 15 ps duration. For the P25N1 regime, which features fewer pulses per burst, a lower cutting speed of 2.4 mm/s was achieved using 10 ps pulse duration and 140 μJ .

To analyze the particles generated during the BUC process, cutting was carried out with the fume extraction system turned off. The regime corresponding to the highest cutting speed was used for the cutting process. After cutting, the dust and particles that settled on the positioning table beneath the sample were collected and examined with a SEM. The SEM images show that the removed particles were tens of µm long (Figure 18). This indicates that the P30N1 burst regime with picosecond pulses results in material removal via fracture. Similar images with µm-length particles are presented in a study where high glass drilling speeds were achieved using 532 nm ns pulses, due to the main material removal mechanism being the ejection of glass particles due to cracking [31].

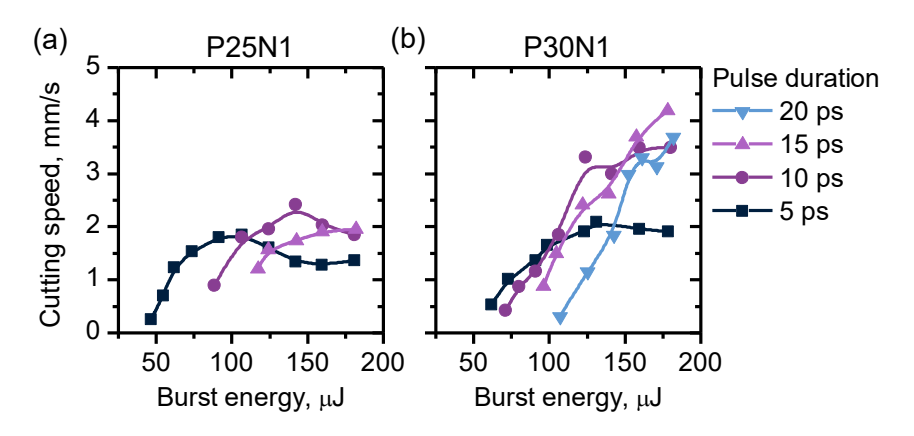
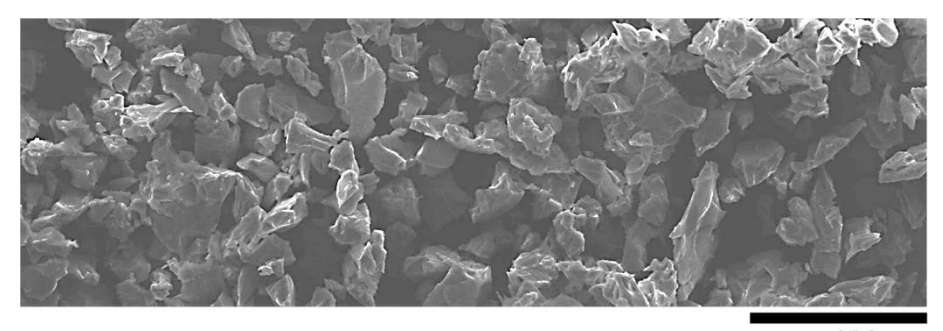


Figure 17. Cutting speed of 4.8 mm-thick glass. The dependence on burst energy for P25N1 (a) and P30N1 (b) burst regimes with different pulse durations. The lines are added to guide the eye [A3].



100 µm

Figure 18. SEM image of the particles removed via BUC. The cutting was performed using a P30N1 regime with 15 ps pulses and a burst energy of 180 μ J.

The linear cutting efficiency dependence on the burst energy is shown in Figure 19. Like the cutting speed, the linear cutting efficiency peaks shifted to larger burst energies for longer pulse durations. For the P25N1 burst regime, the highest cutting efficiency of 0.1 mm/J was achieved using the shortest tested pulse duration of 5 ps, while longer pulses resulted in lower efficiency. However, for the P30N1 burst regime, the highest cutting efficiency of 0.13 mm/J was reached with 10 ps pulses at $E_B = 124 \mu J$, which is 1.6 times higher than the efficiency obtained with 5 ps pulses. Due to the limited power of the laser, it is unclear if further increments in pulse duration could improve cutting efficiency.

To achieve the highest cutting speed, the pulse duration and burst regime should be chosen according to the maximum laser burst energy at a fixed burst repetition rate. The P30N1 regime with 15 ps pulses should be used for the tested burst energies. However, for burst energies lower than $100~\mu J$, the P25N1 regime with 5 ps pulses may be favorable. An alternative approach would be to optimize the burst repetition rate at the parameter set with the highest cutting efficiency. In this case, increasing the repetition rate necessitates higher scanning speeds to maintain the optimal pitch. Therefore, limitations imposed by the scanning system speed may need to be considered.

Higher cutting speed could presumably be achieved with a different experimental setup. As the highest pitch was limited to 45 μ m (for f_B = 200 kHz), faster galvanoscanners allow the use of a higher pitch, which might be optimal for some of the parameter sets used in the experiment. Furthermore, the trend (shown in Figure 17(b) for P30N1 and τ_p = 10–20 ps) suggests that higher burst energy may result in increased cutting speed. This would require

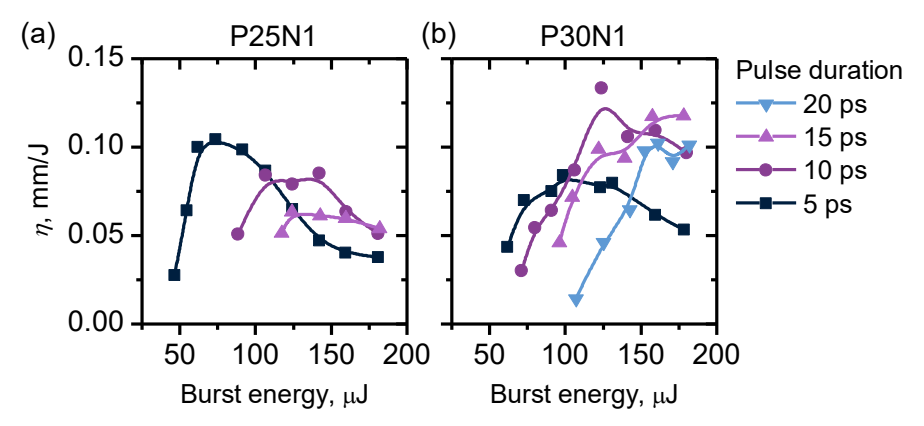


Figure 19. Linear cutting efficiency of 4.8 mm-thick glass. The dependence on burst energy P25N1 (a) and P30N1 (b) burst regimes using different pulse durations. The lines are added to guide the eye [A3].

a higher average power laser if the same burst repetition is maintained. Higher average power laser could also be used in an alternative way – by increasing the burst repetition rate at the parameter set with the highest cutting efficiency. However, in this case, faster galvanoscanners might be needed, as this method would increase the scanning speed if the same pitch is maintained. A higher number of pulses per burst might also result in increased cutting speed, as our results show that the P30N1 mode allows for reaching higher cutting speeds compared to the P25N1 regime.

The sidewall surface topographies of samples cut with the P30N1 burst regime, and the sidewall roughness dependence on burst energy are shown in Figure 20. No clear surface roughness dependence on burst energy or pulse duration was observed for pulse durations below 20 ps. This might result from the optimization approach, as both the vertical speed and pitch were changed for different pulse duration and burst regime combinations. A clearer dependence might have been visible if only one parameter had been changed.

The P30N1 regime with 20 ps stands out as higher R_a values were reached by increasing the burst energy from 140 μ J to 180 μ J (Figure 20(b)). The topographies of the sidewall surfaces indicate horizontal ridges formed for these parameter sets. The regime also differed from others as the optimal pitch was 20 μ m, which is considerably lower than that of other regimes at the same burst energies (Figure 16(b)). The relatively low pitch means that more spiral windings will be scanned at a low speed in the transverse plane per single layer. Considering that a similar cutting speed is achieved for 10–20 ps at 140–180 μ J (Figure 17(b)), the vertical distance between the layers should be larger

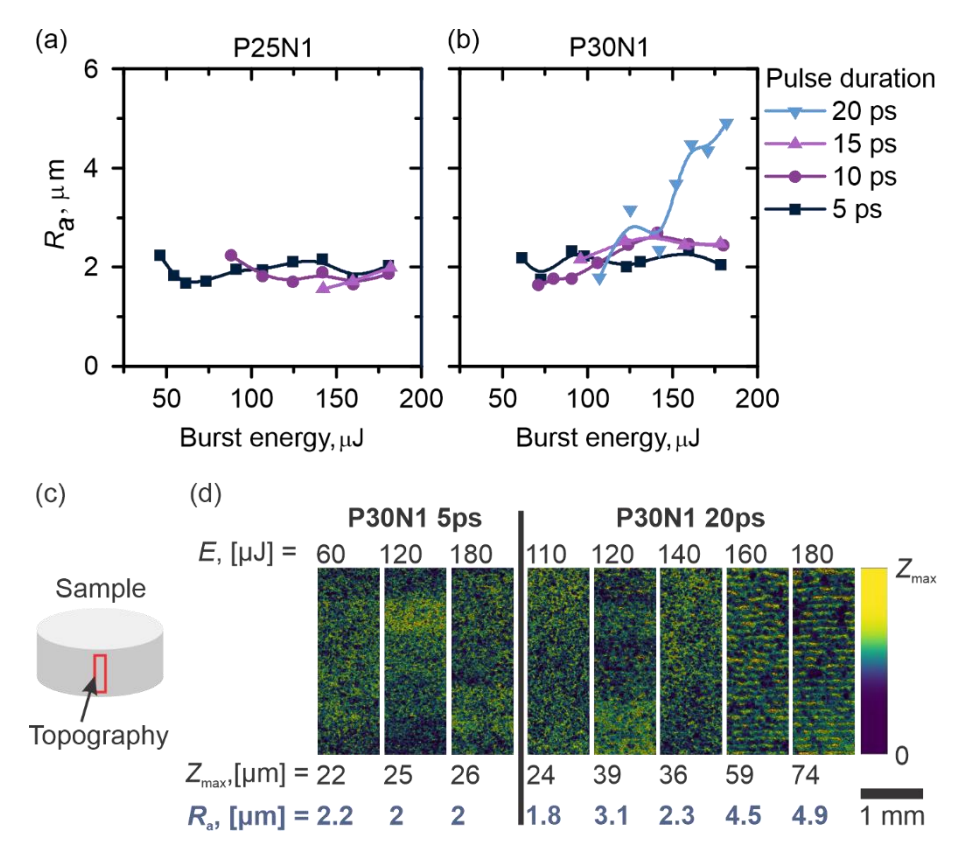


Figure 20. Sample sidewall surface roughness dependence on burst energy when using different pulse duration (5–20 ps) and burst regimes (P25N1 (a), P30N1 (b)), the measurement scheme for sidewall surface topography (c), and sidewall topographies for samples cut with P30N1 burst regime, 5 and 20 ps pulse duration and various burst energies [A3].

for a lower-pitch regime. As the inner circle scanning repeats at higher distances in the Z direction, the scanning lines become visible, resulting in higher surface roughness.

The average sidewall roughness R_a of all the samples was 2.3 μ m with a standard deviation of 0.9 μ m. This is comparable to the sidewall roughness of 3.2 μ m (R_a) of SLG samples cut with nanosecond pulses [5].

Edge quality was assessed by measuring the largest chipping on both the front and bottom surfaces of the sample (as shown in Figure 21(a)). No clear dependence on different burst regimes was detected. However, a higher number of samples should be taken into account as the formation of cracks is a stochastic phenomenon. Figure 21(b) presents the average maximum

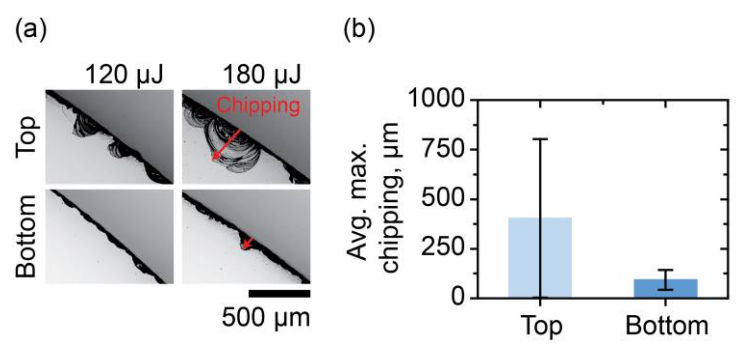


Figure 21. Edge chipping evaluation. OM pictures of the top and bottom surfaces of the sample cut with P30N1 burst regime using 15 ps pulse duration and different burst energy (a). The measured chippings are indicated with red arrows. Maximum chipping on the top and bottom surfaces, averaged across samples processed using the optimal parameter sets (b) [A3].

chipping measured across all samples for both the top and bottom surfaces. On average, the top surface exhibited chippings 4.4 times larger than the bottom surface, with values of 400 μ m ($\sigma_{stdev} = 400 \mu$ m) for the top and 90 μ m ($\sigma_{stdev} = 50 \mu$ m) for the bottom. The chipping lengths for the rear surface are similar to those observed in a study conducted with nanosecond pulses [31].

The reason for the larger crack formation on the top surface is an intrinsic property of the cutting process itself. The cutting starts with the focal spot being raised towards the front surface. As the cutting process progresses, the beam spot on the front surface decreases, and the energy fluence increases. When the beam waist comes close to the front surface, the laser fluence can exceed the damage threshold, causing the front surface ablation [209–211]. The same problem was encountered by Dudutis *et al.*, where the front surface ablation and the shattering of a thin glass layer were proposed to be responsible for the formation of large cracks [5]. The chipping size should be reduced by using a higher NA, as this would allow the beam waist to be positioned closer to the front surface before damaging it.

3.2. Cutting with variable parameters

High-throughput cutting compromises quality, posing a major challenge for its industrial applications. The sample strength is reduced by surface chippings and cracks [110]. Furthermore, the concentration of stress at the edges makes samples with sidewalls perpendicular to the front or bottom surfaces more prone to cracking and chipping upon impact [133]. However, additional processing could improve the quality of the samples. Surface chippings can

be eliminated by forming chamfers that are wider than the chippings themselves. However, the process parameters for chamfer formation must be optimized to ensure high-quality results.

In this subsection, 32 mm diameter circles were cut from 2.3 mm-thick SLG samples. The high-throughput cutting parameters were slightly adjusted due to the system-imposed limitation of a 6 m/s beam scanning speed. The cutting was performed with $E_{\rm B}=170~\mu \rm J$, using 15 ps pulses, 200 kHz burst repetition rate, and P40N2 BiBurst regime. The cutting kerf was reduced to 120 μm , the distance between the subsequent shots was 20 μm , and the distance between the subsequent scanning lines was 40 μm . The vertical speed was reduced to enhance the quality of the surfaces. The cutting took 12 seconds, corresponding to an 8.4 mm/s cutting speed and a 0.25 mm/J linear cutting efficiency. The cutting process was repeated ten times, with chipping widths remaining below 300 μm for eight out of the ten samples. Therefore, it was decided to form chamfers with an angle of 45 deg and dimensions of 300 μm in both width and depth (Figure 5). The chamfer formation method is more thoroughly described in Sub-subsubsection 2.2.1.1.

To achieve high quality, the chamfers were formed using either a singlepulse (P1N1) or a BiBurst regime that consisted of a low number of pulses. The chamfers were intended to be formed using full laser power to minimize the processing time. However, high burst energy results in low quality. Therefore, the full power of the laser was exploited by increasing the burst repetition rate to 600 kHz and reducing the burst energy to 57 µJ. Both chamfers were formed using 15 ps pulse duration. The bottom chamfer was formed with the P2N2 BiBurst regime using 10 µm and 15 µm distances between the subsequent shots and lines, respectively. The bottom chamfer was formed with a BiBurst regime to reduce the peak power and mitigate selffocusing effects. The single-pulse regime was employed for the top chamfer, using 5 µm and 10 µm distances between the subsequent shots and lines, respectively. The bottom and top chamfers were formed in 12 s and 10 s, respectively. Therefore, the cutting of a sample and the formation of chamfers took 34 seconds. The effective cutting speed and efficiency of the full process (excluding the time required for parameter adjustments) were 3 mm/s and 0.09 mm/J. The throughput of the distinct part formation can be calculated by dividing the ablated volume by the processing time. The cutting throughput (2.3 mm³/s) was 3-5 times higher compared to the formation of the bottom $(0.7 \text{ mm}^3/\text{s})$ and top $(0.4 \text{ mm}^3/\text{s})$ chamfers.

Figure 22(a) shows the topography of a side of a chamfered sample, while the OM images of the top and bottom surfaces of chamfered and

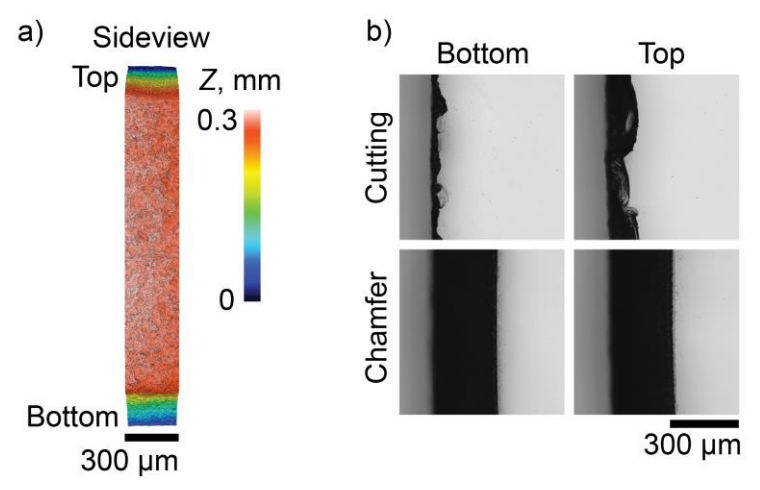


Figure 22. Topography of a sample side (a) and OM images of the bottom and top surfaces of samples with and without chamfers (b).

unchamfered samples are given in Figure 22(b). The images demonstrate that forming 300 μ m-length chamfers removes the edge chippings produced during the initial cutting process. Therefore, we have applied high-throughput and high-quality processing for the same workpiece using the same laser system. This highlights the potential of applying a burst-mode laser source in the glass processing industry.

3.3. Applications

The optimal parameter sets for BUC were used to cut complex shapes (Figure 23(a–c)), 18.8 mm-thick samples (Figure 23(d)), and oblique cylinders (Figure 23(f)). The slant angles, defined as the tilt of the oblique cylinders from the surface normal (depicted in Figure 23(e, g)), reached up to 35 degrees. The slanted sample was cut by translating the cutting zone by Δx at different Z positions while the beam angle of incidence remained unchanged (Figure 23(e)). We note that the sidewall roughness increased with the slant angle (Figure 23(g, h)), reaching 5.7 μ m (R_a) at 35 degrees.

The cutting speed for all samples shown in Figure 23 was lower than the 4.2 mm/s achieved in Subsection 3.1. The cutting speeds were 0.01 mm/s for Figure 10(a), 0.08 mm/s for Figure 10(d), and 0.48 mm/s for Figure 10(f). The reduced cutting speeds emerged from several factors. First, the cutting widths had to be enlarged for thick and slanted samples to facilitate the removal of ablated particles. Second, the burst repetition rates were reduced for samples

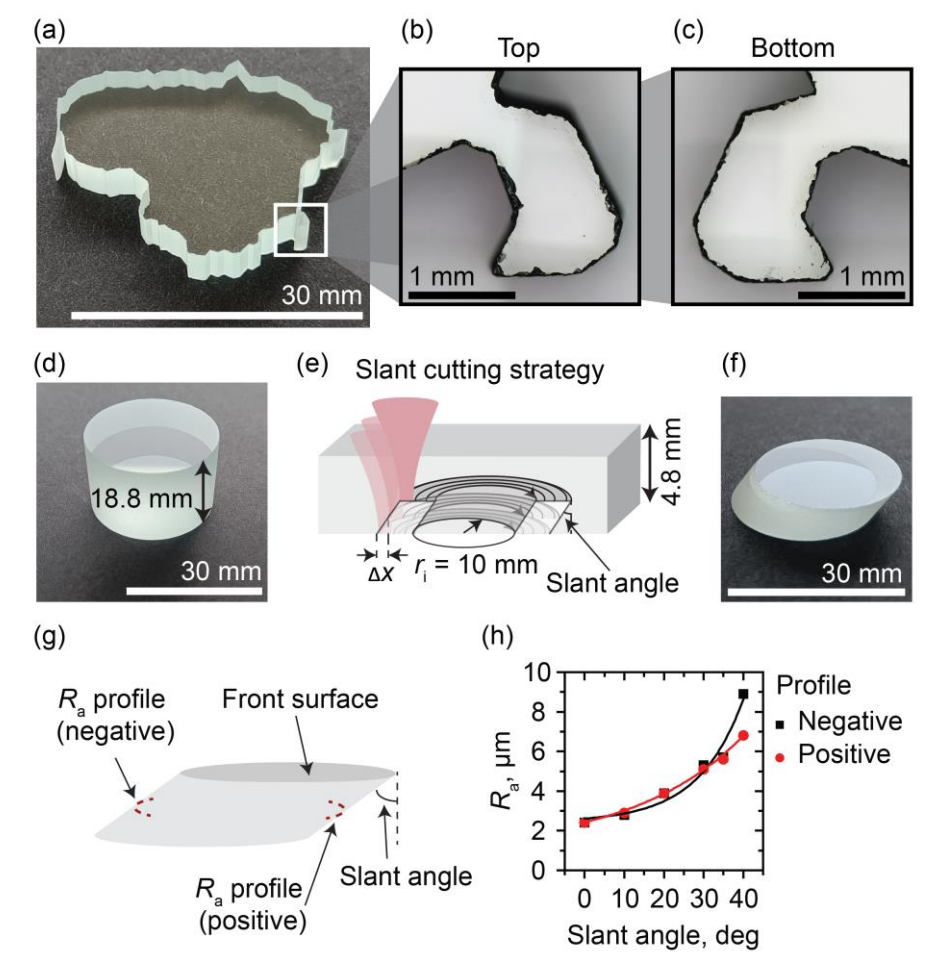


Figure 23. Complex samples cut with a bottom-up technique using a burst regime. Lithuanian borders cut from 4.8 mm-thick glass (a) with the top (b) and bottom (c) surfaces inspected with an OM. The straight wall 15 mm radius cylinder (d). The slant sample cutting strategy (e), the oblique cylinder with a slant angle of 35 degrees (f), the slant object R_a measurement scheme (g), and sample sidewall roughness R_a dependence on slant angle for positive and negative profiles (h). The data points given in the (h) part are fitted with the exponential function $(A \exp[Bx] + C)$, where x is the slant angle) for eye guidance [A3].

shown in Figure 23(a, d). For a thick sample, it helped to reduce heat accumulation, and for a complex trajectory cut, it reduced the beam scanning speed to suit the limitations of galvanometer scanners. Finally, the cutting speed for the thick sample is lower due to its thickness and diameter of 30 mm.

3.4. Subtractive laser glass cutting overview

This subsection will focus exclusively on comparing subtractive laser glass cutting methods of TDC, WATDC, and BUC, as these are single-step processes capable of cutting complex contours. The cutting speed is calculated by dividing the cutting length by the processing time [110] or by dividing the scanning speed by the number of scanning lines [5,144,158–160,168]. In the latter case, the time spent on jumps between the scanning lines is not considered. Straight [5,141,144,158–160,168], circular [158], and rectangular [5,110] cutting trajectories are demonstrated in different studies.

The comparison of linear cutting efficiency and speed achieved in various studies can only be applied to the samples of the same thickness, as they are directly proportional to it. Therefore, 1 mm-thick glass was additionally cut using a 225 μ m cutting kerf employing the P30N1 burst regime with 15 ps pulses and a burst energy of 170 μ J.

The cutting speed and linear cutting efficiency of different subtractive laser cutting techniques for 1 mm-thick glass samples are shown in Figure 24. Both parameters indicate that BUC technology is superior to other methods by more than an order of magnitude. In this work, we demonstrated 13 and 110 times higher cutting speed, and 21 and 64 times higher cutting efficiency compared to the WATDC and TDC, respectively.

This work has demonstrated a similar linear cutting efficiency (0.64 mm/J) as BUC using nanosecond pulses and 532 nm wavelength (532 nm ns-BUC),

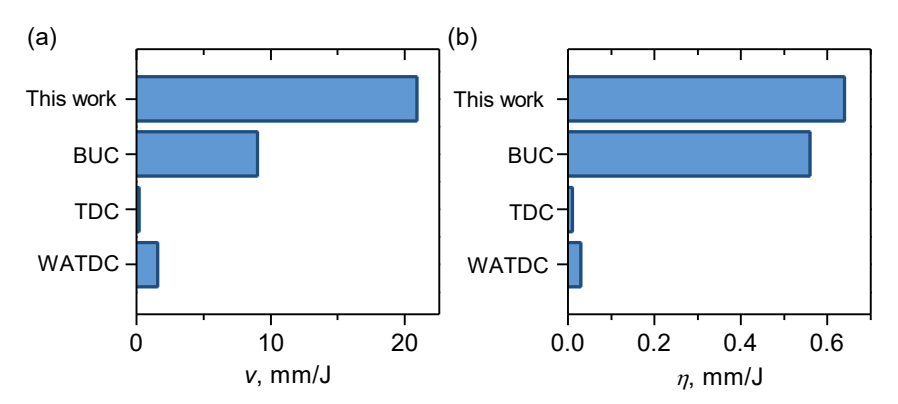


Figure 24. Comparison of fully cut-through 1 mm-thick glass cutting. Cutting speed (a) and linear cutting efficiency (b) using different subtractive laser glass cutting techniques (BUC – bottom-up cutting [110], TDC – top-down cutting [5], WATDC – water-assisted top-down cutting [141,158]). "This work" refers to sample processing using BUC at 1030 nm, with the P30N1 burst regime, 15 ps pulses, and 170 μJ burst energy [A3].

which results in a cutting efficiency of 0.56 mm/J. However, the achieved cutting speed of 20.9 mm/s in this study was about twice as high due to the use of higher average power. This also highlights the possibility of exploiting the full power of the laser source when working with the fundamental wavelength, while conversion to harmonics results in a loss of power.

A comparison of subtractive laser cutting methods is shown in Table 5. This work demonstrated comparable relative cutting speeds and efficiencies for both 4.8 and 1 mm thick samples. However, the cutting speed typically does not depend linearly on glass thickness. Therefore, higher cutting speed and efficiency could be obtained for thinner glass by reducing the cutting width. Furthermore, the cutting speed and efficiency of the top-down

Table 5. Comparison of subtractive laser glass cutting methods. This study employed a GHz burst regime, whereas other studies utilized single-pulse regimes. Here, h denotes sample thickness, λ – wavelength, $\tau_{\rm p}$ – pulse (*intra-burst pulse) duration, $P_{\rm ave}$ – average power, v – cutting speed, $v_{\rm rel}$ – relative cutting speed, η – linear cutting efficiency, $\eta_{\rm rel}$ – relative cutting efficiency, $R_{\rm a}$ – sidewall surface roughness, $d_{\rm front}$ – front and $d_{\rm bot}$ – bottom surface damage width.

Material	<i>h</i> , mm	λ, nm	$^{ m d}_{2}$	$P_{\rm ave}$, W	v, mm/s	$ u_{\mathrm{rel}}, $ $ u_{\mathrm{rel}}^{2/s} $	η , mm/J	$\eta_{ m rel},$ mm $^2/{ m J}$	$R_{ m a}$, $\mu{ m m}$	$d_{ m front}$, $\mu{ m m}$	$d_{ m bot}$, $\mu{ m m}$	Source
Bottom-up cutting (BUC)												
SLG	4.8	1030	15 ps*	36	4.2	20.2	0.12	0.58	2.4	330	110	This
												work
SLG	4.8	1030	10 ps*	24.8	3.3	15.8	0.13	0.64	2.4	120	80	This
												work
SLG	1	1030	15 ps*	33	20.9	20.9	0.64	0.64	2.6	200	160	This
												work
SLG	1	532	12.5 ns	16	9	9	0.56	0.56	1.4	140	125	[110]
SLG	1	1064	12.5 ns	26	0.9	0.9	0.03	0.03	3.2	79	76	[5]
SLG	1	1064	10 ps	19.6	0.74	0.74	0.04	0.04	1	89	101	[5]
				T	op-dow	n cuttin	g (TDC	C)				
SLG	1	1064	10 ps	19.2	0.19	0.19	0.01	0.01	0.3	85	75	[5]
SLG	0.5	532	10 ps	2.3	0.04	0.02	0.02	0.01	-	-	-	[159]
BS	0.42	1064	13 ps	16.5	0.52	0.22	0.03	0.01	1.5	7.4	-	[160]
BS	0.3	1030	350 fs	20.8	3.2	0.96	0.15	0.05	1.7	16	30	[144]
BS	0.11	1030	350 fs	21	20.8	2.3	1	0.11	0.5	16	30	[144]
			Wa	ter-assi	sted top	-down	cutting	(WATD	C)			
SLG	1	1064	10 ps	144	1.58	1.58	0.01	0.01	1	-	-	[158]
SLG	1	1026	260 fs	10	0.33	0.33	0.03	0.03	-	-	-	[141]
SLG	1	1064	10 ps	30.6	0.34	0.34	0.01	0.01	0.8	128	124	[5]
BS	0.55	1030	350 fs	19.3	1.8	1	0.09	0.05	1.2	14	25	[144]
SLG	0.5	532	10 ps	2.3	0.3	0.15	0.13	0.07	-	-	-	[159]
BS	0.42	1064	13 ps	42	5	2.1	0.12	0.05	1.3	2.3	-	[160]
BS	0.4	355	10 ps	15.5	1.8	0.72	0.12	0.05	0.8	1.5	20	[168]
BS	0.3	1030	350 fs	19.3	4	1.2	0.21	0.06	0.7	14	25	[144]
BS	0.11	1030	350 fs	19.5	20.4	2.2	1	0.12	0.5	14	25	[144]

techniques would be even lower if scaled up to a larger thickness.

By comparing the results achieved with $\approx 1~\mu m$ wavelength, the relative cutting speed reported in this study exceeds that of others by 8 to 134 times, while the relative cutting efficiency is 3.2–64 times higher. However, 532 nm ns-BUC is a much more competitive method. Still, the relative cutting efficiency reported in this study is slightly higher, while the relative cutting speed is about twice as high as that of 532 nm ns-BUC.

The 532 nm ns-BUC led to the highest relative cutting speed for singlepulse regimes. Shorter wavelengths result in a higher nonlinear absorption, while nanosecond pulses induce a larger thermal load to the sample. High thermal stresses lead to the fracturing of a material, which is more efficient than ablation [5,162]. This work shows that high cutting speeds can also be achieved with picosecond pulses in GHz burst mode. SLG has a low thermal diffusivity (0.5 mm²/s [44]), leading to µs-scale thermal relaxation time for ~µm lengths of interest. As the duration between the intra-burst pulses is short (404 ps), subsequent pulses increase the thermal load, which leads to the material being cracked. In addition, higher peak intensity of picosecond pulses leads to an increased nonlinear absorption. The pulse peak intensity is increased a thousand times when comparing picoseconds to nanoseconds. On the contrary, the pulse division into a burst reduces the peak intensities of single pulses only by the number of intra-burst pulses. Therefore, GHz burst mode with picosecond pulses takes advantage of higher absorption, along with a higher thermal load. This results in a significant increase in cutting speed.

While fracturing a material increases the cutting throughput, it is also associated with a reduction in the quality of the produced samples. The BUC results in the highest sidewall surface roughness R_a of 1–3.2 μ m and the largest chippings of 76–330 μ m. Better quality is achieved with the TDC and WATDC methods, as the R_a ranges between 0.3–1.7 μ m and the chippings between 1.5–128 μ m.

3.5. Summary

We demonstrated the rapid and efficient cutting of 4.8 mm-thick SLG samples by employing GHz bursts with picosecond pulses. To achieve the highest cutting speed, the pulse duration must be chosen in consideration of the maximum laser burst energy. For higher burst energy, larger pitch, more pulses per burst, and longer pulse duration are favorable. For 4.8 mm-thick glass, the highest cutting speed of 4.2 mm/s and linear cutting efficiency of 0.64 mm/J were achieved using picosecond pulses in GHz bursts with an optimized pitch. The average maximum chippings for the investigated

processing parameters were 90 μ m and 400 μ m for the bottom and top surfaces, respectively. The average sidewall roughness (R_a) was 2.3 μ m.

Our results were compared to other laser subtractive cutting methods (TDC, WATDC, and BUC). The cutting speed (20.9 mm/s) and efficiency (0.64 mm/J) for 1 mm-thick glass were more than an order of magnitude higher for BUC compared to the TDC and WATDC. Specifically, the cutting speed was 110 and 13 times higher than the TDC and WATDC, respectively, while the cutting efficiency was 64 and 21 times greater, respectively. A similar cutting efficiency was achieved with 1030 nm GHz bursts with picosecond pulses, as with 532 nm nanosecond pulses, due to material removal via fracturing. This highlights the possibility of exploiting the full power of the laser source when working with the fundamental wavelength, as conversion to harmonics results in a loss of power. By comparing the results achieved with $\approx 1~\mu m$ wavelength, the relative cutting speed reported in this study exceeds that of others by 8 to 134 times, while the relative cutting efficiency is 3.2–64 times higher.

The BUC was applied to samples with various thicknesses, ranging from 1 to 18.8 mm. Additionally, the complex contours of the Lithuanian borders were cut from 4.8 mm-thick glass. This required a decrease in the beam scanning speed to suit the limitations of galvanometer scanners. Finally, oblique cylinders were cut by translating the cutting zone by Δx at different Z positions while the beam angle of incidence remained unchanged. The slant angles up to 35 degrees were achieved. The sidewall surface roughness increased with the slant angle, reaching 5.7 μ m at a 35-degree angle.

Overall, the GHz burst laser can significantly increase the cutting throughput compared to the classical ultrashort pulsed laser ablation. However, a high-speed cutting regime comes with an inferior cutting quality. Nevertheless, modern laser control enables a quick switch to more conventional laser processing parameters for high-quality ablation. Using a high-throughput regime, we demonstrated the cutting of 32 mm diameter circles from 2.3 mm-thick samples. The chippings formed during the cutting process were eliminated by forming 300 µm-long chamfers under high-quality regimes. The cutting throughput (2.3 mm³/s) was 3–5 times higher compared to the formation of the bottom (0.7 mm³/s) and top (0.4 mm³/s) chamfers. Applying high-quality ablation and high-speed coarse machining to the same workpiece opens new possibilities for laser micromachining of glass components.

4. SINGLE-SHOT MODIFICATIONS

In this section, the burst and BiBurst modes are used to form elongated single-shot modifications with transverse dimensions via self-focusing when using NA of \sim 0.04. The volumetric modifications are formed in FS and SLG samples.

The experimental setup is shown in Figure 7, while the single-shot modification formation scheme and characterization of the modifications are described in Sub-subsections 2.2.2 and 2.3.3, respectively. Results provided in this section were published in [A2] research paper.

4.1. Longitudinal modifications

No modification was observed in the volume of the samples using the single-pulse (P1N1) regime. The peak powers reached 0.7 GW for FS and up to 1.9 GW for SLG. This was 143 and 2375 times larger than the critical power for self-focusing in FS ($P_{cr} = 4.9 \text{ MW}$) and SLG ($P_{cr} = 0.8 \text{ MW}$), respectively. The P_{cr} values were calculated using equation (12) and the nonlinear refractive indexes listed in Table 1.

The highest tested peak powers were insufficient for producing filamentation in air ($P_{\rm cr} = 5.3$ GW [212]). This implies that filaments were created inside the glasses, but the free electron density was lower than the critical plasma density of ~ 10^{21} cm⁻³ [13]. This is the case for weak focusing, when less dense electron plasma is needed to counteract the self-focusing and diffraction, and the laser intensity is clamped to a level insufficient to induce damage [72,74,78].

The elongated in-volume modifications were formed by switching the laser regime from a single-pulse to the burst or BiBurst modes. For FS, MHz or GHz burst regimes consisting of at least 5 and 4 pulses, respectively, and for SLG, BiBurst regimes consisting of at least 20 pulses were needed to form modifications. A sequence of laser pulses separated at a short time can lead to the accumulation of self-trapped excitons [91], point defects [22], and heat [74,138]. These phenomena help to increase the deposited energy density, leading to permanent modifications [138].

The following chapters study longitudinal and transverse modifications formed in FS and SLG samples using the burst or BiBurst regimes.

4.1.1. Longitudinal length

The OM pictures of the longitudinal modifications taken from the side surface of the FS samples are shown in Figure 25. The uniformity of the longitudinal modifications was mostly determined by the number of intra-burst pulses and the temporal delay between them. Uniform longitudinal modifications in FS were only formed with GHz bursts of 8 or more intra-burst pulses. Modifications formed with MHz bursts and 5 pulses per GHz burst were split along the beam propagation axis (Figure 25(a, c, d)). The exception is the relatively short modifications (< 300 μ m) formed with either low burst energy or a low number of pulses per MHz burst.

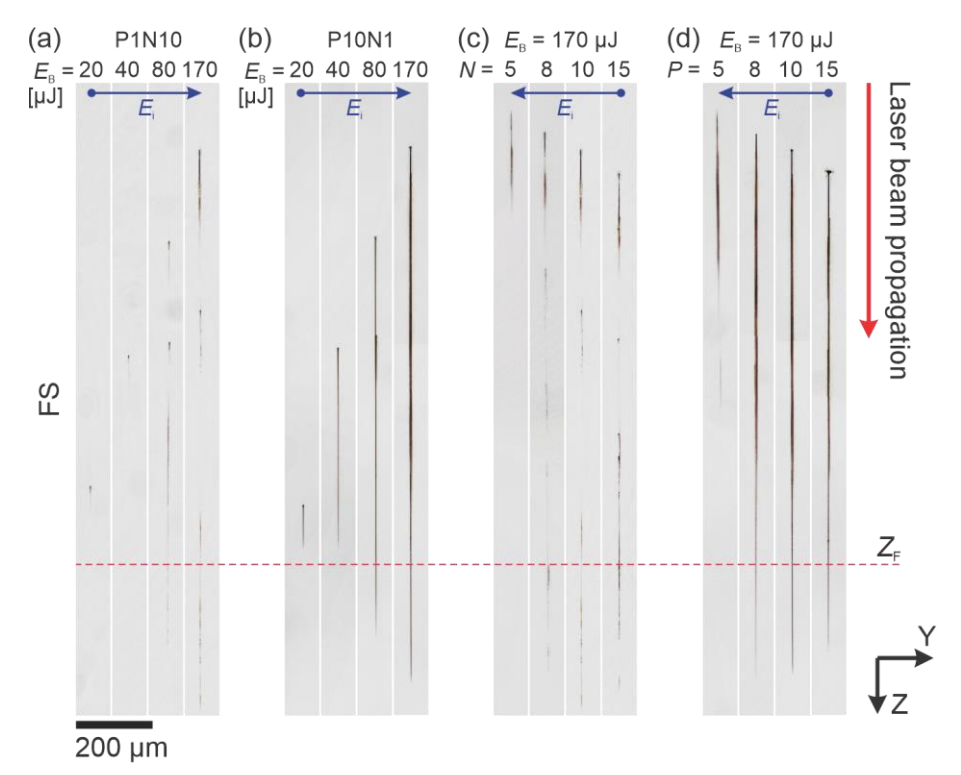


Figure 25. The OM images of longitudinal modifications in the YZ plane. The laser beam was focused from the top. The geometrical focal position Z_F , defined by linear optics, is represented by a red dashed line. The blue arrow represents the direction in which intra-burst energy (E_i) increases. The modifications formed in FS with 10 pulses per MHz and GHz burst at burst energies of 20–170 μ J are shown in parts (a) and (b), respectively. The modifications formed using the maximum burst energy of 170 μ J and 5–15 pulses per MHz and GHz burst are shown in parts (c) and (d), respectively [A2].

The filamentation separation along the propagation direction is a well-known phenomenon for a single-pulse regime [74,126,213]. The leading edge of the pulse creates an electron plasma, inducing a local reduction in the refractive index, which defocuses and splits the trailing edge of the pulse [213]. The leading edge of the pulse creates the first focus in the filament. The second peak in the plasma filament is formed when the trailing edge of the pulse has enough power to re-induce self-focusing.

The OM images of longitudinal modifications formed with $E_{\rm B}=170~\mu{\rm J}$ and 10 pulses per GHz and MHz bursts are shown in Figure 26. The modifications formed with GHz bursts are highly repeatable, as all modifications are uniform with close to equal lengths and positions (Figure 26(b)). All of the modifications formed using MHz bursts were divided into 3 parts. The position of the first part (closest to the front surface)

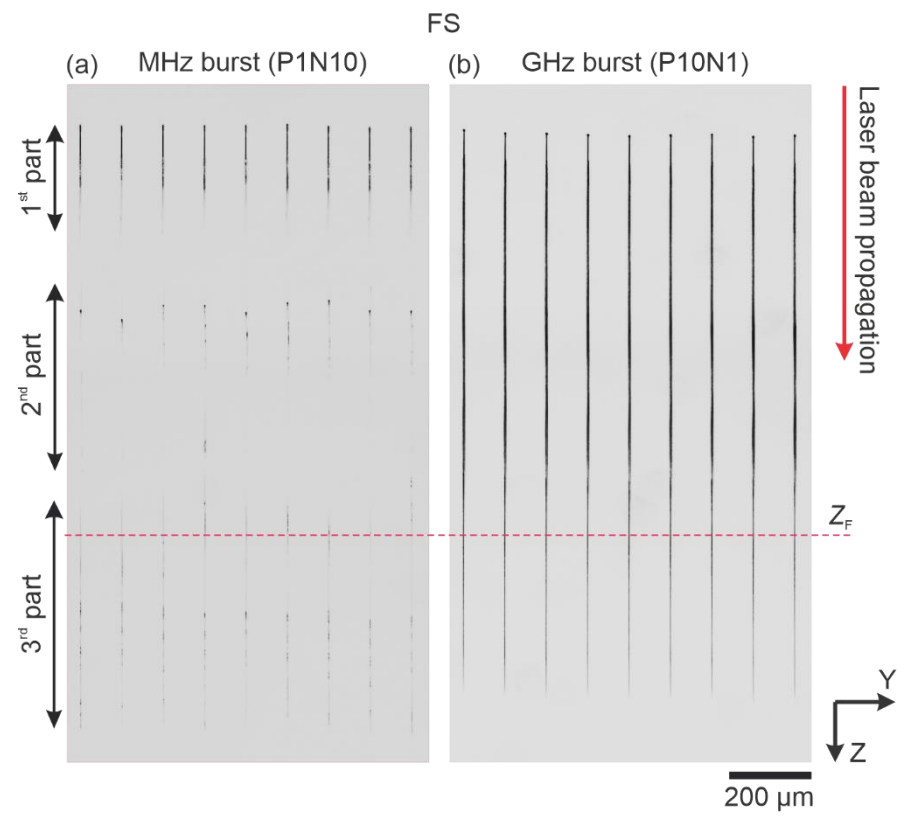


Figure 26. The reproducibility of the longitudinal modifications. OM images of longitudinal modifications formed in FS with 10 pulses per MHz (a) and GHz (b) bursts using 170 μ J burst energy. The geometrical focal position Z_F , defined by linear optics, is represented by a red dashed line [A2].

remained relatively consistent. However, the position and homogeneity of the 2nd and 3rd parts slightly differ. Therefore, the damage created by the first cycle of self-focusing is more repeatable and predictable than the damage formed by the further refocusing cycles.

The longitudinal length dependence on the number of pulses per burst or BiBurst for different energies is shown in Figure 27. MHz and GHz bursts consisting of 1–20 pulses were used to form modifications in the FS samples. In experiments with the SLG, the laser source enabled burst regimes with the number of pulses per burst limited to 10. However, no modification was observed in SLG using up to 10 pulses per MHz or GHz bursts. In order to increase the number of intra-burst pulses, BiBurst regimes of P10N(1–10) were introduced (Figure 27(c)). The BiBurst regimes with the highest number of 10 pulses per GHz burst were selected, as GHz bursts were more advantageous than MHz when forming longitudinal modifications in FS (Figure 25).

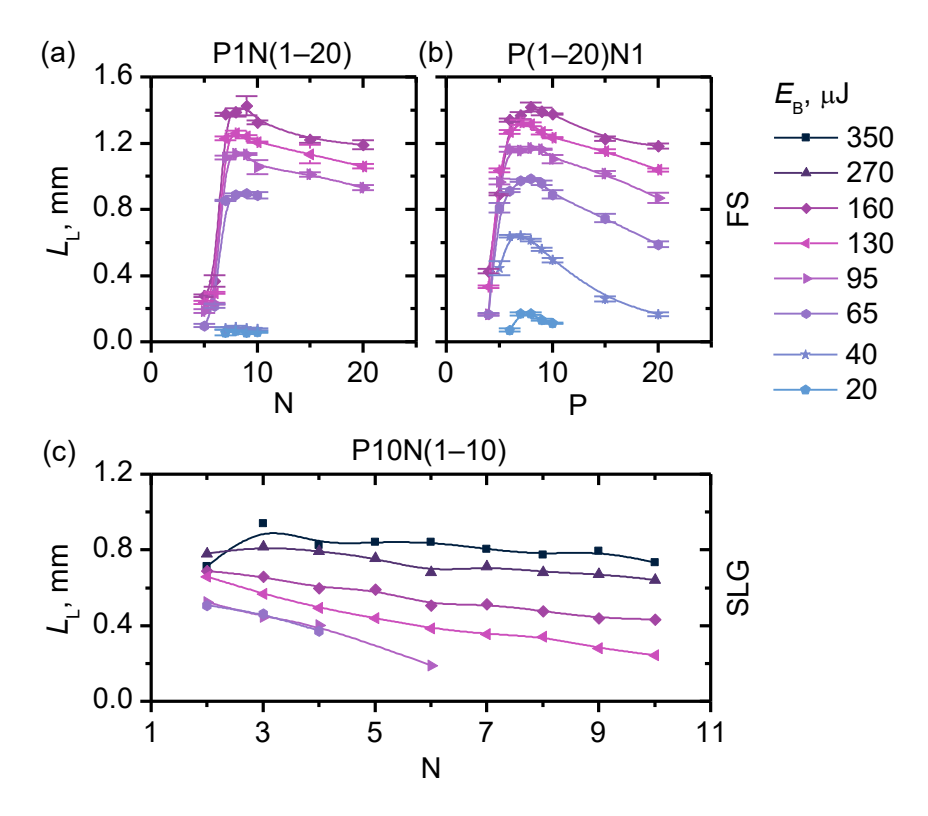


Figure 27. Longitudinal length dependence on pulses per MHz (a) and GHz (b) burst for FS and on pulses per MHz burst for SLG (c) when using different burst energies [A2].

As different burst modes were used for FS and SLG, a direct comparison of the results in different materials is not eligible. However, it is seen that higher burst energy resulted in longer longitudinal modifications for both the SLG and FS samples (Figure 27).

The modifications in FS were formed with 7–10 pulses per MHz burst when using burst energies of 20–40 μ J. A larger range of 5–15 pulses per MHz burst was suitable for modification formation when using a higher burst energy of 160 μ J. The same tendency is observed in SLG samples, as higher burst energy increased the suitable range of pulses per BiBurst needed to form modifications. Furthermore, the results on FS indicate that this range is increased when using GHz bursts. Therefore, higher cumulative effects, achieved with shorter intra-burst temporal delay, and stronger nonlinear interaction between the beam and the sample, achieved with higher burst energy, allow using a wider range of pulses per burst for modification formation.

The longest modifications in FS were formed with 7–10 (MHz) and 6–10 (GHz) pulses per burst for the same burst energy. The highest burst energy resulted in ~1.4 mm longitudinal lengths for the aforementioned optimal number of intra-burst pulses. The optimal range of pulses per burst exists as this parameter changes both the intra-burst pulse energy and the number of cumulative cycles. A higher number of pulses per burst results in lower intra-burst pulse peak intensities and weaker nonlinear interaction. On the contrary, a smaller number of intra-burst pulses results in fewer cumulative cycles, which are crucial for modification formation.

For the SLG, the optimal number of pulses per BiBurst was not so pronounced. In most cases, lowering the number of pulses per MHz burst increased the modification lengths. However, for 270 and 350 μ J burst energies, the P10N2 regime resulted in shorter longitudinal modifications than the P10N3. This was due to increased intra-burst pulse energy, which caused damage to the front surface. This resulted in less energy available for modification formation since a portion was lost due to front surface damage and plasma shielding. Consequently, the longest modifications of ~0.9 mm were formed using the P10N3 BiBurst regime at the highest burst energy of 350 μ J, as these parameters provided the highest pulse peak intensities without inducing front surface damage.

It should be reminded that although the longitudinal lengths in FS were similar for MHz and GHz bursts, the modifications formed with GHz bursts were more uniform (as shown in Figure 25).

The influence of pulse duration on longitudinal lengths was tested for SLG samples using a BiBurst regime of P10N5 (Figure 28). Higher E_B and shorter

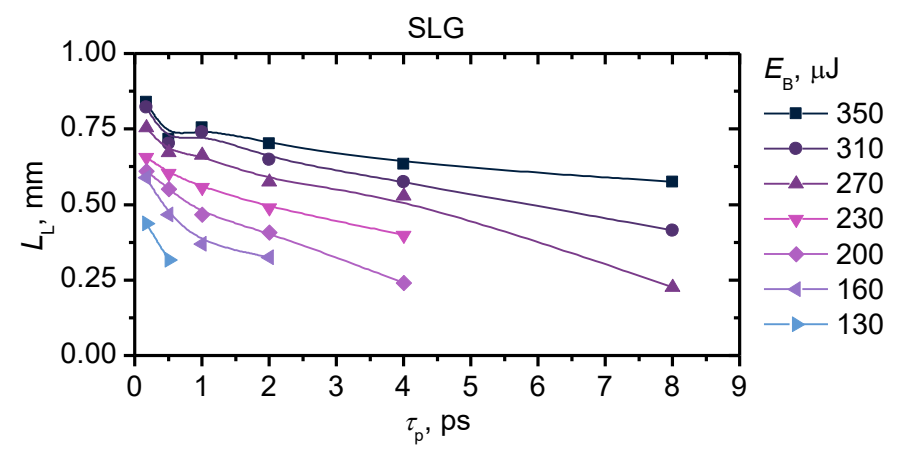


Figure 28. Longitudinal length dependence on pulse duration for modifications formed in SLG with BiBurst regime of P10N5 using different burst energies.

 $\tau_{\rm p}$ result in longer longitudinal modifications, with the longest being 840 µm, formed with $\tau_{\rm p} = 176$ fs and $E_{\rm B} = 350$ µJ. Shorter $\tau_{\rm p}$ and higher $E_{\rm B}$ both lead to higher pulse peak intensities and stronger nonlinear interaction between the sample and the beam, allowing the formation of longer modifications.

4.1.2. Modification position

The position of the longitudinal modifications formed in FS was characterized by measuring the distances between the top surface of the sample and the front $D_{\rm F}$ and bottom $D_{\rm B}$ of the modification. The dependence of $D_{\rm F}$ and $D_{\rm B}$ on burst energy is shown in Figure 29. All the inspected modifications started to form before the geometrical focus. The modifications formed closer to the front surface with higher burst energy and fewer intra-burst pulses. A stronger Kerr effect for higher pulse peak intensities could explain this. The intra-burst repetition rate had a minimal impact on the front position of modification, as there was no significant difference between the MHz and GHz burst regimes.

As the burst energy increased, the modifications expanded in both directions. The number of pulses per burst had a different impact on the $D_{\rm F}$ and $D_{\rm B}$ values. The modification bottom position varied slightly within the 8–15 pulses per burst range. However, when the number of pulses per burst changed from 5 to 8, the $D_{\rm B}$ increased by up to 1.2 mm (for MHz burst) and 0.7 mm (for GHz burst). The steep increase in the longitudinal lengths when increasing the number of pulses per burst from 5 to 8 was also seen in Figure 25(c, d)) and Figure 27(a, b).

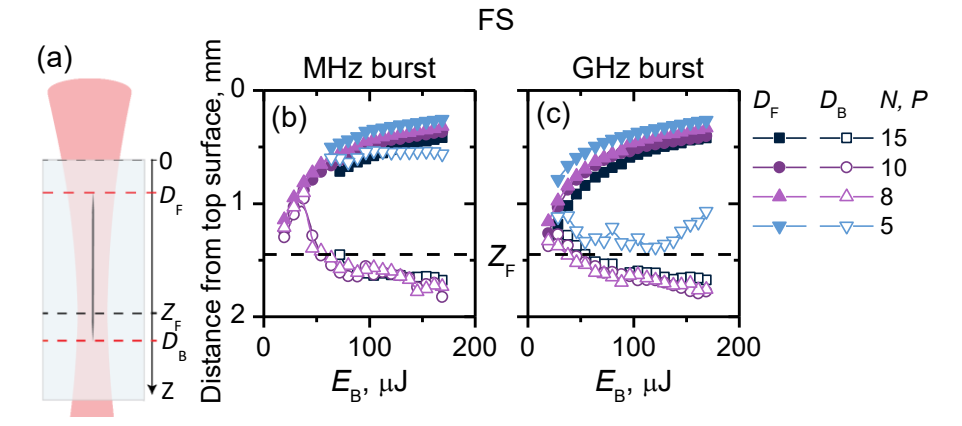


Figure 29. Scheme of the focused laser beam and different depth parameters (a). The red dashed lines represent the parameters in (b, c) graphs. Distance between the FS sample top surface to the modification front (D_F) and bottom (D_B) dependence on burst energy for 5–15 pulses per MHz and GHz burst is shown in (b) and (c) graphs, respectively. The data points are connected with lines for eye guidance. The black dashed line on (b, c) parts corresponds to the geometrical focus Z_F , defined by linear optics [A2].

The P5N1 regime exhibits an unusual behavior, as increasing the burst energy from 120 μ J resulted in a smaller D_B position. As the front position of the modification formed with the P5N1 regime exhibited the same tendency as other regimes, a more thorough analysis of the longitudinal lengths should be made.

The OM pictures of the longitudinal modifications formed in FS with the P5N1 regime and different burst energies are shown in Figure 30. The modifications are split into several parts for all the burst energies. The length of the first part increased with burst energy. However, from 140 µJ, the distance between the first and the second parts decreased with burst energy, resulting in a shorter overall length. The decrease in the spacing between the focusing-refocusing events for higher energies was also observed in other studies [214,215]. Furthermore, the focusing-refocusing cycles were shown to start merging at sufficient energies, resulting in a filament with a more homogeneous spatial intensity profile [215].

The filament front position can be calculated for a single-pulse regime for low-NA focusing conditions [216]. As we studied the burst regime, we calculated the position, assuming it is defined by a single intra-burst pulse.

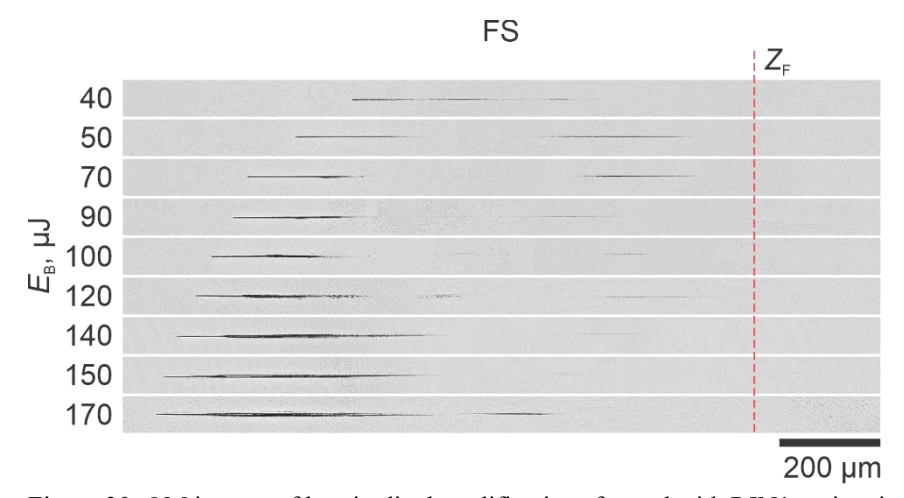


Figure 30. OM images of longitudinal modifications formed with P5N1 regime in FS with different burst energies. The contrast of the OM pictures was enhanced with computer software to improve clarity. The geometrical focal position Z_F , defined by linear optics, is represented by a red dashed line.

The intra-burst pulse energy E_i was calculated from the burst energy as:

$$E_i = \frac{E_B}{N_i + 2},\tag{27}$$

where N_i denotes the number of pulses per MHz or GHz burst. The number 2 in the denominator is added because the last pulse in a burst had ~3 times larger amplitude (seen in Figure 8(a, b)). The filament collapse distance is calculated with a lens equation using nonlinear $L_{\rm C}$ and geometrical $Z_{\rm f}$ focal lengths. The distance from the sample top to the modification front was calculated as:

$$D_{\rm F} = \frac{L_{\rm C} Z_{\rm f}}{L_{\rm C} + Z_{\rm f}}. (28)$$

The nonlinear focus was calculated with equation (13). The peak power of the initial beam was calculated as $P_{\rm in} = 0.94E_i/\tau_{\rm p}$. The radius of the beam w was taken, assuming that the nonlinear interaction started at the front surface of a FS sample. In the experiment, the beam waist position was mechanically shifted by 1 mm from the front surface to the volume of a sample. Therefore, the beam diameter at the front surface can be determined from the beam measurements in air, given in Figure 9(c). The beam diameter at the front

surface of a FS sample was taken as 57 μ m, the average of the diameters along the minor and major axes at a Z position of 1 mm before the waist. With the given parameters, the nonlinear focal length $L_{\rm C}$ was computed.

The dependence of the modification front position on the intra-burst pulse energy is shown in Figure 31(b, c), where symbols represent the experimental data points, and the green line depicts the position calculated using equation (28). The model fits the experimental data well, with errors of up to 10%, indicating that the modification front position can be accurately estimated using only the intra-burst pulse energy.

The number of intra-burst pulses and intra-burst rate had a negligible impact on the modification front position. Therefore, despite accumulative cycles being crucial for modification formation, they do not have a significant importance on the modification front position.

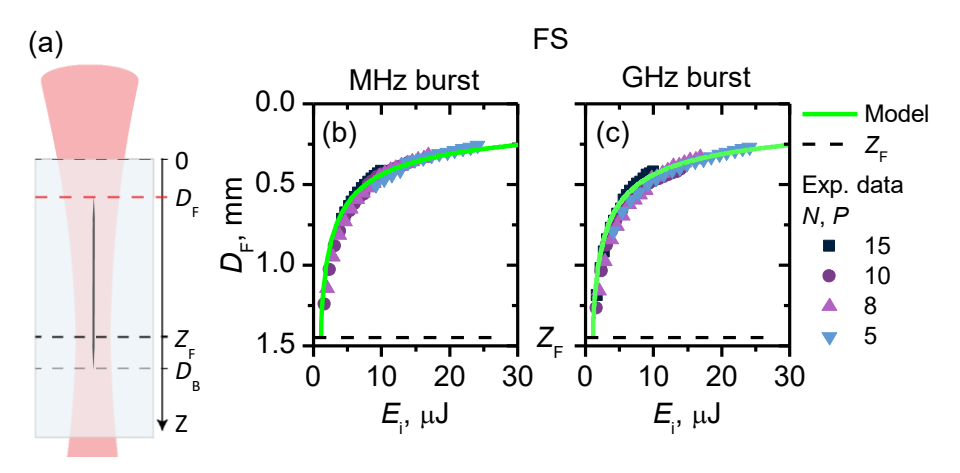


Figure 31. Schematic of the focused laser beam and different depth parameters (a). Distance between the FS sample top surface and modification front ($D_{\rm F}$) dependence on intra-burst energy when using MHz (b) and GHz (c) bursts. The dark dashed line corresponds to the geometrical focus, defined by linear optics, and the solid green line – to the position calculated with equation (28).

4.2. Transverse modifications

Self-focusing typically induces patterns of one or more circular damage regions that are elongated along the propagation axis [125,217]. However, the burst regime enabled the formation of modifications with elongated transverse dimensions. Hendricks *et al.* studied the MHz burst effect on cracks formed

in SLG using a high NA focusing system [178]. The time-resolved analysis revealed that each intra-burst pulse generates a shear acoustic wave, which induces tensile stresses that increase the length of a crack. As the stress redistribution occurs at around 9 μs [178], both MHz and GHz bursts should impact the crack length.

The following chapters are dedicated to studying the impact of different laser parameters on transverse modifications.

4.2.1. Polarization

The polarization impact on transverse modifications for burst regimes of P10N1, P1N10 (FS), and BiBurst regime of P10N5 (SLG) can be seen in the OM images shown in Figure 32. For FS samples, two different dependencies are seen. For $E_B = 170 \,\mu\text{J}$, the transverse modifications aligned close to the major axis of the beam before the geometrical focus (Figure 9(b)). This is similar to the modifications formed with Bessel beams, as crack control by beam asymmetry is a well-known phenomenon [89]. For lower burst energies, the transverse modifications aligned along the orientation of a linear polarization. For circular polarization, this corresponded to the omnidirectional cracks. It should be noted that higher burst energy was needed to form modifications using circular polarization due to a higher critical power for self-focusing [46] and a lower multiphoton ionization probability [218].

The transverse modifications formed in SLG aligned perpendicularly to the polarization. However, for the highest burst energies of 300 μ J, the transverse modifications shifted slightly towards the beam major axis for polarizations set along the X and Y axes. Nevertheless, the crack angle control by the major beam axis is not as pronounced as with FS samples. This could be related to the lower intra-burst pulse energy used in the SLG experiments due to the higher number of intra-burst pulses.

The polarization-related effects on material processing were discussed in Subsection 1.9. Rapp *et al.* demonstrated the impact of polarization on cracks formed in crystalline material with a Bessel beam. [196]. However, to our knowledge, this is the first time that the polarization effect on crack formation in glass has been reported.

When the polarization direction does not coincide with the direction of the major axis of the beam, the orientation of directional cracks formed in FS might be driven by the interplay between two competing phenomena. Cracks are pushed to orientate (i) along the polarization direction and (ii) along the major axis of the beam. The latter effect requires the asymmetrical intensity

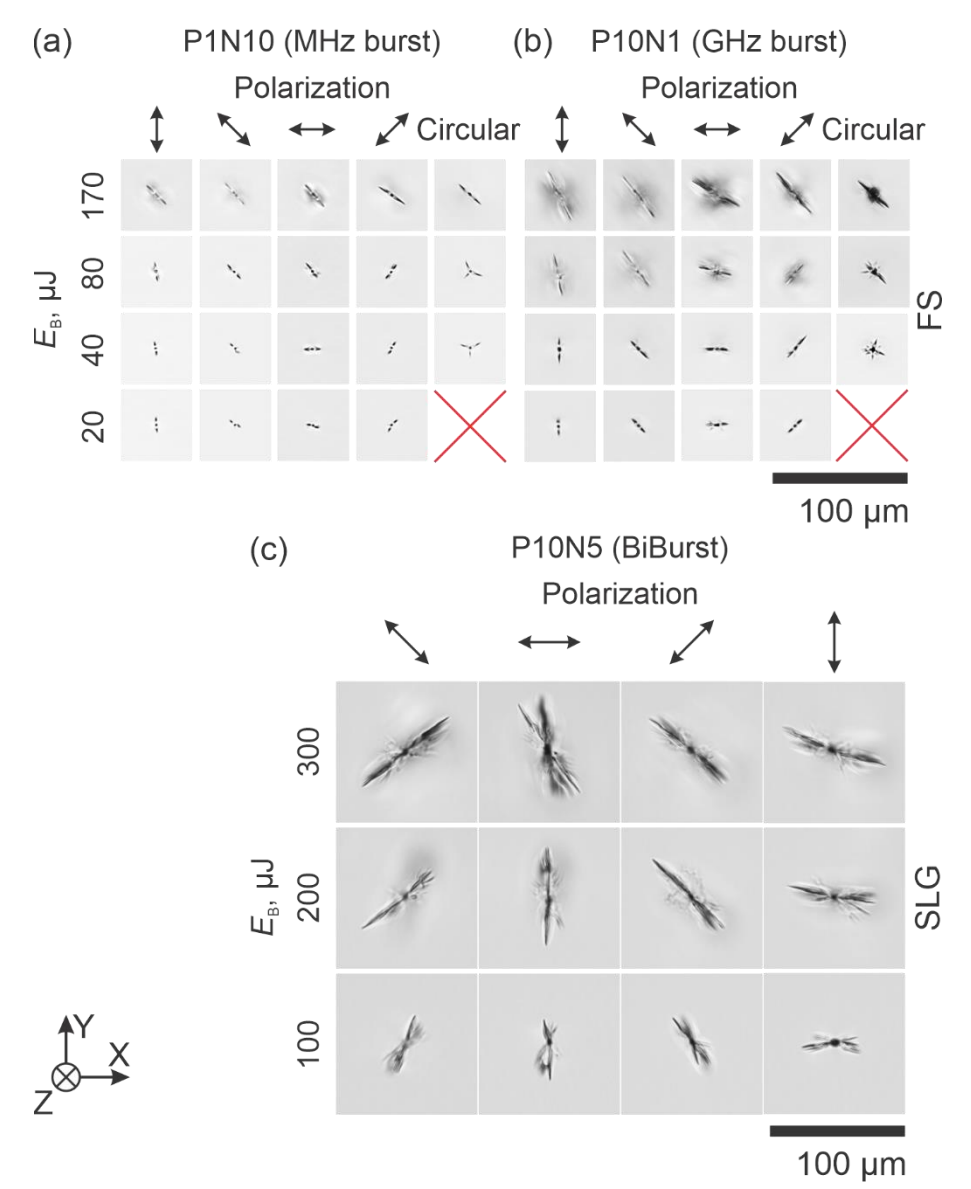


Figure 32. OM pictures of transverse modifications in the XY plane. The modifications were formed in FS (a, b) and SLG (c) with burst regimes of P1N10 (a), P10N1 (b), and BiBurst regime P10N5 (c) using different burst energies, angles of linear polarization, and circular polarization. The parameter sets at which no modifications were seen are depicted with red crosses [A1, A2].

distribution. In the linear propagation regime, the ellipticity of the beam changes along the beam propagation direction and is of a lower value at regions just before the geometrical focus (Figure 9(c)). At higher pulse energy, the nonlinear interaction between the laser pulse and material should

begin at longer distances before the geometrical focus, where the beam is more elliptical, and the asymmetry-driven control of crack orientation should dominate. For lower energies, the nonlinear interaction should begin with a more symmetrical beam, allowing the control by polarization to dominate.

The crack control via beam ellipticity and polarization could be related to the formation of deterministic MF patterns. Beam ellipticity of just 1.09 can induce a MF pattern with a central filament and a pair of identical filaments along the major and (or) minor axes of the ellipse [66]. However, the vectorial effects are also shown to cause the breakup of axial symmetry and beam splitting into two filaments along or perpendicular to the polarization [62,65]. Intensity patterns with central core and side lobes can also be seen in works with modulated Bessel-like beams formed using SLM [88], phase or amplitude masks [134], elliptically-shaped axicons [89], or tilting an axicon [219]. The cracks can orient along the major axis of the central core [89,134] or along the side lobes [88,131]. Therefore, the angle of the modifications formed in our work might have been determined by the secondary filaments created along the beam ellipticity, or parallel or perpendicular to polarization. Furthermore, Fibich et al. stated that the threshold for polarization-induced MF is considerably lower than that required for MF caused by beam astigmatism or noise [63,65]. This would explain the transverse angle dependence on polarization at lower burst energies and on the beam angle for higher burst energies. However, the exact evolution of the non-ideal beam during nonlinear propagation is unclear and requires a thorough theoretical investigation.

The dependence of the transverse angle of the modifications, formed in FS with P1N10 and P10N1 regimes, on burst energy for different polarization angles is shown in Figure 33(a, b). For higher burst energies, the modifications started to orient at a -45 deg angle, which coincided with the major axis of the beam before the geometrical focal point (Figure 9(b)). The modifications aligned along the polarization for burst energies up to 80 μ J (GHz) or 70 μ J (MHz). The polarization-controlled regimes are displayed in a gray rectangle in Figure 33.

The dependence of transverse length on burst energy for different polarization angles is shown in Figure 33(c, d). The transverse lengths increased with burst energy. In the polarization-controlled regime, the transverse lengths were ~12 μm for MHz and up to 32 μm for GHz bursts. Different polarization angles had a minimal impact on transverse lengths for MHz burst regimes. On the contrary, transverse lengths depended on the polarization angle for GHz bursts within the burst energy range of 60–140 μJ .

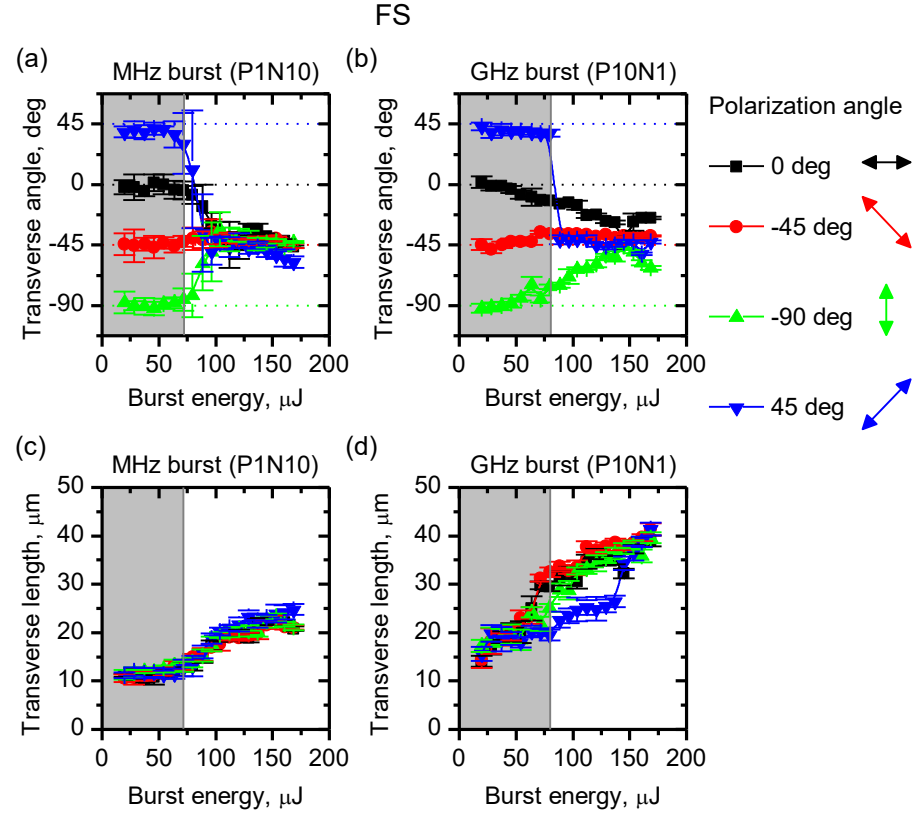


Figure 33. Modification transverse angle (a, b) and length (c, d) dependence on burst energy for different polarization angles of 45 deg, 0 deg, -45 deg, and -90 deg. The modifications were formed in FS using 10 pulses per MHz (a, c) and GHz (b, d) burst. The dashed horizontal lines in graphs (a, b) represent the polarization angles. The gray box represents the polarization-controlled regimes [A2].

At this burst energy range, the largest transverse lengths were achieved with the polarization set close to parallel to the major axis of the beam before the geometrical focus, and the smallest lengths with polarization set perpendicular to the beam angle.

The 60–140 μ J energy range also marks the transition of a dominant parameter that controls the transverse angle. For polarization angles of 0 deg and -90 deg, the crack orientation gradually shifted from the direction of polarization towards the direction of a beam as the burst energy increased from 60 to 140 μ J. For polarization oriented perpendicular to the beam (at 45 deg), a sharp change was observed as the transverse angles were around 45 deg for $E_{\rm B}$ < 40 μ J and approximately at -45 deg for $E_{\rm B}$ > 40 μ J. For polarization

aligned along the beam major axis before the focus (at -45 deg), the angle remained around -45 deg for all the burst energies.

It should be reminded that the modifications were measured at such Z position, where the longest transverse modifications were observed. However, the lengths and angles of transverse modifications differed throughout the Z axis. The transverse length and angle dependencies on the Z position for different polarizations for the P10N1 regime with 55 and 160 μ J burst energies are given in Figure 34. The chosen burst energies reflect both transverse angle control regimes — via polarization and via beam asymmetry.

The transverse modifications were oriented parallel to the polarization throughout the Z axis for $E_B = 55~\mu J$ (Figure 34(a)). For a higher burst energy of 160 μJ , the transverse angles varied throughout the Z position with the modification bottom aligned to the polarization and modification front – close to the major axis of the beam. However, the transverse modifications maintained their orientation throughout the Z axis when polarization was aligned close to the major axis of the beam before the geometrical focus.

The variation of the transverse angle along the Z axis could be related to the depletion of the intra-burst pulse energy during the propagation. Initially, high energy leads to beam-oriented modifications, while further along the propagation, reduced energy allows polarization effects to take over. It could also be linked to a changing asymmetrical intensity distribution. During the propagation, the beam ellipticity might be reduced enough [198] to allow for polarization-based control.

For glass scribing purposes, maintaining the same transverse angle throughout the Z axis is crucial. Therefore, the modifications should be formed either with linear polarization at low burst energies or by aligning the linear polarization with the beam angle at high burst energies.

The transverse length dependence on the Z position is shown in Figure 34(c, d). The transverse lengths were similar (\sim 17 µm with $\sigma_{\rm stdev}$ = 2 µm) at different Z positions for $E_{\rm B}$ = 55 µJ for all polarization angles except the one set parallel to the beam angle. For the polarization oriented along the beam angle (at -45 deg), the transverse lengths varied throughout the Z position ($\sigma_{\rm stdev}$ = 6 µm), with the longest of 32 µm formed at around the center of a longitudinal modification. For higher burst energy of 160 µJ, the transverse lengths ranged between 5–40 µm throughout the Z position, with the longest formed at the front of the modification. At a specific Z position, the transverse lengths were similar for different polarization angles, except

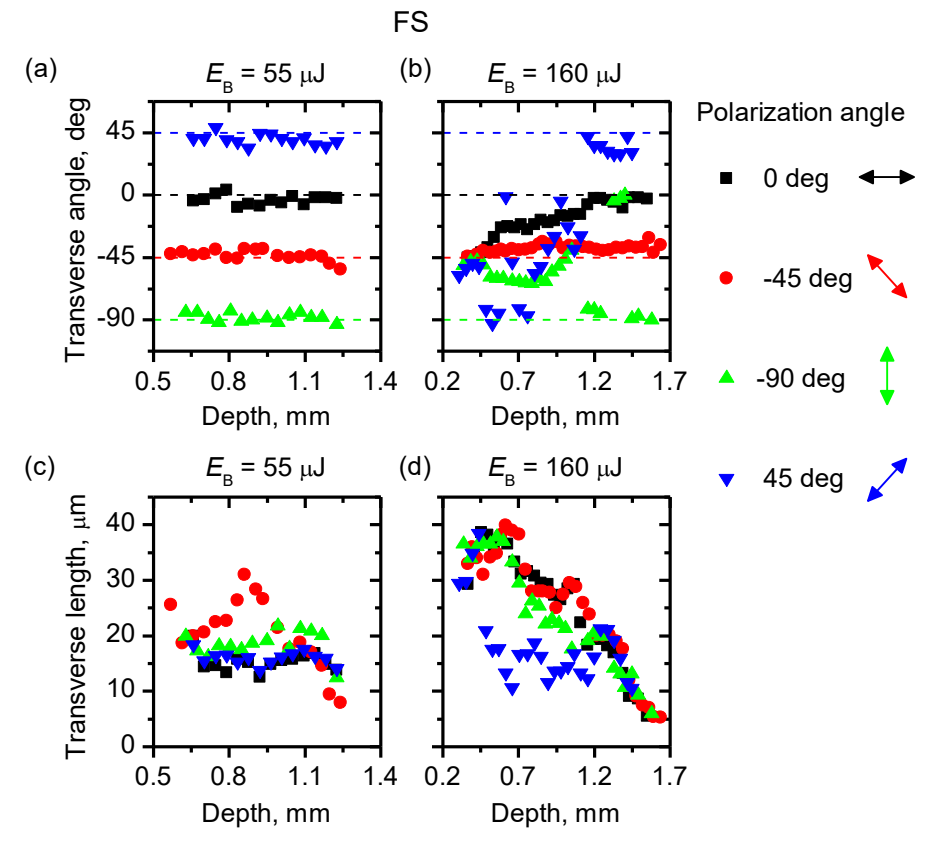


Figure 34. Modification transverse angle (a, b) and length (c, d) dependence on sample depth for polarization angles of 45 deg, 0 deg, -45 deg, and -90 deg. The depth value of 0 corresponds to the top surface of the sample. The modifications were formed in FS with the burst regime of P10N1 using burst energies of 55 μ J (a, c) and 160 μ J (b, d). The dashed horizontal lines on (a, b) graphs represent the polarization angles [A2].

when the polarization was set perpendicular to the beam, which resulted in shorter lengths.

Similar lengths throughout the depth are preferred for scribing as they ensure consistent overlap of the modifications. Therefore, using a polarization-controlled regime with polarization oriented at 45 deg, -45 deg, and -90 deg should be advantageous for scribing purposes.

4.2.2. Burst parameters

The OM pictures of the transverse modifications formed in FS and SLG with different burst parameters and polarization set vertically are shown in

Figure 35. The transverse modifications changed from uniform to more chaotic when the number of pulses per burst increased. This could be due to the initial intra-burst pulses creating a crack, which disrupts the propagation of the subsequent pulses, ultimately leading to the formation of chaotic cracks.

The images indicate that the burst energy and the number of pulses per burst impact the transverse length and angle. Therefore, the effect of these parameters on the transverse modifications will be investigated quantitatively. The transverse length dependence on the number of pulses per burst or BiBurst

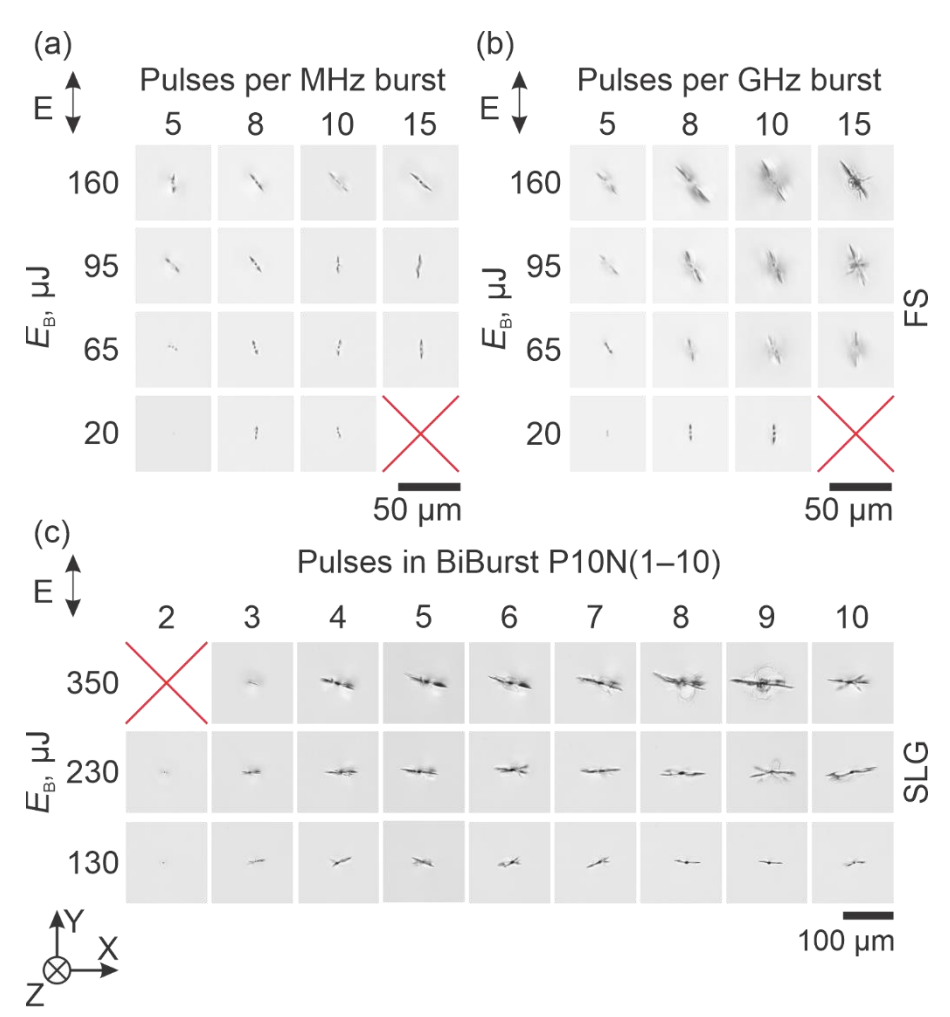


Figure 35. OM images of transverse modifications in the XY plane. The modifications were formed in FS (a, b) and SLG (c) samples using different burst energy and number of pulses per MHz (a) or GHz (b) bursts or BiBurst (c). The linear polarization was oriented at -90 deg. The parameter sets at which no modifications were seen are depicted with red crosses.

for different burst energies is shown in Figure 36. The transverse lengths increased with the burst energy. For the FS, in most cases, the modifications got longer as the number of pulses per MHz or GHz burst increased to 10. The tendency is unclear for the further pulse number increase to 20, as this resulted in either comparable length or longer modifications. The transverse lengths up to 46 μm were formed with the GHz burst, while the MHz burst resulted in 1.7 shorter lengths.

For the SLG, the transverse modifications got longer as the number of pulses per BiBurst increased from 20 (P10N2) to 50 (P10N5). Further increase in the number of pulses resulted in similar lengths for $E_B \le 160 \,\mu\text{J}$ or longer modifications for $E_B \ge 270 \,\mu\text{J}$. The longest modifications of 114 μ m were formed with the P10N10 regime at 350 μ J.

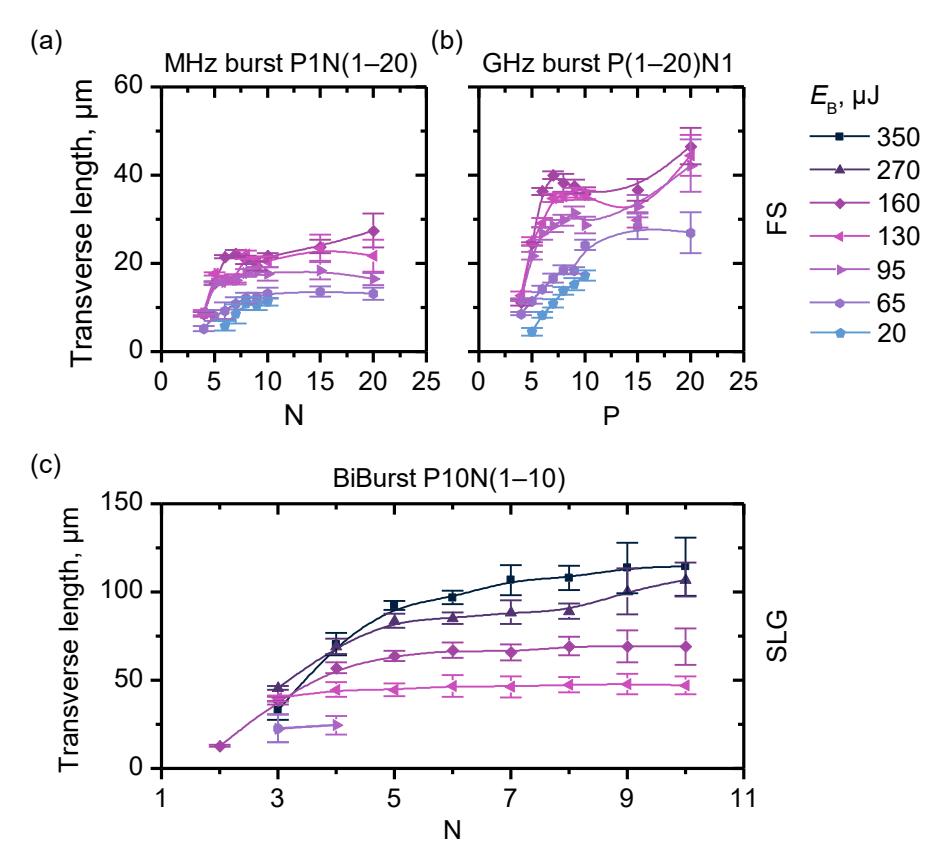


Figure 36. Transverse length dependence on pulses per MHz (a, c) and GHz (b, d) bursts for FS (b, d) and per BiBurst for SLG (c), when using different burst energies. The polarization was oriented at -90 deg. The data points are connected with lines for eye guidance [A2].

The transverse angle dependence on the number of pulses per burst for modifications formed with polarization set at -90 deg is shown in Figure 37. For the FS and MHz bursts, the number of pulses per burst had a different impact on the angle depending on the burst energy. For the GHz burst, increasing the number of pulses to 15 resulted in modifications rotating toward the polarization. P20N1 regime resulted in chaotic cracks, indicated by the large errors. For the MHz burst, increasing the number of pulses per burst to 10 resulted in modifications rotating toward polarization (for $E_B \le 65 \mu J$) or toward the beam major axis (for $E_B \ge 65 \mu J$).

For the SLG and the lowest burst energies of 130 and 160 μ J, the transverse angles were around 0 deg, with the number of pulses per burst having no clear impact. For higher burst energies of 270 and 350 μ J, reducing the number of

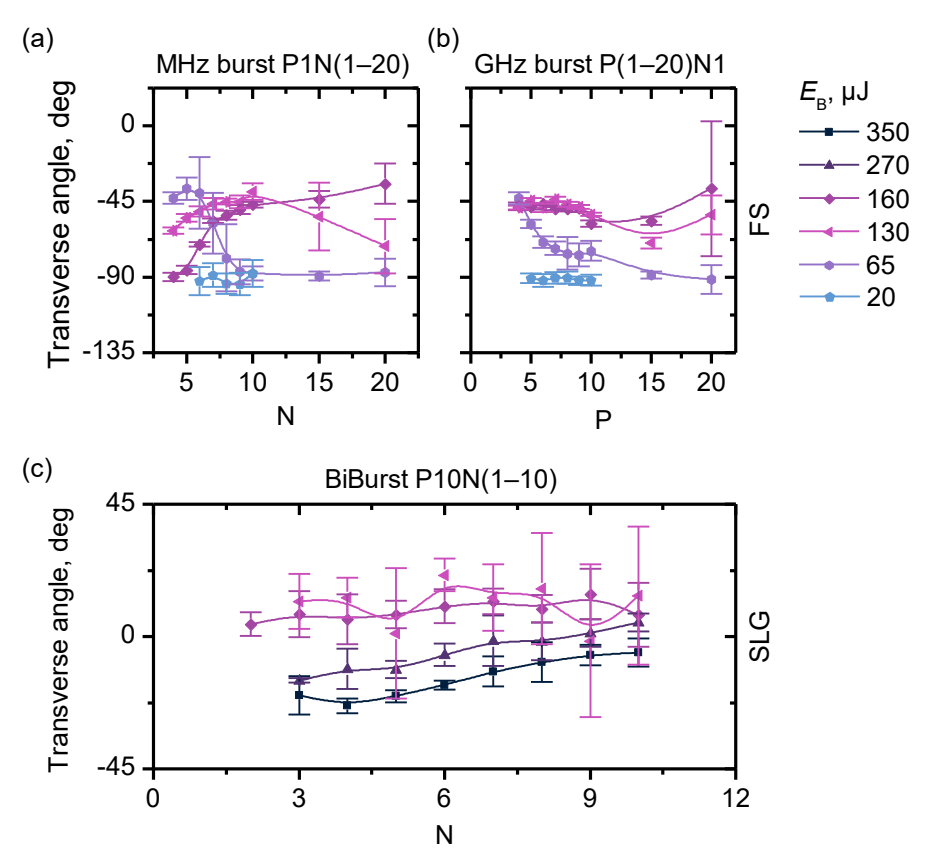


Figure 37. The transverse angle dependence on the number of pulses per MHz (a) or GHz (b) burst or BiBurst (c). The modifications were formed in FS (a, b) and SLG (c) using a vertical polarization (-90 deg).

pulses resulted in modification rotating towards the negative values (closer to the beam angle).

In most cases, higher burst energy and fewer pulses per burst—both resulting in higher intra-burst energy—led to modifications orienting towards the beam angle (Figure 37(b, c)). Therefore, we decided to investigate the transverse angle dependence on the intra-burst energy (Figure 38). Here, the intra-burst energy reflects the energy of the first pulse in a burst or BiBurst, calculated considering the temporal characteristic measurements (Figure 8). The P20N1 regime was excluded from Figure 38 due to having an additional pre-burst with a higher amplitude than the original burst (Figure 8(b)).

The transverse angle is shown to mainly depend on the intra-burst energy (Figure 38), as the number of pulses per burst or BiBurst had a negligible

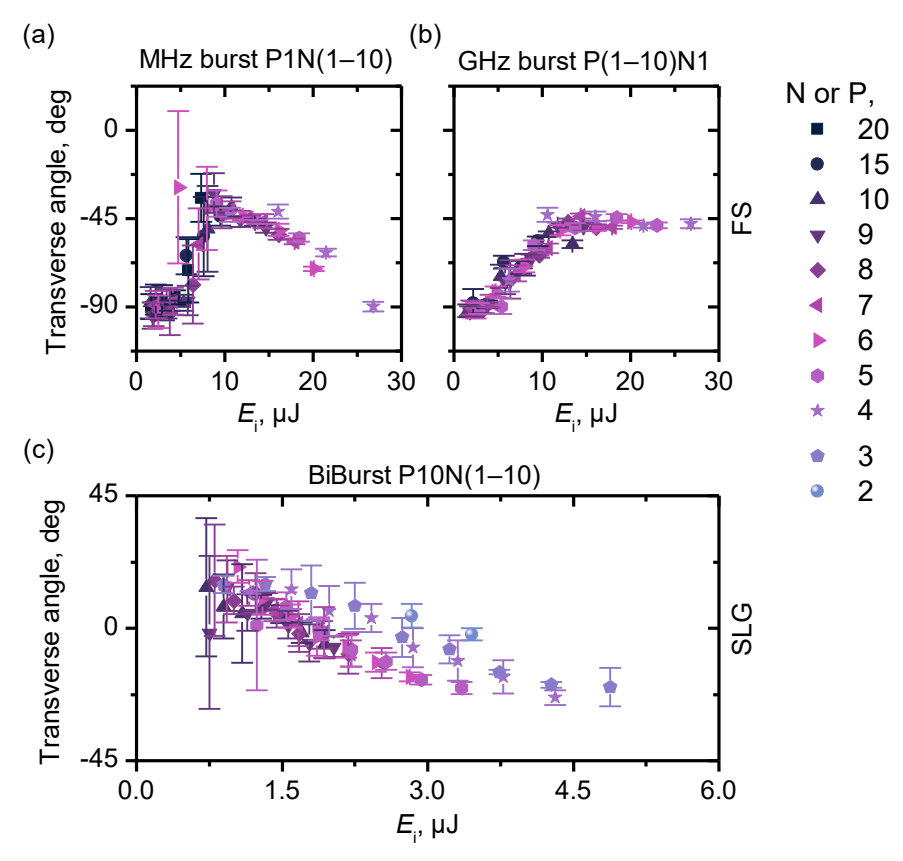


Figure 38. The transverse angle dependence on intra-burst pulse energy for different number of pulses per MHz (a) or GHz (b) burst or BiBurst (c). The modifications were formed in FS (a, b) and SLG (c) using polarization set vertically (-90 deg).

impact. For the FS, the lowest $E_{\rm i}$, up to ~5 $\mu \rm J$, resulted in modifications oriented along the polarization. Increasing the $E_{\rm i}$ to ~10 $\mu \rm J$ resulted in modifications orienting towards the beam angle. Further increment of the $E_{\rm i}$ resulted in no change for the GHz burst and modifications rotating towards the polarization for the MHz burst.

For the SLG, the modifications gradually rotated from 14 to -23 deg when increasing the E_i from 0.7 to 5 μ J. Both FS and SLG indicate that the intraburst energy is the main parameter for determining the transverse angle control mechanism.

The pulse duration impact on transverse modifications formed in SLG using the BiBurst regime of P10N5 is shown in Figure 39. The modifications become more chaotic for pulse durations of 2 ps and longer, compared to the one-directional modifications formed with shorter pulses. The study, which investigated modifications in glass using a Bessel-like beam, observed that the cracks transitioned from uniform to chaotic as the number of pulses per burst or pulse duration increased [12].

Figure 40 shows the dependence of transverse angle and length on pulse

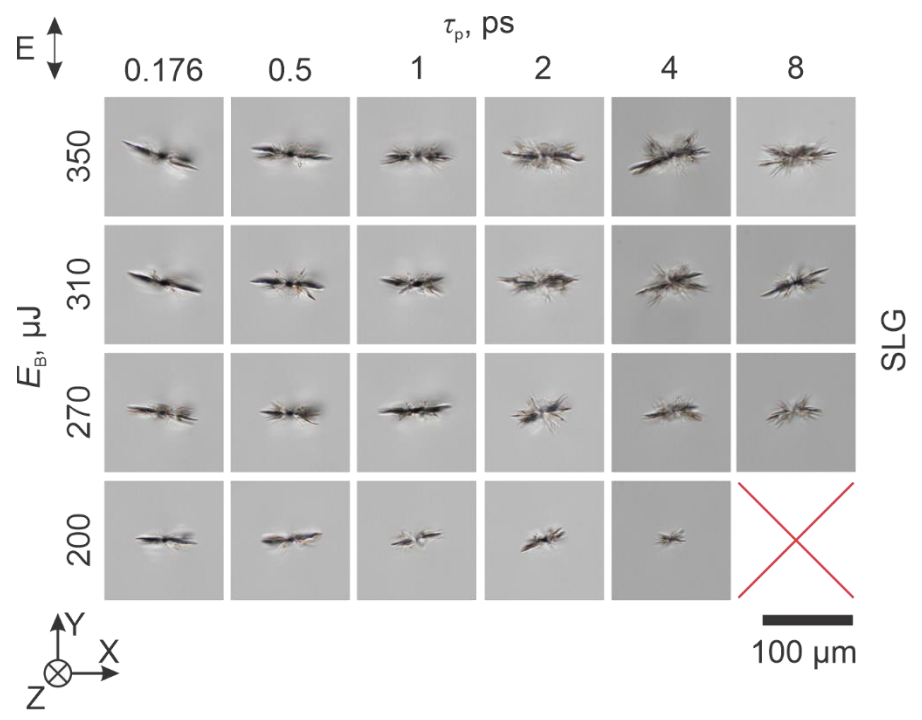


Figure 39. Impact of pulse duration and burst energy on transverse modifications formed in SLG. OM pictures of modifications formed using BiBurst regime P10N5 and polarization set vertically (-90 deg).

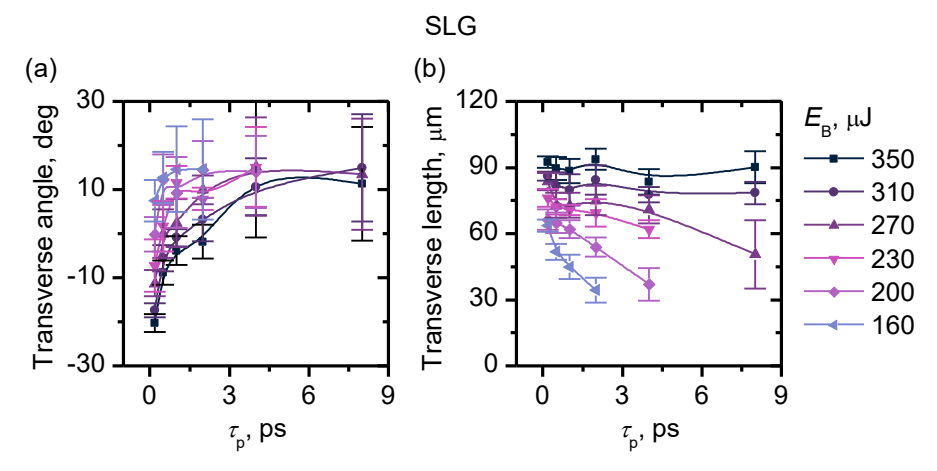


Figure 40. Dependence of transverse angle (a) and length (b) on pulse duration for modifications formed in SLG using different burst energies. The modifications were formed using the P10N5 BiBurst regime and polarization set vertically (-90 deg).

duration for different burst energies. For burst energies of $160\text{--}350~\mu\text{J}$ and pulse durations of 0.176--8~ps, the transverse angle ranged between -20–15 deg (Figure 40(a)). Higher burst energy and shorter pulse duration, both of which lead to higher peak intensities, resulted in modifications rotating towards the negative angles. Both transverse and longitudinal lengths also increased under these conditions (Figure 40(b), Figure 28). The longest transverse (~90 μ m (Figure 40(b))) and longitudinal (~840 μ m (Figure 28)) modifications were formed with a 176 fs pulse duration and 350 μ J burst energy.

4.3. Summary

Experiments have revealed the importance of a burst regime for volumetric elongated modification formation in FS and SLG when using femtosecond pulses and NA of 0.04. No modification was observed in samples with a single-pulse regime and peak powers greater than the critical power for self-focusing. The phenomenon was linked to an insufficient electron density, as lower density is required to counteract self-focusing and diffraction when using low NA. Elongated modifications were only formed by applying the burst or BiBurst regimes. In FS, at least 5 pulses per MHz and 4 pulses per GHz bursts were needed to form modifications. For the SLG, the

modifications were created with BiBurst regimes consisting of at least 20 pulses.

The homogeneity of longitudinal modifications was inspected for the FS samples. Uniform longitudinal modifications were only formed with GHz bursts consisting of 8 or more pulses, showing that the number of pulses per burst and the intra-burst repetition rate are highly important. Modifications with lengths over 300 µm formed with MHz bursts were split along the propagation path into several parts. Despite this, the overall length and position of the longitudinal modifications were of similar value for both MHz and GHz bursts when using the same parameter sets. The longest modifications (~1.4 mm) in FS were formed with 7–10 (MHz) and 6–10 (GHz) pulses per burst using the highest burst energy of 170 µJ. For the SLG, the longest modifications of 0.9 mm were formed using P10N3 BiBurst with the highest burst energy of 350 µJ and the shortest pulse duration of 176 fs.

In both FS and SLG, higher burst energy increased the longitudinal lengths and the range of the number of pulses per burst needed to form modifications. Furthermore, the GHz burst allowed using a higher range of pulses per burst compared to the MHz bursts when forming modifications in FS. The range of the number of pulses per burst exists as this parameter changes the intra-burst pulse energy and the number of cumulative cycles, both of which are important for the creation of modifications.

The longitudinal modification positions were measured only for FS samples. The modifications formed closer to the front surface when using higher intra-burst energy. The modification front position was accurately calculated (with errors of up to 10%) using Dawes and Marburgers and lens formulae (equations (13) and (28)) by only using the intra-burst pulse energy as a variable.

The transverse angles were determined by linear polarization or beam ellipticity, depending on the intra-burst energy. For low intra-burst energies, the modifications formed parallelly (for FS) or perpendicularly (for SLG) to the polarization. The intra-burst energy increase resulted in modifications rotating towards the beam ellipticity. However, modifications formed in FS using MHz bursts started rotating towards the polarization when the intra-burst energy increased from $10~\mu J$.

The transverse angles along the Z axis were measured for the FS sample using P1N10 and P10N1 regimes. For higher burst energies, the transverse modifications were oriented along the beam angle at the front of the modification, while at the bottom of the modification, the angle was aligned along the linear polarization. The transverse modification angle remained the same at different Z positions for the polarization-controlled regimes and when

the polarization was set along the beam. However, the transverse lengths differed throughout the Z position for $E_{\rm B}=160~\mu{\rm J}$ and for a polarization-controlled regime with polarization set along the beam angle. The transverse lengths at different Z positions were similar for polarizations oriented at 45 deg or greater relative to the beam angle.

The transverse modifications transitioned from uniform to more chaotic as the number of pulses per burst increased. In most cases, the modifications got longer with higher burst energy, and the number of intra-burst pulses increased to 10 (for FS) and to 50 (for SLG). The transverse lengths up to 46 μm were formed in FS with the GHz burst, while the MHz burst resulted in 1.7 shorter lengths. The modifications in SLG reached 114 μm , formed with the P10N10 regime at 350 μJ .

The impact of pulse duration on transverse modifications was investigated for SLG using the P10N5 BiBurst regime. Transverse modifications changed from unidirectional to omnidirectional as the pulse duration increased from hundreds of femtoseconds to a few picoseconds. Transverse and longitudinal lengths increased with higher burst energy and lower pulse duration, resulting in higher peak intensities. At the pulse duration of 176 fs and burst energy of 350 μJ , the transverse lengths reached ~90 μm , while the longitudinal lengths were ~840 μm .

5. SODA-LIME GLASS SCRIBING

In this section, single-shot modifications with polarization-controlled transverse angles, formed via filamentation, were utilized for 1.1 mm-thick SLG scribing. The scribing was carried out using a simple and fast beam positioning system, consisting of galvanometer scanners and a telecentric f-theta lens, which enabled scanning speeds of several meters per second.

The experimental setup is illustrated in Figure 7, while the scribing and sample separation processes, together with separation stress simulation, are described in Sub-subsection 2.2.3. Results provided in this section were published in [A1] research paper.

5.1. Single-pass scribing

The single-shot experiments in Section 4 have shown that the BiBurst regime plays a critical role in forming modifications inside SLG via filamentation, as modifications were formed with BiBurst regimes consisting of at least 20 pulses. Therefore, the BiBurst regimes of P10N(2–10) were considered for scribing. For the scribing purposes, uniform modifications with extended longitudinal and transverse dimensions are preferred. The length of the modifications is shown to increase with the burst energy (Figure 27(c), Figure 36(c)). For $E_B \ge 200 \,\mu\text{J}$, a higher number of pulses per BiBurst (P10N(6–10)) is shown to lead to chaotic transverse cracks (Figure 35(c)). Using fewer pulses per BiBurst resulted in longer longitudinal (Figure 27(c)) but shorter transverse lengths (Figure 36(c)). Therefore, the scribing investigation was conducted using an intermediate P10N5 BiBurst regime.

It is essential to align the crack angles along the scribing line to achieve faster scribing at higher quality [127,134]. The crack angle can be controlled with polarization, as demonstrated in Sub-subsection 4.2.1. The OM pictures of the samples scribed with different polarization angles are provided in Figure 41. The beam was focused to the bottom surface of the sample, creating a modified zone closer to this surface. Consequently, the samples were separated by applying tension to the bottom surface.

The smallest deviation of the separation line from the scribing line occurred with polarization set perpendicular to the scribing line. Consequently, further scribing experiments were done by scanning the beam along the X axis while the polarization was set along the Y axis. This

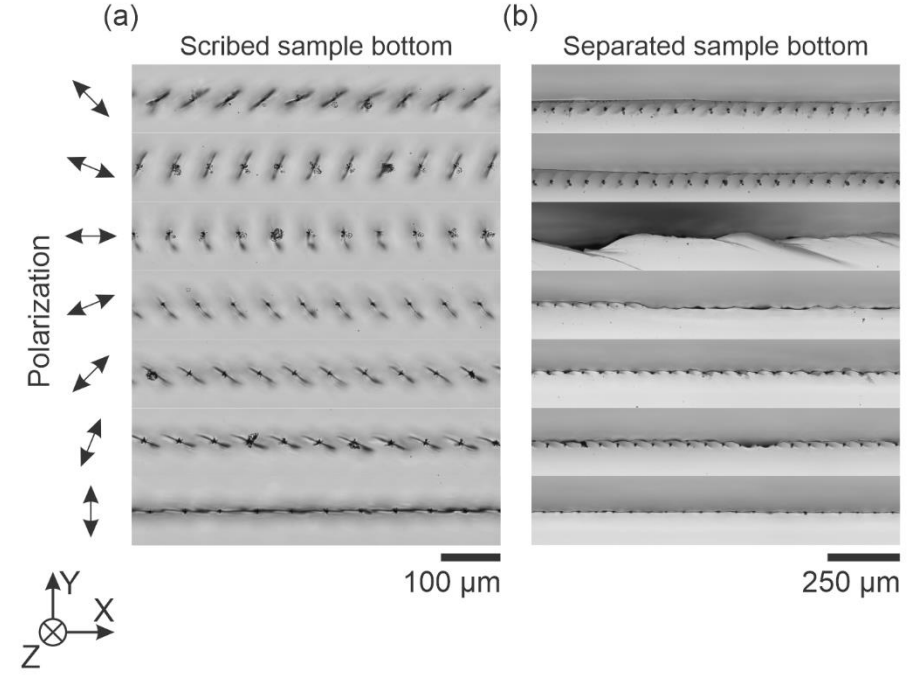


Figure 41. Polarization impact on scribing (a) and separation (b). Scribing was done using BiBurst regime P10N5, $\tau_p = 176$ fs, $f_B = 100$ kHz, $E_B = 300$ µJ, and $v_{\text{scan}} = 6$ m/s with the beam focused to the bottom surface [A1].

alignment ensured that the transverse modifications were parallel to the scribing path.

5.1.1. Scanning speed and pulse duration

In this sub-subsection, scribing was performed with a beam focused to the bottom surface, and separation was performed by tensioning the bottom surface. The impact of pulse duration and beam scanning speed on sample separation stress can be seen in Figure 42. The lowest separation stress of 18 MPa was achieved with $v_{\rm scan}=6$ m/s, $\tau_{\rm p}=176$ fs, and $E_{\rm B}=300$ $\mu{\rm J}$. The single-shot experiments show that longer pulses result in omnidirectional modifications (Figure 39) and shorter longitudinal lengths (Figure 28), which may explain the increased separation pressure for a pulse duration of 4 ps at a burst energy of 300 $\mu{\rm J}$.

For a lower burst energy of 200 μ J, the separation stress was higher, with the lowest being ~27 MPa for τ_p = 1–4 ps, while the shortest pulse duration of 176 fs resulted in a higher value of 32 MPa.

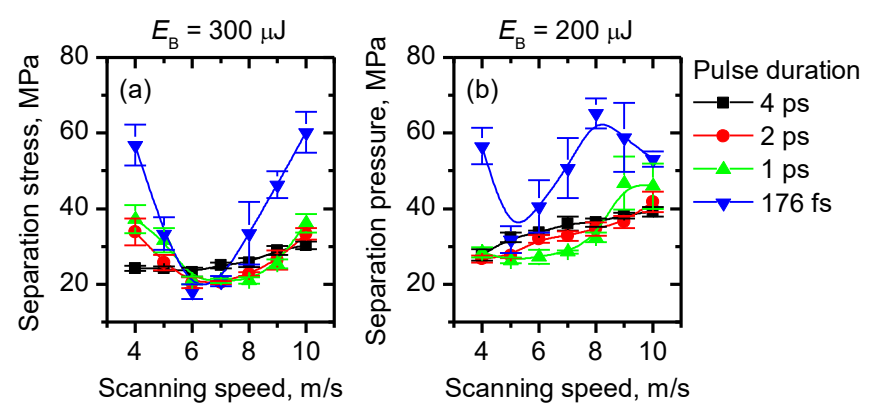


Figure 42. Dependence of separation stress on scanning speed for different pulse duration and $E_B = 200 \,\mu\text{J}$ (a) and 300 μJ (b). Scribing was performed with the BiBurst regime P10N5, $f_B = 100 \,\text{kHz}$, the beam focused to the bottom surface, and polarization set perpendicular to the scribing line [A1].

The top and bottom surfaces of samples scribed at 6 m/s with different pulse durations were inspected with an OM (Figure 43). The top surface had fewer defects as opposed to the bottom surface, where chippings were formed. The largest chippings were formed with a lower burst energy of 200 μ J and longer pulse durations of 1–4 ps. The best surface quality was reached with the shortest pulse duration of 176 fs.

The top and bottom surface quality was assessed by measuring the length of the largest chipping (Figure 44). The mean chipping length on the front

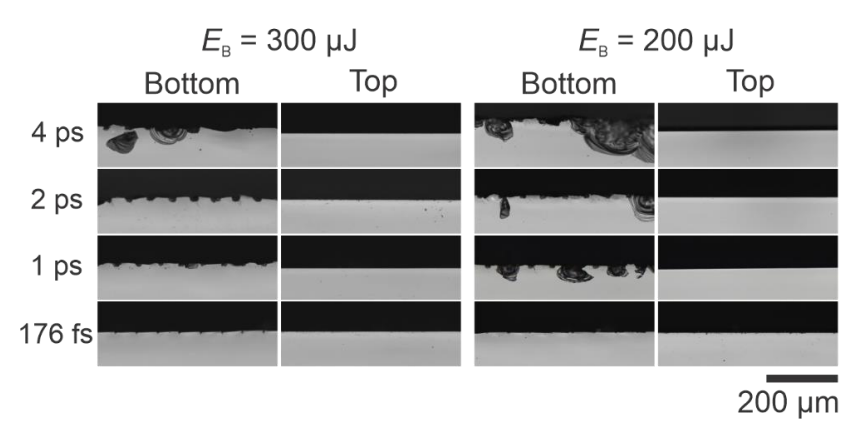


Figure 43. OM pictures of the top and bottom surfaces of the scribed samples. Scribing was done with BiBurst regime P10N5, $f_{\rm B} = 100 \, \rm kHz$, $E_{\rm B} = 300, 200 \, \mu \rm J$, and $v_{\rm scan} = 6 \, \rm m/s$, the beam focused to the bottom surface, and polarization set perpendicular to the scribing line [A1].

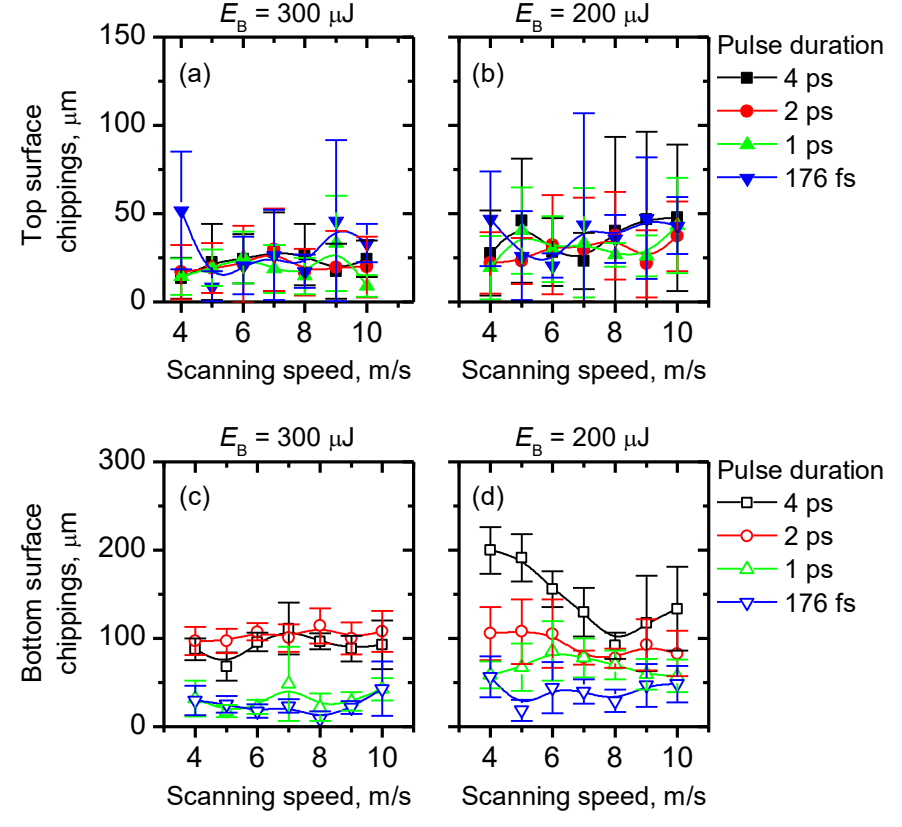


Figure 44. Dependence of top (a, b) and bottom (c, d) surface chippings on scanning speed for burst energies of 300 μ J (a, c) and 200 μ J (b, d). The scribing was done with BiBurst regime P10N5, $f_{\rm B} = 100$ kHz, $\tau_{\rm p} = 0.176$ –4 ps, and $v_{\rm scan} = 4$ –10 m/s. The beam was focused to the bottom surface, and polarization was set perpendicular to the scribing line.

surface was up to 60 μ m for all the tested parameters, with no visible tendency. The largest chippings on the bottom surface were formed with the longest pulse duration and the lowest burst energy. For $E_B = 300~\mu J$, the chippings were ~100 μ m for $\tau_p = 2$ –4 ps. However, for shorter pulse durations of 1 ps and 176 fs, smaller chippings of ~30 μ m were formed. For a lower burst energy of 200 μ J, the chippings decreased with each shorter pulse duration, with the shortest pulse duration resulting in ~40 μ m chippings.

The sidewall roughness R_a and waviness W_a were measured at different sample depths for samples scribed at 6 m/s using the P10N5 regime with $E_B = 300 \mu J$ and $\tau_p = 176$ fs. The sidewall surface consisted of a modified zone at the bottom and a mirror-like zone at the top (Figure 45(a)). The mirror-like

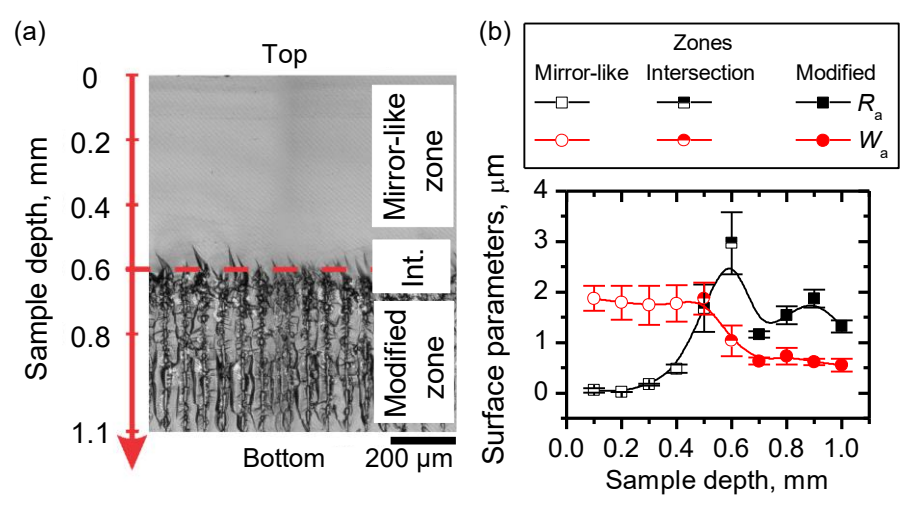


Figure 45. Sidewall surface (a) and its quality versus sample depth (b). The surface was separated into modified, intersection, and mirror-like zones. The dashed line in (a) represents the direction of a profile used for R_a and W_a calculation. Scribing was done with BiBurst regime P10N5, $\tau_p = 176$ fs, $f_B = 100$ kHz, $E_B = 300$ µJ, and $v_{\text{scan}} = 6$ m/s. The beam was focused to the bottom surface, and the polarization was set perpendicular to the scribing line [A1].

zone had the highest W_a of 2 μ m and the lowest R_a of 0.02 μ m (Figure 45(b)). Higher W_a values indicate poorer control of the cleavage plane propagation. The R_a of the modified zone increased to 2 μ m, and the W_a reduced to 0.6 μ m. However, the highest R_a of 3 μ m was achieved at the intersection of the mirror and modified zones, where hackle marks were formed.

The quality of the sidewalls was inspected for samples scribed at different speeds using P10N5 burst regime, $\tau_p = 176$ fs, and $E_B = 300 \,\mu\text{J}$ (Figure 46). Samples scribed at a speed of 4–5 m/s using 300 μ J burst energy had inclined modifications. Periodical inclined modifications on the sample sidewalls were seen in sapphire scribed using a burst regime [207]. The phenomenon was explained by the enhanced-absorption zones created by the previous pulses. Thus, with each pulse, the laser beam is absorbed at a higher part of the sample until the fluence is insufficient to induce further modifications. This results in inclined cracks forming upward and toward the beam scanning trajectory.

As the scribing was performed with a burst repetition rate of 100 kHz, the distance between the shots ranged from 40 to 100 μ m for the scanning speeds of 4 to 10 m/s. The distance of 40 μ m is high enough to avoid the overlapping of the filaments, considering that the typical diameters in glasses reach up to 10 μ m [55–57]. In addition, the time of 10 μ s between the subsequent pulses is insufficient for heat to travel the 40 μ m distance, as 3.2 ms is required

(calculated using 0.5 mm²/s thermal diffusivity of SLG [44]). Consequently, thermal effects from prior pulses should not impact the subsequent pulses. However, the cracks could have affected the subsequent pulses, as they also can reduce the damage threshold [220]. Thus, each pulse could damage the material at a higher part of the sample. Hendrick *et al.* have demonstrated that the crack length increases with each pulse in a MHz burst due to transversal shear waves propagating at a speed of 3.5 μ m/ns [178]. At a 10 μ s interval between shots, the shear wave travels ~12 mm, indicating that the cracks are fully formed by the time the next shot occurs. The transverse length of the single-shot modification formed with 176 fs, 300 μ J, and P10N5 reached 86 μ m. Therefore, the cracks overlapped using the scanning speeds of 8 m/s or lower.

In this work, inclined modifications were avoided by scanning the beam at 6 m/s or higher (Figure 46(a)). This could be explained by the reduced influence of the previous pulses due to the larger modification center-to-center distance and reduced overlapping of the cracks.

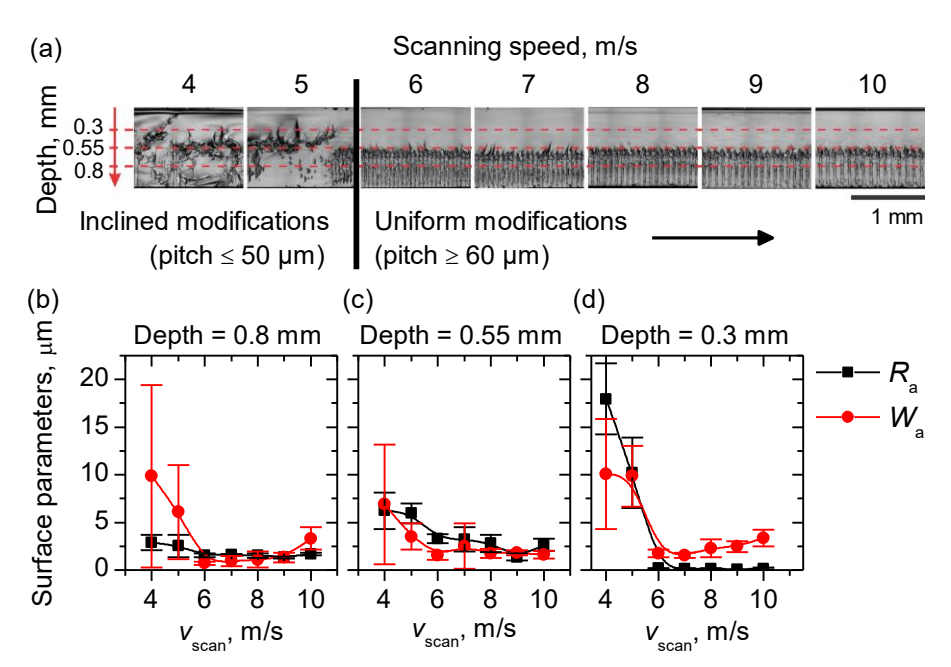


Figure 46. OM images of sidewall surfaces of samples scribed at different speeds (a). The pitch depicts the centre-to-centre distance between the modifications. The dependence of sidewall surface parameters (R_a and W_a) on scribing speed when measuring at 0.8 mm (b), 0.55 mm (c), and 0.3 mm (d) sample depth. The scribing was performed with BiBurst regime P10N5, $\tau_p = 176$ fs, $f_B = 100$ kHz, $E_B = 300$ μ J with the beam focused to the bottom surface. The polarization was perpendicular to the scribing line [A1].

The sidewall images can also help to explain the separation stress dependence on scribing speed shown in Figure 42(a) for 176 fs pulses and 300 μ J burst energy. The lowest separation stress occurs with the most uniform modification plane, which is formed using a scanning speed of 6 m/s. At lower speeds, inclined modifications are formed, while higher speeds result in non-optimal overlap of the modifications.

The modified and mirror-like zones, as well as their intersection, were investigated by measuring roughness and waviness at the depths indicated by the dashed lines in Figure 46(a). The samples with inclined modifications (scanning speed of 4–5 m/s) exhibited the poorest surface quality. Considering that the W_a and R_a were significantly higher than those of the samples scribed at higher speeds, only the results using 6–10 m/s scanning speed will be discussed more thoroughly. At the bottom and the middle parts of the sample, the W_a and R_a ranged between 0.7 and 3.3 µm (Figure 46(b, c)). The top part of the sample had W_a about an order of magnitude larger than R_a and reached 3.4 µm (Figure 46(d)). Furthermore, higher scanning speeds resulted in higher waviness of the sidewall top part. In other words, higher distances between the shots increased the separation path deviation for the unmodified zone.

5.1.2. Focus position

Photographs of separated samples scribed with various focus positions are shown in Figure 47. The position of the modified zone depended on the focus position. The samples were separated by applying tension to the surface nearer the modified zone. Therefore, the bottom surface was tensioned for ≥ 0.9 mm and the top surface for ≤ 0.7 mm focus positions. It should be noted that for focus positions smaller than 0.5 mm, the sample separation was unstable, often resulting in the sample breaking into more than two pieces and the separation line deviating from the scribing line. The sidewalls of samples scribed by focusing the beam at 0.9 mm and smaller focus positions had additional hackle cracks formed between the modifications and the tensioned surface. In these cases, the laser-induced modifications did not touch the tensioned surface, which led to the formation of additional cracks. It is also seen that the filament-induced damage did not distribute evenly for focus positions of 0.5 and 0.7 mm, with some parts being modification-free. As these modifications were formed near the top surface, absorption at the top surface could have occurred, disrupting the beam propagation. This is supported by the fact that damaged zones were inspected on the top surface.

Tensioned surfaces

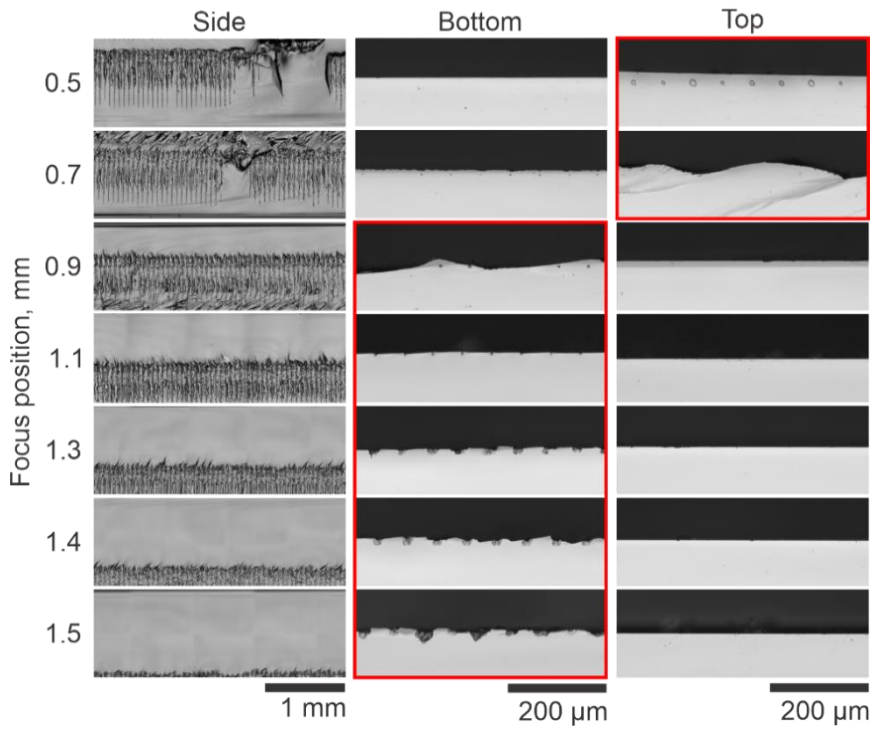


Figure 47. OM images of sidewalls, top, and bottom surfaces of separated samples. Scribing was done with BiBurst regime P10N5, $\tau_{\rm p}=176\,{\rm fs}$, $f_{\rm B}=100\,{\rm kHz}$, $E_{\rm B}=300\,{\rm \mu J}$, and $v_{\rm scan}=6\,{\rm m/s}$. The beam was focused at different depths, and the polarization was perpendicular to the scribing line. The samples were separated by tensioning either the bottom (1.5–0.9 mm) or top (0.7–0.5 mm) surfaces, outlined with red rectangles [A1].

The dependence of separation stress on focus position is shown in Figure 48(a). The graph is colored blue and pink for the top and bottom tensioned surfaces, respectively. There are two minimums, each corresponding to the front or bottom tensioned surface. The minimal separation stress was 30 ± 4 MPa and 18 ± 2 MPa, respectively, when the beam was focused to depths of 0.5 mm and 1.1 mm. To explain these minima, the modified zone position and length were measured, as shown in Figure 48(b).

The modifications reached the bottom surface when the beam was focused to 1.1 mm or deeper (Figure 48(c)). However, it was impossible to form modifications reaching the top surface as a certain distance is needed for the Kerr effect to build up [126]. It is crucial to form modifications as close to the

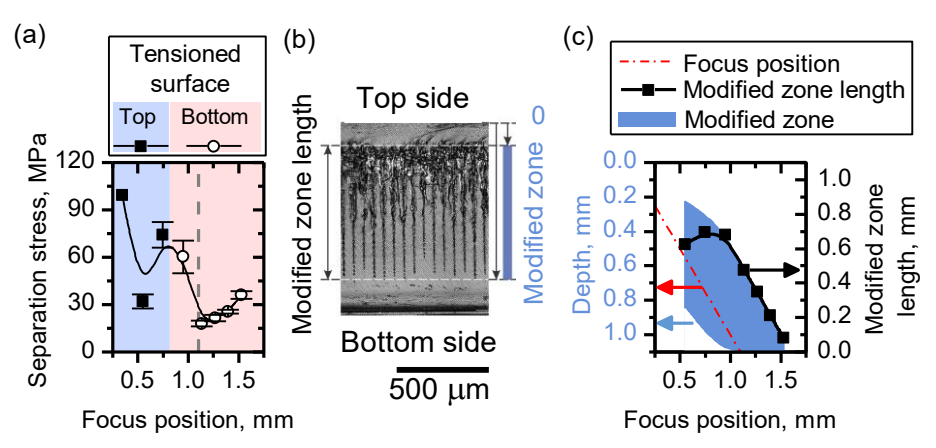


Figure 48. Dependence of separation stress on laser focus position (a) with respect to the top surface of the sample (0 mm). The blue and pink zones indicate which surface, top or bottom, was tensioned during separation. The gray dashed line represents the bottom surface of a sample. Measurement of the modified zone length and position (b) and their dependence on focus position (c). The scribing was done by scanning the beam at 6 m/s speed, using a BiBurst regime P10N5, $\tau_p = 176$ fs, $f_B = 100$ kHz, $E_B = 300$ µJ, and $v_{scan} = 6$ m/s. The polarization was perpendicular to the scribing line [A1].

tensioned surface as possible, as the highest tensile stresses are created there [203]. Because of this, the lowest separation stress was achieved with modifications positioned at the bottom (Figure 48(a)).

Another important aspect is the modification zone length, as it affects the separation stress of the samples. The longest modifications were formed with the focus position of 0.7 mm; however, they did not reach the top or bottom surfaces. Therefore, the minimal separation stress for the top-tensioned surface was achieved with a smaller focus position of 0.5 mm, resulting in a reduced modification-to-surface distance. Even smaller focus positions resulted in lower modified zone length and an unstable separation process. For the bottom surface, the lowest separation stress was achieved at such a focus position where the modifications reaching the bottom surface were the longest (0.5 mm). This focus position happened to be the bottom surface.

5.2. Double-pass scribing

The results of single-pass scribing indicate that higher quality and smoother separation are achieved with modifications formed closer to the bottom surface. The separation process could further be improved by forming a longer

modified zone, thereby reducing the flexural strength of the sample [110]. Therefore, two scribing lines were scanned at different focus positions, as shown in Figure 49(a). The first line was scribed at focus position Z_1 (1.1 mm) and the second line – at Z_2 . The position of the second line was changed from 1.1 mm to 0.3 mm in increments of 0.2 mm. Both lines were scribed with the same burst energy of either 300 μ J or 200 μ J. The beam scanning speed was 6 m/s, resulting in twice lower effective scribing speed due to the two lines being scanned.

The dependence of separation stress on the Z_2 position is shown in Figure 49(b). For both burst energies, the minimal separation stress of ~12 MPa was achieved with the second line focused at 0.7 mm. However, for $E_B = 300 \,\mu\text{J}$, a similar separation stress was achieved in the Z_2 range of 0.5–0.9 mm. To explain the minima points, pictures of the sidewall surfaces were taken (Figure 49(c)). The images indicate that there is an optimal Z_2

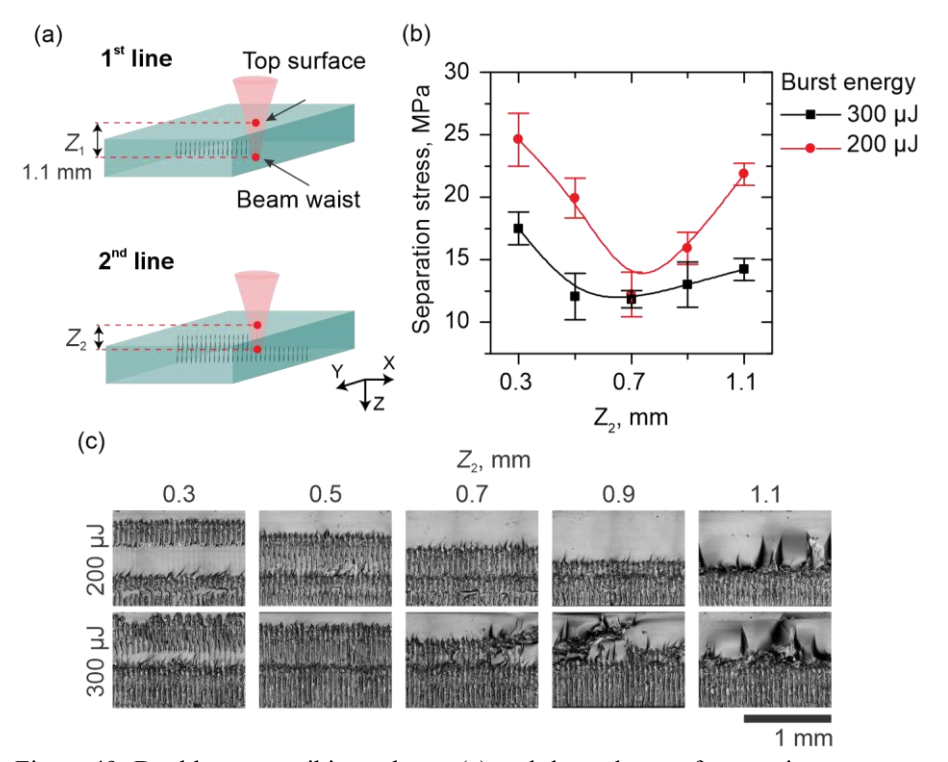


Figure 49. Double-pass scribing scheme (a) and dependence of separation stress on the $2^{\rm nd}$ scribing line position (Z_2) with the first line focused at 1.1 mm (b), and the OM pictures of sample sidewalls. Scribing was done with BiBurst regime P10N5, $\tau_{\rm p} = 176$ fs, $f_{\rm B} = 100$ kHz, and $E_{\rm B} = 200$ µJ (red circle) and 300 µJ (black square). The beam was scanned at a speed of 6 m/s. The polarization was perpendicular to the scribing line [A1].

position: focusing above this position leads to non-overlapping modified zones, while focusing below it causes a reduction in modified zone length, sometimes accompanied by inclined modifications.

The Z_2 should be chosen considering the separation stress and sidewall quality. In that case, the optimal Z_2 would be 0.5 mm for $E_{\rm B}=300~\mu{\rm J}$ and 0.7 mm for $E_{\rm B}=200~\mu{\rm J}$.

The R_a and W_a parameters of sidewall surface dependence on the sample depth for samples scribed with 200 and 300 μ J using an optimal Z_2 position are shown in Figure 50. Over the large extent of the modified zone, the W_a was lower than R_a and remained below 2 μ m. The roughness increased at the intersection between the mirror and modified zones, and towards the bottom surface. The modified zone exhibited approximately 1.5 times lower roughness in samples scribed with 200 μ J burst energy ($R_a \sim 2 \mu$ m) compared to those scribed with 300 μ J.

The dependence of separation stress on modified zone length is shown in Figure 51. The experimental data points correspond to the samples with separation stresses depicted in Figure 48 and Figure 49, with modified zone lengths measured as shown in Figure 48(b). Only experimental data of samples with modified zones reaching the bottom surface and overlapping zones (for double-pass scribing) were considered. Figure 51 also includes theoretical values based on the inert and sub-critical crack growth models (described in Sub-subsubsection 2.2.3.1). The experimental data points correlate well with the models, as separation stress decreased with longer

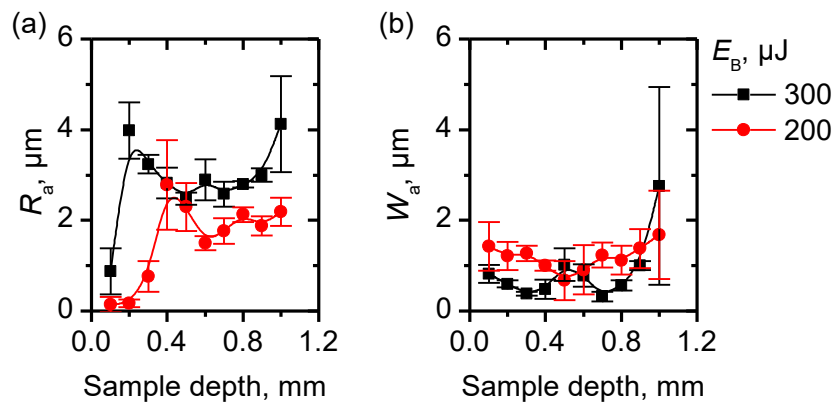


Figure 50. The R_a (a) and W_a (b) dependence on sample depth. The samples were scanned twice at $Z_1=1.1$ mm and $Z_2=0.5$ mm ($E_B=200~\mu J$) or $Z_2=0.7$ mm ($E_B=300~\mu J$) focus positions. The scribing was performed with a BiBurst regime P10N5, $\tau_p=176$ fs, and $f_B=100$ kHz. The beam was scanned at a speed of 6 m/s. The polarization was perpendicular to the scribing line [A1].

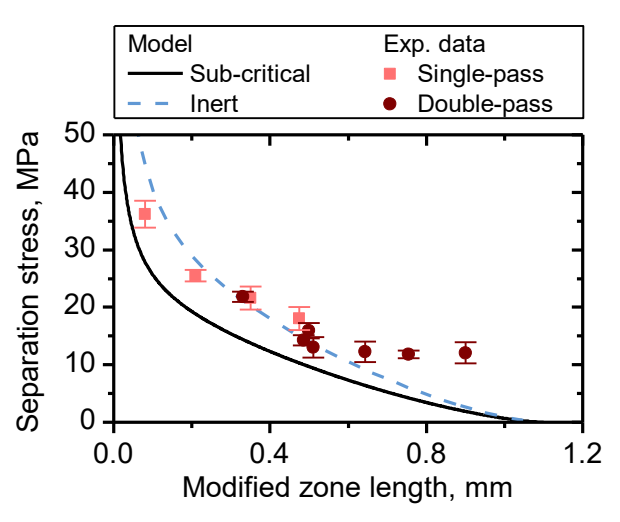


Figure 51. Separation stress dependence on modified zone length. The figure includes estimation by inert (blue dashed line) and sub-critical crack growth (black line) models described in Sub-subsubsection 2.2.3.1, and experimental data of single-pass (pink squares) and double-pass (dark red circles), taken from Figure 48 and Figure 49, respectively [A1].

modified zone lengths. The experimental points differed from the inert model by up to 25% for the modified zone lengths of up to 0.6 mm (around half the sample thickness). However, the experimental data and the model difference increased for longer modified zones.

The deviation between the model and experimental data occurs due to non-perfect modification distribution, as the transverse length differs throughout the Z position (Figure 34(c, d)). The model is based on the ideal crack, described as a uniform crack through the entire plane of modification. However, the sidewall surface pictures (Figure 46, Figure 47, Figure 48(b), and Figure 49) indicate that the cracks connected unevenly at different depths. Furthermore, in the ideal case, the spatial distribution of the modifications should be evaluated before the separation, preventing the formation of additional cracks. The absence of hackle marks would also result in a more precise measurement of the modified zone length.

The optimal parameter sets of double-pass scribing, together with single-pass scribing results obtained at the same scanning speed of 6 m/s, are shown in Table 6. Higher burst energy of 300 μ J should be used for single-pass scribing as it resulted in approximately twice lower separation stress and bottom surface chippings. For double-pass scribing, both energies resulted in similar quality and separation stress, except for the roughness of the modified zone, which was 1.5 times lower for a burst energy of 200 μ J.

Table 6. Separation stress, top and bottom surface chippings, R_a and W_a of the samples scribed with a single-pass and double-pass using optimal focus positions of Z_1 and Z_2 . The R_a was measured at the modified zone, and the W_a at the mirror-like zone. Scribing was performed using the BiBurst regime P10N5, $\tau_p = 176$ fs, $f_B = 100$ kHz, with polarization set perpendicular to the scribing line. Values are given in (mean \pm a standard deviation) format.

Ε, μJ	Z ₁ , mm	Z ₂ , mm	v _{scan} , m/s	σ _b , MPa	Top surface chippings, um	Bottom surface chippings,	Modified zone R _a , μm	Mirror zone W _a , μm
					•	μm	·	
SINGLE-PASS SCRIBING								
200	1.1	-	6	41 ± 7	21 ± 7	44 ± 29	1.9 ± 0.8	1.5 ± 0.6
300	1.1	-	6	18 ± 2	21 ± 16	18 ± 7	1.8 ± 0.6	1.8 ± 0.1
DOUBLE-PASS SCRIBING								
200	1.1	0.7	6	12 ± 2	19 ± 11	26 ± 19	2.0 ± 0.3	1.2 ± 0.2
300	1.1	0.5	6	12 ± 2	23 ± 12	27 ± 14	3.1 ± 0.6	0.8 ± 0.2

Double-pass scribing allowed achieving 1.5 times lower separation stress while preserving similar quality. Nevertheless, the twice faster single-pass scribing process is superior when considering the scribing speed.

In our experiments, the scanning speed was limited to 10 m/s due to the technical constraints of the galvanoscanner. However, we determined that the optimal speed for minimizing sample separation stress was 6 m/s, suggesting that other process parameters also influence the maximum achievable scribing speed. Higher scribing speeds could be attained by either (i) increasing the burst repetition rate while maintaining the same pulse energy of 300 µJ, or (ii) enlarging the spacing between modifications by using higher burst energies. Both strategies demand a higher average laser power. However, since higher burst energies tend to degrade the quality of transverse modifications, increasing the repetition rate appears to be a more favorable approach. Although some commercial laser systems could theoretically support scribing speeds of up to 24 m/s—requiring four times the average power of our current setup—this would require using a polygon scanner. However, this would come at the cost of reduced scanning flexibility.

The separation stress of 18 MPa for single-pass scribing is comparable to that of samples scribed at 158 mm/s with filaments formed using MHz bursts with picosecond pulses and samples scribed at 225 mm/s using Bessel beam with sub-ns pulses [135,221]. The minimal separation stress of ~12 MPa achieved with double-pass scribing is similar to the separation of 1 mm-thick SLG samples scribed with a Bessel beam at 48 mm/s using picosecond

pulses [134]. Even smaller separation stress of 4 MPa was demonstrated for 1 mm-thick SLG samples scribed at 100 mm/s with Bessel beams when using sub-ns pulses with ~mJ energy [110]. However, the Bessel beam allows modifications to be formed throughout the entire thickness of the sample. In this work, the longest modification zone covered 83% of the sample thickness, limiting the minimal theoretical separation stress to 2.3 MPa (calculated with the sub-critical crack growth model).

The sidewall roughness R_a of ~2 µm is comparable to that of a study investigating filament-based scribing using high average power lasers with MHz bursts [6]. However, R_a values as low as a few hundred nanometers can be achieved, as demonstrated with samples scribed using Bessel beam and MHz bursts [138,222].

5.3. Comparison of different glass cutting methods

The filament scribing and BUC results achieved in this work (Sections 5 and 3) at the optimal parameters are compared to different glass cutting methods in Figure 52. Here, the scribing speed is referred to as the cutting speed. The slowest cutting methods are the disk and wire sawing, followed by laser subtractive (TDC, WATDC, and BUC) and waterjet cutting techniques (Figure 52(a)). The mechanical and laser-based glass scribing allows for the fastest sample separation. The glass scribing speed of 6 m/s achieved in this study is the highest compared to all other methods. For comparison, filament-scribing has been shown to reach 1.2 m/s for 3.8 mm-thick glass using high average power laser sources [6]. The mechanical scribing was shown to reach 2 m/s for 8 mm-thick glass samples, corresponding to a relative cutting speed of 160 cm²/s [4]. The relative cutting speed of 66 cm²/s demonstrated in this work is the second highest reported, with only a few laser scribing studies showing similar values of 46 and 48 cm²/s [6,88] (Figure 52(b)).

The cutting efficiency parameters are compared only for the laser-based techniques (Figure 52(c, d)). For all methods, cutting efficiency decreases with increasing thickness (Figure 52(c)). Nevertheless, the relative cutting efficiency mitigates this issue, yielding comparable results when processing samples of varying thicknesses with the same cutting method. The most efficient method is laser scribing, followed by controlled fracture, and the least efficient method is subtractive cutting. The linear and relative cutting efficiencies (300 mm/J and 330 mm²/J) achieved in this study are the highest compared to other methods.

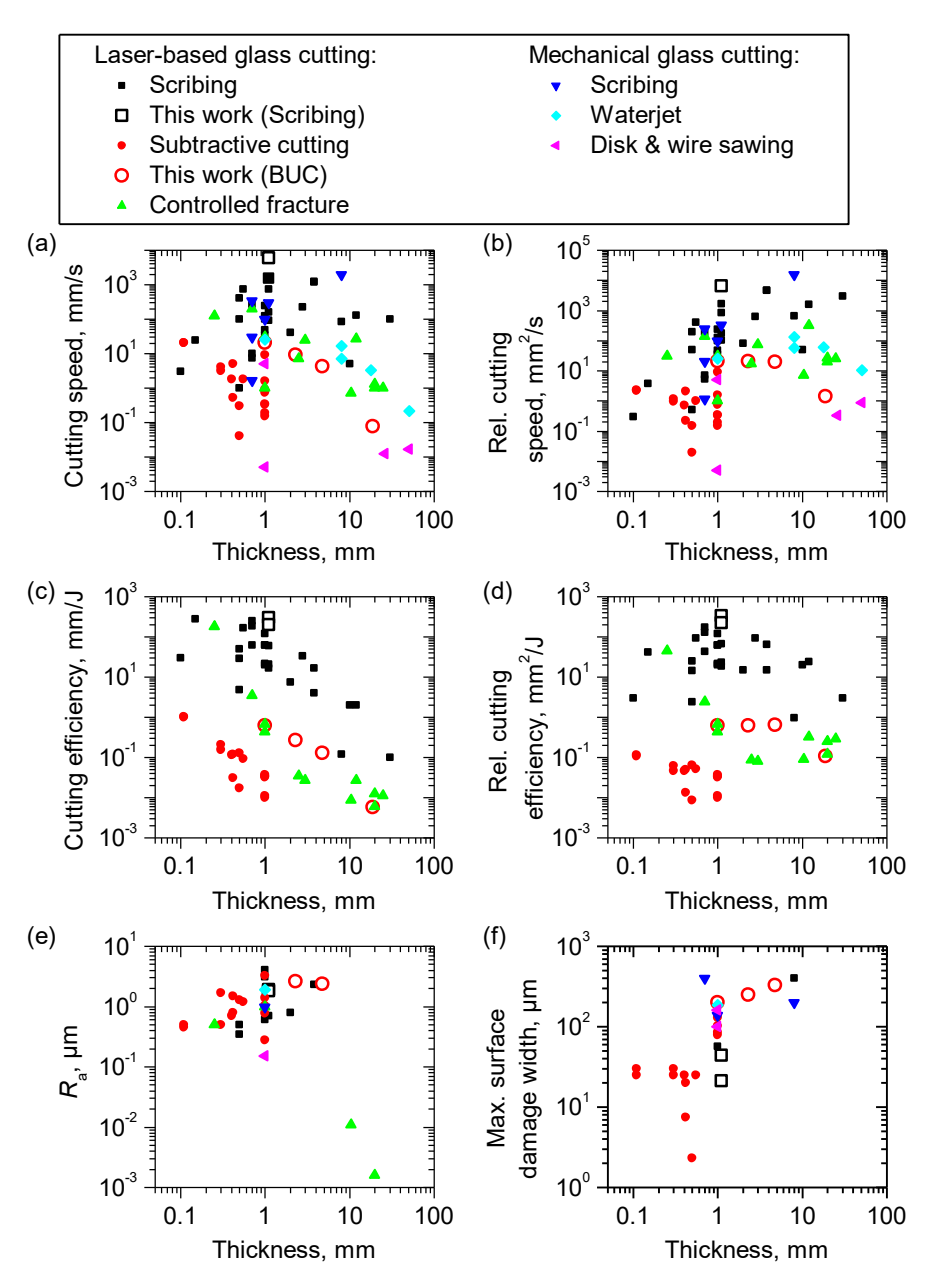


Figure 52. Comparison of glass cutting studies. Cutting speed (a) and efficiency (c), relative cutting speed (b) and efficiency (d), average sidewall surface roughness (e), and the largest surface damage width on either the front or bottom surface (f) are shown as dependencies on sample thickness. The methods include laser-scribing (using Bessel beams [81,87,88,110,123,124,127,134,135,138,219,222–225]) or filaments [6,12,77,221,226,227]), subtractive cutting (combination of TDC [5,144,159,160], WATDC [5,141,144,158,160,168,228], and BUC [5,110]), controlled fracture [30,91,232,113–116,138,229–231], mechanical scribing [4,95,96,110,233,234], disk [99,110] and wire [101,235] sawing, and waterjet [99,104,109,110,236,237] cutting.

The quality of the cut is assessed by comparing the sidewall roughness R_a and the maximum width of surface chippings (Figure 52(e, f)). There are significantly fewer data points, as half of the studies have not assessed the quality of the samples using the aforementioned parameters. However, it can be seen that the highest sidewall surface quality is achieved with a controlled fracture method, as it results in a mirror-like surface with R_a of a few nm. Laser subtractive cutting, scribing, and mechanical sawing methods enable achieving a R_a of 1 μ m or lower. However, different experimental setups and parameter sets result in R_a ranging from 0.3 μ m to 5 μ m.

The largest chippings of a few hundred μm are formed using the mechanical scribe and break method. Similar chippings were formed in this work using BUC with GHz bursts. Significantly smaller chippings of ~20 μm were formed in this study using the filament-scribing. However, the smallest surface chippings of a few μm are achieved using laser subtractive methods.

5.4. Summary

Stable separation of 1.1 mm-thick SLG samples scribed at up to 10 m/s speed was accomplished by forming modifications via filamentation with a BiBurst regime of P10N5, burst repetition rate of 100 kHz, and NA of 0.04. The transverse modifications were aligned along the scribing line by setting the linear polarization perpendicular to it.

The surface quality was examined for samples scribed with a single-pass, with the beam focused to the bottom, and the separation achieved by applying tension to the bottom surface. The mean maximum chipping length on the front surface was up to 60 μm for all the tested parameters, with no visible tendency. However, different chipping values were achieved for the bottom surface. Shorter pulse durations of 176 fs and 1 ps resulted in $\sim\!\!30~\mu m$ chippings for scanning speeds of 4–10 m/s and a burst energy of 300 μJ . Longer pulse durations of 2–4 ps resulted in $\sim\!\!100~\mu m$ chippings. Furthermore, a lower burst energy of 200 μJ resulted in larger chippings.

The sample sidewalls consisted of mirror-like and modified zones with roughness (R_a) and waviness (W_a) of up to 3.4 µm for scanning speeds of 6–10 m/s using burst energy of 300 µJ. Lower scanning speeds of 4–5 m/s resulted in the formation of inclined modifications and significantly worse sidewall quality.

The experiments revealed that the lowest separation stress is achieved by forming the longest modified zone, which reaches the tensioned surface. Higher separation stress was achieved when tensioning the top surface compared to the bottom surface, as modifications did not reach the top surface

due to a certain distance needed for the Kerr effect to build up. The lowest separation stress was accomplished by focusing the beam to the bottom surface. Lowering the focus resulted in a shorter modified zone, while raising the focus prevented the modifications from reaching the bottom surface.

Stable separation of single-pass scribed samples with a 4–10 m/s speed was accomplished. The lowest separation stress of 18 MPa for single-pass scribing was achieved at $v_{\rm scan}=6$ m/s, $\tau_{\rm p}=176$ fs, and $E_{\rm B}=300$ $\mu{\rm J}$. Lower burst energy of 200 $\mu{\rm J}$ resulted in a 1.5 times higher separation stress. The double-pass scribing increased the modified zone length and reduced the separation stress to ~12 MPa at the expense of twice slower scribing. For double-pass scribing, both 200 and 300 $\mu{\rm J}$ burst energies led to similar separation stress and surface chippings. However, a lower burst energy of 200 $\mu{\rm J}$ resulted in better sidewall quality with $R_{\rm a}=2$ $\mu{\rm m}$ of the modified zone and $W_{\rm a}=1.2$ $\mu{\rm m}$ of the mirror zone.

The separation stress of the scribed samples was compared to the simulations based on inert and sub-critical crack growth models. The experimental data confirm the theoretical trend, as separation stress decreased with longer modified zones. The experimental points differed from the inert model by up to 25% for the modified zone lengths of up to 0.6 mm (around half the sample thickness). The difference between the experimental data and the model increased for longer modified zones.

Compared to other works, our study demonstrated the highest cutting speed, linear and relative cutting efficiencies, and the second-best relative cutting speed for glass cutting.

MAIN RESULTS AND CONCLUSION

The first statement to be defended is based on these results:

- 1. Fast (4.2 mm/s) and efficient (0.13 mm/J) cutting of 4.8 mm-thick soda-lime glass (SLG) samples was achieved using 1030 nm wavelength GHz bursts of picosecond pulses as the material was removed via fracturing.
- 2. High-speed cutting regime comes with an inferior cutting quality. The average sidewall roughness (R_a) was 2.3 μ m, and the average maximum length of chippings on the bottom and top surfaces was 90 μ m and 400 μ m, respectively.
- 3. High-quality ablation and high-speed coarse machining regimes were applied to the same SLG workpiece by changing the process parameters. The high-throughput regime, achieved with a high number of pulses per burst, allowed a fast cutting of a sample, while the 300 μm-wide chamfers produced with the high-quality regime, achieved with fewer pulses per burst, eliminated chippings generated during the cutting process.

The second statement to be defended is based on these results:

- 4. The burst and BiBurst regimes allowed forming elongated modifications with transverse dimensions inside fused silica (FS) and SLG when employing low NA ~0.04 and femtosecond pulses, whereas no modification was observed with the single-pulse regime.
- 5. In both FS and SLG, higher burst energy increased the transverse and longitudinal lengths, except in cases where it led to front surface damage. The longitudinal lengths reached 1.4 mm for FS and 0.9 mm for SLG, while transverse lengths were up to 46 μ m for FS and 114 μ m for SLG.
- 6. At the Z positions where the transverse modifications were the longest, the transverse angle relied on linear polarization or beam ellipticity, depending on the intra-burst energy. For low intra-burst energies, the modifications formed parallelly (for FS) or perpendicularly (for SLG)

to polarization. Increasing the intra-burst energy caused modifications to rotate towards the beam ellipticity. The exception is the modifications formed in FS with MHz burst, as they started rotating towards the polarization for MHz burst when the intra-burst energy increased beyond $10~\mu J$.

7. In FS, the transverse angle of modifications formed using the P1N10 and P10N1 regimes varied along the Z axis at higher burst energies, aligning along the beam ellipticity at the front and along the polarization at the bottom of the modification. In contrast, under polarization-controlled conditions or when the polarization was aligned along the beam, the transverse angle remained constant along the Z axis.

The third statement to be defended is based on these results:

8. Stable separation of 1.1 mm-thick SLG samples scribed at 4–10 m/s speed was accomplished by forming modifications via filamentation with a BiBurst regime of P10N5, burst repetition rate of 100 kHz, and NA of 0.04. To the best of our knowledge, we demonstrated the fastest glass scribing recorded to date. To achieve this, the transverse modifications were aligned along the scribing line by setting the linear polarization perpendicular to it.

Main conclusion:

9. Ultrashort pulsed lasers operating in GHz burst mode offer exceptional flexibility for bottom-up cutting (BUC) of glass, as the number of pulses per burst affects cutting efficiency, throughput, and quality. The GHz burst mode enables dynamic adjustment of the number of pulses per burst during a single processing operation, enabling "quality" or "throughput" modes for different regions of the workpiece. Additionally, the same laser can be used to form polarization-controlled filament-induced modifications, which are suitable for scribing, achieving speeds of up to 10 m/s in 1.1 mm-thick glass. Demonstrating both BUC and filamentation scribing with a single laser setup highlights the unique flexibility of ultrashort GHz burst mode lasers for multiple advanced glass processing applications.

REFERENCES

- 1. E. Axinte, "Glasses as engineering materials: A review," Mater. Des. **32**(4), 1717–1732 (2011).
- 2. A. M. Kovalchenko, "Studies of the ductile mode of cutting brittle materials (A review)," J. Superhard Mater. **35**(5), 259–276 (2013).
- 3. A. Perveen and C. Molardi, "Machining of Glass Materials: An Overview," in (2017), pp. 23–47.
- 4. S. Müller-Braun, M. Seel, M. König, P. Hof, J. Schneider, and M. Oechsner, "Cut edge of annealed float glass: crack system and possibilities to increase the edge strength by adjusting the cutting process," Glas. Struct. Eng. 5(1), 3–25 (2020).
- 5. J. Dudutis, L. Zubauskas, E. Daknys, E. Markauskas, R. Gvozdaitė, G. Račiukaitis, and P. Gečys, "Quality and flexural strength of laser-cut glass: classical top-down ablation versus water-assisted and bottom-up machining," Opt. Express **30**(3), 4564 (2022).
- 6. T. Dietz, M. Jenne, D. Bauer, M. Scharun, D. Sutter, and A. Killi, "Ultrafast thin-disk multi-pass amplifier system providing 1.9 kW of average output power and pulse energies in the 10 mJ range at 1 ps of pulse duration for glass-cleaving applications," Opt. Express 28(8), 11415 (2020).
- 7. C. Kerse, H. Kalaycıoğlu, P. Elahi, B. Çetin, D. K. Kesim, Ö. Akçaalan, S. Yavaş, M. D. Aşık, B. Öktem, H. Hoogland, R. Holzwarth, and F. Ö. Ilday, "Ablation-cooled material removal with ultrafast bursts of pulses," Nature **537**(7618), 84–88 (2016).
- 8. A. Žemaitis, M. Gaidys, P. Gečys, M. Barkauskas, and M. Gedvilas, "Femtosecond laser ablation by bibursts in the MHz and GHz pulse repetition rates," Opt. Express **29**(5), 7641 (2021).
- 9. G. Bonamis, E. Audouard, C. Hönninger, J. Lopez, K. Mishchik, E. Mottay, and I. Manek-Hönninger, "Systematic study of laser ablation with GHz bursts of femtosecond pulses," Opt. Express **28**(19), 27702 (2020).
- 10. B. Neuenschwander, B. Jaeggi, D. J. Foerster, T. Kramer, and S. Remund, "Influence of the burst mode onto the specific removal rate for metals and semiconductors," J. Laser Appl. **31**(2), 022203 (2019).
- 11. E. Kažukauskas, S. Butkus, P. Tokarski, V. Jukna, M. Barkauskas, and V. Sirutkaitis, "Micromachining of Transparent Biocompatible Polymers Applied in Medicine Using Bursts of Femtosecond Laser Pulses," Micromachines 11(12), 1093 (2020).
- 12. B. Stępak, N. Grudzień, K. Kowalska, Y. Stepanenko, and M. Nejbauer, "High-speed cleaving of glass and polymers using ultrafast fiber laser," J. Laser Appl. **35**(1), (2023).
- 13. D. Metzner, P. Lickschat, C. Kreisel, T. Lampke, and S. Weißmantel, "Study on laser ablation of glass using MHz-to-GHz burst pulses," Appl. Phys. A **128**(8), 637 (2022).

- 14. P. Balage, M. Lafargue, T. Guilberteau, G. Bonamis, C. Hönninger, J. Lopez, and I. Manek-Hönninger, "Comparative Study of Percussion Drilling in Glasses with a Femtosecond Laser in Single Pulse, MHz-Burst, and GHz-Burst Regimes and Optimization of the Hole Aspect Ratio," Micromachines **14**(9), 1754 (2023).
- 15. T. G. Mayerhöfer, S. Pahlow, and J. Popp, "The Bouguer-Beer-Lambert Law: Shining Light on the Obscure," Chemphyschem **21**(18), 2029–2046 (2020).
- 16. M. Wollenhaupt, L. Englert, A. Horn, and T. Baumert, "Control of ionization processes in high band gap materials," J. Laser Micro Nanoeng. **4**(3), 144–151 (2009).
- 17. D. Tan, K. N. Sharafudeen, Y. Yue, and J. Qiu, "Femtosecond laser induced phenomena in transparent solid materials: Fundamentals and applications," Prog. Mater. Sci. **76**(September 2015), 154–228 (2016).
- 18. A. Dubietis, *Netiesinė Optika: Vilniaus Universiteto Vadovėlis* (Vilniaus universitetas, 2011).
- 19. M. V. Shugaev, C. Wu, O. Armbruster, A. Naghilou, N. Brouwer, D. S. Ivanov, T. J. Y. Derrien, N. M. Bulgakova, W. Kautek, B. Rethfeld, and L. V. Zhigilei, "Fundamentals of ultrafast laser-material interaction," MRS Bull. **41**(12), 960–968 (2016).
- 20. A. M. Zheltikov, "Keldysh parameter, photoionization adiabaticity, and the tunneling time," Phys. Rev. A **94**(4), 1–6 (2016).
- 21. G. D. Tsibidis and E. Stratakis, "Ionization dynamics and damage conditions in fused silica irradiated with mid-infrared femtosecond pulses," Appl. Phys. Lett. **122**(4), (2023).
- 22. S. S. Mao, F. Quéré, S. Guizard, X. Mao, R. E. Russo, G. Petite, and P. Martin, "Dynamics of femtosecond laser interactions with dielectrics," Appl. Phys. A Mater. Sci. Process. **79**(7), 1695–1709 (2004).
- 23. S. C. Jones, P. Braunlich, R. T. Casper, X.-A. Shen, and P. Kelly, "Recent Progress On Laser-Induced Modifications And Intrinsic Bulk Damage Of Wide-Gap Optical Materials," Opt. Eng. **28**(10), (1989).
- 24. A. Kaiser and B. Rethfeld, "Microscopic processes in dielectrics under irradiation by subpicosecond laser pulses," Phys. Rev. B Condens. Matter Mater. Phys. **61**(17), 11437–11450 (2000).
- 25. B. Rethfeld, "Free-electron generation in laser-irradiated dielectrics," Phys. Rev. B Condens. Matter Mater. Phys. **73**(3), 1–6 (2006).
- 26. B. Rethfeld, D. S. Ivanov, M. E. Garcia, and S. I. Anisimov, "Modelling ultrafast laser ablation," J. Phys. D Appl. Phys. **50**(19), (2017).
- 27. R. Osellame, G. Cerullo, and R. Ramponi, "Femtosecond Laser Micromachining: Photonic and Microfluidic Devices in Transparent Materials," Top. Appl. Phys. **123**, 3–18 (2012).
- 28. X. Liu, D. Du, and G. Mourou, "Laser ablation and micromachining with ultrashort laser pulses," IEEE J. Quantum Electron. **33**(10), 1706–

- 1716 (1997).
- 29. D. Nieto, J. Arines, G. M. O'Connor, and M. T. Flores-Arias, "Single-pulse laser ablation threshold of borosilicate, fused silica, sapphire, and soda-lime glass for pulse widths of 500 fs, 10 ps, 20 ns," Appl. Opt. 54(29), 8596 (2015).
- 30. J. Wei, J. Yang, D. Zhang, X. Pan, Z. Yi, L. Shui, M. Jin, R. Che, and Y. Liu, "Adjustable multifocus laser separation scheme for thick glass with flexibly controllable thermal stress distribution," J. Laser Appl. 34(1), 012028 (2022).
- 31. P. Gečys, J. Dudutis, and G. Račiukaitis, "Nanosecond Laser Processing of Soda-Lime Glass," J. Laser Micro/Nanoengineering **10**(3), 254–258 (2015).
- 32. A. Salleo, T. Sands, and F. Y. Génin, "Machining of transparent materials using an IR and UV nanosecond pulsed laser," Appl. Phys. A Mater. Sci. Process. **71**(6), 601–608 (2000).
- 33. Y. Li and S. Qu, "Water-assisted femtosecond laser ablation for fabricating three-dimensional microfluidic chips," Curr. Appl. Phys. 13(7), 1292–1295 (2013).
- 34. L. Zubauskas, E. Markauskas, A. Vyšniauskas, V. Stankevič, and P. Gečys, "Comparative analysis of microlens array formation in fused silica glass by laser: Femtosecond versus picosecond pulses," J. Sci. Adv. Mater. Devices 9(4), (2024).
- 35. B. C. Stuart, M. D. Feit, A. M. Rubenchik, B. W. Shore, and M. D. Perry, "Laser-induced damage in dielectrics with nanosecond to subpicosecond pulses," Phys. Rev. Lett. **74**(12), 2248–2251 (1995).
- 36. G. Ren, H. Sun, T. Koike, K. Takabayashi, K. Nakagawa, N. Sugita, and Y. Ito, "Ultrafast machining through heating laser-excited electrons," Ultrafast Sci. 1–10 (2025).
- 37. "Refractive index database," https://refractiveindex.info/?shelf=glass&book=soda-lime&page=Rubin-clear, accessed 08/21/2025.
- 38. M. Haldimann, A. Luible, and M. Overend, *Structural Use of Glass* (International Association for Bridge and Structural Engineering, 2008).
- 39. "Refractive index database," https://refractiveindex.info/?shelf=glass&book=fused silica&page=Malitson, accessed 08/21/2025.
- 40. P. Kabaciński, T. M. Kardaś, Y. Stepanenko, and C. Radzewicz, "Nonlinear refractive index measurement by SPM-induced phase regression," Opt. Express 27(8), 11018 (2019).
- 41. A. Shehata, M. Ali, R. Schuch, and T. Mohamed, "Experimental investigations of nonlinear optical properties of soda-lime glasses and theoretical study of self-compression of fs laser pulses," Opt. Laser Technol. **116**(December 2018), 276–283 (2019).
- 42. "Fused Silica Glass (SiO2)," https://www.crystran.com/optical-materials/fused-silica-sio2, accessed 08/21/2025.
- 43. J. Bonse, T. Seuthe, M. Grehn, M. Eberstein, A. Rosenfeld, and A.

- Mermillod-Blondin, "Time-resolved microscopy of fs-laser-induced heat flows in glasses," Appl. Phys. A Mater. Sci. Process. **124**(1), 0 (2018).
- 44. M. L. Baesso, J. Shen, and R. D. Snook, "Time-resolved thermal lens measurement of thermal diffusivity of soda—lime glass," Chem. Phys. Lett. **197**(3), 255–258 (1992).
- 45. A. Braun, G. Korn, X. Liu, D. Du, J. Squier, and G. Mourou, "Self-channeling of high-peak-power femtosecond laser pulses in air," Opt. Lett. **20**(1), 73 (1995).
- 46. A. Couairon and A. Mysyrowicz, "Femtosecond filamentation in transparent media," Phys. Rep. **441**(2–4), 47–189 (2007).
- 47. T. Olivier, F. Billard, and H. Akhouayri, "Nanosecond Z-scan measurements of the nonlinear refractive index of fused silica," Opt. Express 12(7), 1377 (2004).
- 48. D. N. Schimpf, T. Eidam, E. Seise, S. Hädrich, J. Limpert, and A. Tünnermann, "Circular versus linear polarization in laser-amplifiers with Kerr-nonlinearity," Opt. Express 17(21), 18774 (2009).
- 49. X. Lu, Q. Liu, Z. Liu, S. Sun, P. Ding, B. Ding, and B. Hu, "Measurement of nonlinear refractive index coefficient using emission spectrum of filament induced by gigawatt-femtosecond pulse in BK7 glass," Appl. Opt. **51**(12), 2045–2050 (2012).
- 50. S. Onda, W. Watanabe, K. Yamada, K. Itoh, and J. Nishii, "Study of filamentary damage in synthesized silica induced by chirped femtosecond laser pulses," J. Opt. Soc. Am. B **22**(11), 2437 (2005).
- 51. C. Ma and W. Lin, "Normal dispersion effects on the nonlinear focus," J. Opt. Soc. Am. B **33**(6), 1055 (2016).
- 52. V. Jukna, "Conical wave triggered transient spatio-temporal effects in kerr media," Vilniaus universitetas (2012).
- 53. F. Théberge, W. Liu, P. T. Simard, A. Becker, and S. L. Chin, "Plasma density inside a femtosecond laser filament in air: Strong dependence on external focusing," Phys. Rev. E Stat. Nonlinear, Soft Matter Phys. 74(3), 1–7 (2006).
- 54. Y. P. Deng, J. B. Zhu, Z. G. Ji, J. S. Liu, B. Shuai, R. X. Li, Z. Z. Xu, F. Théberge, and S. L. Chin, "Transverse evolution of a plasma channel in air induced by a femtosecond laser," Opt. Lett. **31**(4), 546 (2006).
- 55. A. Couairon, L. Sudrie, M. Franco, B. Prade, and A. Mysyrowicz, "Filamentation and damage in fused silica induced by tightly focused femtosecond laser pulses," Phys. Rev. B Condens. Matter Mater. Phys. **71**(12), 1–11 (2005).
- 56. E. Yablonovitch and N. Bloembergen, "Avalanche ionization and the limiting diameter of filaments induced by light pulses in transparent media," Phys. Rev. Lett. **29**(14), 907–910 (1972).
- 57. S. Juodkazis, V. Mizeikis, E. Gaižauskas, E. Vanagas, V. Jarutis, and H. Misawa, "Studies of femtosecond pulse filamentation in glasses," Proc SPIE **6053**, 60530R-60530R-8 (2006).

- 58. A. Couairon, "Filamentation length of powerful laser pulses," Appl. Phys. B Lasers Opt. **76**(7), 789–792 (2003).
- S. Tzortzakis, L. Sudrie, M. Franco, B. Prade, A. Mysyrowicz, A. Couairon, and L. Bergé, "Self-guided propagation of ultrashort ir laser pulses in fused silica," Phys. Rev. Lett. 87(21), 213902-1-213902-4 (2001).
- 60. S. L. Chin, S. A. Hosseini, W. Liu, Q. Luo, F. Théberge, N. Aközbek, A. Becker, V. P. Kandidov, O. G. Kosareva, and H. Schroeder, "The propagation of powerful femtosecond laser pulses in optical media: Physics, applications, and new challenges," Can. J. Phys. **83**(9), 863–905 (2005).
- 61. S. Xu, J. Bernhardt, M. Sharifi, W. Liu, and S. L. Chin, "Intensity clamping during laser filamentation by TW level femtosecond laser in air and argon," Laser Phys. **22**(1), 195–202 (2012).
- 62. G. Fibich and B. Ilan, "Deterministic vectorial effects lead to multiple filamentation," Opt. Lett. **26**(11), 840 (2001).
- 63. G. Fibich and B. Ilan, "Multiple Filamentation of Circularly Polarized Beams," Phys. Rev. Lett. **89**(1), 1–4 (2002).
- 64. A. S. Arabanian and R. Massudi, "Study on effect of polarization and frequency chirp of incident pulse on femtosecond-laser-induced modification inside silica glass," J. Opt. Soc. Am. B **31**(4), 748 (2014).
- 65. G. Fibich and B. Ilan, *Vectorial and Random Effects in Self-Focusing and in Multiple Filamentation* (2001), **157**(1–2).
- 66. A. Dubietis, G. Tamošauskas, G. Fibich, and B. Ilan, "Multiple filamentation induced by input-beam ellipticity," Opt. Lett. **29**(10), 1126 (2004).
- 67. D. Majus, V. Jukna, G. Valiulis, and A. Dubietis, "Generation of periodic filament arrays by self-focusing of highly elliptical ultrashort," Phys. Rev. A **79**(033843), 1–6 (2009).
- 68. O. G. Kosareva, T. Nguyen, N. A. Panov, W. Liu, A. Saliminia, V. P. Kandidov, N. Akozbek, M. Scalora, R. Vallee, and S. L. Chin, "Array of femtosecond plasma channels in fused silica," Opt. Commun. **267**(2), 511–523 (2006).
- 69. Z. Hao, K. Stelmaszczyk, P. Rohwetter, W. M. Nakaema, and L. Woeste, "Femtosecond laser filament-fringes in fused silica," Opt. Express **19**(8), 7799 (2011).
- 70. A. Camino, Z. Hao, X. Liu, and J. Lin, "Control of laser filamentation in fused silica by a periodic microlens array," Opt. Express **21**(7), 7908 (2013).
- 71. C. Corsi, A. Tortora, and M. Bellini, "Generation of a variable linear array of phase-coherent supercontinuum sources," Appl. Phys. B Lasers Opt. **78**(3–4), 299–304 (2004).
- 72. W. Liu, S. Petit, A. Becker, N. Aközbek, C. M. Bowden, and S. L. Chin, "Intensity clamping of a femtosecond laser pulse in condensed matter," Opt. Commun. **202**(1–3), 189–197 (2002).

- 73. S. Xu, X. Sun, B. Zeng, W. Chu, J. Zhao, W. Liu, Y. Cheng, Z. Xu, and S. L. Chin, "Simple method of measuring laser peak intensity inside femtosecond laser filament in air," Opt. Express **20**(1), 299 (2012).
- 74. J. B. Ashcom, R. R. Gattass, C. B. Schaffer, and E. Mazur, "Numerical aperture dependence of damage and supercontinuum generation from femtosecond laser pulses in bulk fused silica," JOSA B **23**(11), 2317–2322 (2006).
- 75. S. Tzortzakis, D. G. Papazoglou, and I. Zergioti, "Long-range filamentary propagation of subpicosecond ultraviolet laser pulses in fused silica," Opt. Lett. **31**(6), 796 (2006).
- S. Butkus, E. Gaižauskas, D. Paipulas, Ž. Viburys, D. Kaškelyė, M. Barkauskas, A. Alesenkov, and V. Sirutkaitis, "Rapid microfabrication of transparent materials using filamented femtosecond laser pulses," Appl. Phys. A 114(1), 81–90 (2014).
- 77. M. S. Ahsan, I. Sohn, and H. Choi, "Gorilla Glass Cutting Using Femtosecond Laser Pulse Filaments," Appl. Sci. **14**(1), 312 (2023).
- 78. L. Sudrie, A. Couairon, M. Franco, B. Lamouroux, B. Prade, S. Tzortzakis, and A. Mysyrowicz, "Femtosecond Laser-Induced Damage and Filamentary Propagation in Fused Silica," Phys. Rev. Lett. **89**(18), 1–4 (2002).
- 79. Q. Sun, H. Asahi, Y. Nishijima, N. Murazawa, K. Ueno, and H. Misawa, "Pulse duration dependent nonlinear propagation of a focused femtosecond laser pulse in fused silica," Opt. Express **18**(24), 24495 (2010).
- 80. M. K. Bhuyan, F. Courvoisier, P. A. Lacourt, M. Jacquot, R. Salut, L. Furfaro, and J. M. Dudley, "High aspect ratio nanochannel machining using single shot femtosecond Bessel beams," Appl. Phys. Lett. **97**(8), 1–4 (2010).
- 81. K. Mishchik, M. Delaigue, C. Hönninger, and E. Mottay, "Advanced spatial and temporal shaping for glass cutting application," Proc. Conf. Lasers Manuf. 1–5 (2019).
- 82. S. N. Khonina, N. L. Kazanskiy, P. A. Khorin, and M. A. Butt, "Modern types of axicons: New functions and applications," Sensors **21**(19), (2021).
- 83. F. Courvoisier, J. Zhang, M. K. Bhuyan, M. Jacquot, and J. M. Dudley, "Applications of femtosecond Bessel beams to laser ablation," Appl. Phys. A Mater. Sci. Process. **112**(1), 29–34 (2013).
- 84. J. Durnin, J. Miceli, and J. H. Eberly, "Diffraction-free beams," Phys. Rev. Lett. **58**(15), 1499–1501 (1987).
- 85. M. K. Bhuyan, F. Courvoisier, H. S. Phing, O. Jedrkiewicz, S. Recchia, P. Di Trapani, and J. M. Dudley, "Laser micro- and nanostructuring using femtosecond Bessel beams," Eur. Phys. J. Spec. Top. **199**(1), 101–110 (2011).
- 86. L. Froehly, M. Jacquot, P. A. Lacourt, J. M. Dudley, and F.

- Courvoisier, "Spatiotemporal structure of femtosecond Bessel beams from spatial light modulators," J. Opt. Soc. Am. **31**(4), 790 (2014).
- 87. M. Jenne, D. Flamm, T. Ouaj, J. Hellstern, J. Kleiner, D. Grossmann, M. Koschig, M. Kaiser, M. Kumkar, and S. Nolte, "High-quality tailored-edge cleaving using aberration-corrected Bessel-like beams," Opt. Lett. **43**(13), 3164 (2018).
- 88. M. Jenne, D. Flamm, K. Chen, M. Schäfer, M. Kumkar, and S. Nolte, "Facilitated glass separation by asymmetric Bessel-like beams," Opt. Express **28**(5), 6552 (2020).
- 89. J. Dudutis, P. Gečys, and G. Račiukaitis, "Non-ideal axicon-generated Bessel beam application for intra-volume glass modification," Opt. Express **24**(25), 28433 (2016).
- 90. H. D. Nguyen, X. Sedao, C. Mauclair, G. Bidron, N. Faure, E. Moreno, J. P. Colombier, and R. Stoian, "Non-diffractive bessel beams for ultrafast laser scanning platform and proof-of-concept side-wall polishing of additively manufactured parts," Micromachines 11(11), (2020).
- 91. J. Lopez, K. Mishchik, B. Chassagne, C. Javaux-Leger, C. Hönninger, E. Mottay, and R. Kling, "Glass cutting using ultrashort pulsed bessel beams," J. Laser Appl. **60**(2015), 60–69 (2018).
- 92. Z. Bouchal, J. Wagner, and M. Chlup, "Self-reconstruction of a distorted nondiffracting beam," Opt. Commun. **151**(4–6), 207–211 (1998).
- 93. C. H. Tsai and B. W. Huang, "Diamond scribing and laser breaking for LCD glass substrates," J. Mater. Process. Technol. **198**(1–3), 350–358 (2008).
- 94. Y. S. Liao, G. M. Yang, and Y. S. Hsu, "Vibration assisted scribing process on LCD glass substrate," Int. J. Mach. Tools Manuf. **50**(6), 532–537 (2010).
- 95. C. T. Pan, C. C. Hsieh, C. Y. Su, and Z. S. Liu, "Study of cutting quality for TFT-LCD glass substrate," Int. J. Adv. Manuf. Technol. **39**(11–12), 1071–1079 (2008).
- 96. T. Ono, "Effect of Scribing Wheel Dimensions on the Cutting of LCD Glass Substrate," SID Symp. Dig. Tech. Pap. **31**(1), 156–159 (2000).
- 97. M. I. Smirnov, Y. A. Spiridonov, and A. R. Karapetyan, "Modern sheet-glass cutting technologies," Glas. Ceram. **68**(1–2), 6–10 (2011).
- 98. J. Liu, R. Han, L. Zhang, and H. Guo, "Study on lubricating characteristic and tool wear with water vapor as coolant and lubricant in green cutting," Wear **262**(3–4), 442–452 (2007).
- 99. J. Salinas-Luna, R. Machorro, J. Camacho, E. Luna, and J. Nunez, "Water jet: A promising method for cutting optical glass," Appl. Opt. **45**(15), 3477–3481 (2006).
- 100. W. I. Clark, A. J. Shih, C. W. Hardin, R. L. Lemaster, and S. B. McSpadden, "Fixed abrasive diamond wire machining Part I: Process monitoring and wire tension force," Int. J. Mach. Tools Manuf. 43(5),

- 523-532 (2003).
- 101. S. Li, J. Wang, B. An, A. Tang, and R. G. Landers, "Wire saw cutting force modeling and control using wire SAW velocity," Proc. 2018 ISFA 2018 Int. Symp. Flex. Autom. 15–19 (2018).
- 102. P. Liu, L. Deng, J. Duan, B. Wu, X. Zeng, Y. Shangguan, and X. Wang, "A study on laser multi-focus separation technology of thick KDP crystal," Int. J. Mach. Tools Manuf. 118–119(January), 26–36 (2017).
- 103. M. Sutowska, C. Łukianowicz, and M. Szada-Borzyszkowska, "Sequential Smoothing Treatment of Glass Workpieces Cut by Abrasive Water Jet," Materials (Basel). **15**(19), (2022).
- 104. U. Aich, S. Banerjee, A. Bandyopadhyay, and P. K. Das, "Abrasive Water Jet Cutting of Borosilicate Glass," Procedia Mater. Sci. 6(Icmpc), 775–785 (2014).
- 105. S. Nisar, L. Li, and M. A. Sheikh, "Laser glass cutting techniques—A review," J. Laser Appl. **25**(4), 042010 (2013).
- 106. "Everything You Wanted to Know About Cutting Glass with Diamond Blades," https://ukam.com/everything-you-wanted-to-know-about-cutting-glass-with-diamond-blades, accessed 07/22/2025.
- 107. Y. Yin, Y. Gao, and C. Yang, "Sawing characteristics of diamond wire cutting sapphire crystal based on tool life cycle," Ceram. Int. **47**(19), 26627–26634 (2021).
- 108. "Water Jet Cutting: Types, Uses and Processes," https://www.iqsdirectory.com/articles/water-jet-cutting.html, accessed 07/22/2025.
- 109. F. Yuan, J. A. Johnson, D. D. Allred, and R. H. Todd, "Waterjet cutting of cross-linked glass," J. Vac. Sci. Technol. A Vacuum, Surfaces, Film. **13**(1), 136–139 (1995).
- 110. J. Dudutis, J. Pipiras, R. Stonys, E. Daknys, A. Kilikevičius, A. Kasparaitis, G. Račiukaitis, and P. Gečys, "In-depth comparison of conventional glass cutting technologies with laser-based methods by volumetric scribing using Bessel beam and rear-side machining," Opt. Express **28**(21), 32133 (2020).
- 111. T. L. Anderson, *Fracture Mechanics: Fundamentals and Applications*, 3rd ed. (CRC Press, 2005).
- 112. C. H. Tsai and C. S. Liou, "Fracture mechanism of laser cutting with controlled fracture," J Manuf. Sci. Eng **125**(3), 519–528 (2003).
- 113. J. Jiao and X. W. Ã, "Cutting glass substrates with dual-laser beams," Opt. Lasers Eng. J. 47, 860–864 (2009).
- 114. H. K. Tönshoff, A. Ostendorf, C. Kulik, H. Hesener, and O. Haupt, "Final glass products in one processing step by the means of laser radiation," ICALEO 2003 22nd Int. Congr. Appl. Laser Electro-Optics, Congr. Proc. 110, (2003).
- 115. S. Nisar, S. Z. Khan, M. Ali, L. Li, and M. A. Sheikh, "Comparison of Cut Path Deviation Between CO2 and Diode Lasers in Float-Glass Cutting," J. Russ. Laser Res. **35**(2), 182–192 (2014).
- 116. P. Liu, J. Duan, B. Wu, L. Deng, Y. Shangguan, X. Zeng, and X. Wang,

- "A flexible multi-focus laser separation technology for thick glass," Int. J. Mach. Tools Manuf. **135**, 12–23 (2018).
- 117. K. Du and P. Shi, "Subsurface precision processing of glass substrates by innovative lasers," Glas. Sci. Technol. **76**(2), 95–98 (2003).
- 118. K. Venkatakrishnan, N. Sudani, and B. Tan, "A high-repetition-rate femtosecond laser for thin silicon wafer dicing," J. Micromechanics Microengineering **18**(7), (2008).
- 119. J. Shin, "Investigation of the surface morphology in glass scribing with a UV picosecond laser," Opt. Laser Technol. **111**(September 2018), 307–314 (2019).
- 120. C. Y. Seong, H. U. Kim, N. S. Kim, and B. C. Kim, "Comparison of laser glass cutting process using ps and fs lasers," ICALEO 2012 31st Int. Congr. Appl. Lasers Electro-Optics **1289**, 1289–1293 (2012).
- 121. Y. Luo, X. Xie, Z. Zhang, Z. Li, and Y. Huang, "Ultrafast laser composite cutting ultra-thin glass," Opt. Commun. **555**(December 2023), 130224 (2024).
- 122. J. Li, E. Ertorer, and P. R. Herman, "Ultrafast laser burst-train filamentation for non-contact scribing of optical glasses," Opt. Express 27(18), 25078 (2019).
- 123. R. Meyer, L. Froehly, R. Giust, J. Del Hoyo, L. Furfaro, C. Billet, and F. Courvoisier, "Extremely high-aspect-ratio ultrafast Bessel beam generation and stealth dicing of multi-millimeter thick glass," Appl. Phys. Lett. **114**(20), (2019).
- 124. H. Shin and D. Kim, "Strength of ultra-thin glass cut by internal scribing using a femtosecond Bessel beam," Opt. Laser Technol. **129**(December 2019), 106307 (2020).
- 125. A. S. Hosseini and P. R. Herman, "Method of material processing by laser filamentation," U.S. patent US20130126573A1 (2013).
- 126. N. Naseri, G. Dupras, and L. Ramunno, "Mechanism of laser induced filamentation in dielectrics," Opt. Express **28**(18), 26977 (2020).
- 127. J. Dudutis, R. Stonys, G. Račiukaitis, and P. Gečys, "Bessel beam asymmetry control for glass dicing applications," Proc. CIRP **74**, 333–338 (2018).
- 128. Z. Li, X. Wang, J. Wang, O. Allegre, W. Guo, W. Gao, N. Jia, and L. Li, "Stealth dicing of sapphire sheets with low surface roughness, zero kerf width, debris/crack-free and zero taper using a femtosecond Bessel beam," Opt. Laser Technol. **135**(July 2020), 106713 (2021).
- 129. K. Sato, R. Hisamatsu, and K. Akamatsu, "Controller design for high-speed, ultra-precision positioning of a linear motion stage on a vibrating machine base stage control on a vibrating base," Precis. Eng. **80**(November 2022), 10–19 (2023).
- 130. R. Arimoto, C. Saloma, T. Tanaka, and S. Kawata, "Imaging properties of axicon in a scanning optical system," Appl. Opt. **31**(31), 6653 (1992).
- 131. J. Dudutis, R. Stonys, G. Račiukaitis, and P. Gečys, "Generation of

- asymmetrical Bessel-like laser beams for glass dicing," in *Laser Beam Shaping XIX*, A. Dudley and A. V. Laskin, eds. (SPIE, 2019), **1110709**(September), p. 8.
- 132. J. Dudutis, R. Stonys, G. Račiukaitis, and P. Gečys, "Aberration-controlled Bessel beam processing of glass," Opt. Express **26**(3), 3627 (2018).
- 133. D. Flamm, M. Kaiser, M. Feil, M. Kahmann, M. Lang, J. Kleiner, and T. Hesse, "Protecting the Edge: Ultrafast Laser Modified C-shaped Glass Edges," J. Laser Appl. **34**(012014), 1–8 (2022).
- 134. J. Dudutis, M. Mackevičiūtė, J. Pipiras, R. Stonys, V. Stankevič, G. Račiukaitis, and P. Gečys, "Transversal and axial modulation of axicon-generated Bessel beams using amplitude and phase masks for glass processing applications," Opt. Express 30(2), 1860–1874 (2022).
- 135. J. Dudutis, J. Pipiras, S. Schwarz, S. Rung, R. Hellmann, G. Račiukaitis, and P. Gečys, "Laser-fabricated axicons challenging the conventional optics in glass processing applications," Opt. Express 28(4), 5715 (2020).
- 136. M. Lamperti, V. Jukna, O. Jedrkiewicz, P. Di Trapani, R. Stoian, T. E. Itina, C. Xie, F. Courvoisier, and A. Couairon, "Invited Article: Filamentary deposition of laser energy in glasses with Bessel beams," APL Photonics **3**(12), (2018).
- 137. M. K. Bhuyan, P. K. Velpula, J. P. Colombier, T. Olivier, N. Faure, and R. Stoian, "Single-shot high aspect ratio bulk nanostructuring of fused silica using chirp-controlled ultrafast laser Bessel beams," Appl. Phys. Lett. **104**(2), (2014).
- 138. K. Mishchik, R. Beuton, O. Dematteo Caulier, S. Skupin, B. Chimier, G. Duchateau, B. Chassagne, R. Kling, C. Hönninger, E. Mottay, and J. Lopez, "Improved laser glass cutting by spatio-temporal control of energy deposition using bursts of femtosecond pulses," Opt. Express 25(26), 33271 (2017).
- 139. P. Balage, T. Guilberteau, M. Lafargue, G. Bonamis, C. Hönninger, J. Lopez, and I. Manek-Hönninger, "Bessel Beam Dielectrics Cutting with Femtosecond Laser in GHz-Burst Mode," Micromachines **14**(9), 1–15 (2023).
- 140. J. Furmanski, A. M. Rubenchik, M. D. Shirk, and B. C. Stuart, "Deterministic processing of alumina with ultrashort laser pulses," J. Appl. Phys. **102**(7), (2007).
- 141. S. Butkus, E. Gaižauskas, L. Mačernytė, V. Jukna, D. Paipulas, and V. Sirutkaitis, "Femtosecond Beam Transformation Effects in Water, Enabling Increased Throughput Micromachining in Transparent Materials," Appl. Sci. 9(12), 2405 (2019).
- 142. M. Sun, U. Eppelt, W. Schulz, and J. Zhu, "Ultrafast reflection and secondary ablation in laser processing of transparent dielectrics with ultrashort pulses," Opt. Eng. **53**(5), 051512 (2014).
- 143. H. Shin and D. Kim, "Cutting thin glass by femtosecond laser

- ablation," Opt. Laser Technol. 102, 1-11 (2018).
- 144. E. Markauskas, L. Zubauskas, G. Račiukaitis, and P. Gečys, "Femtosecond Laser Cutting of 110–550 μm Thickness Borosilicate Glass in Ambient Air and Water," Micromachines **14**(1), 176 (2023).
- 145. S. Butkus, D. Paipulas, D. Kaškelyte, E. Gaižauskas, and V. Sirutkaitis, "Improvement of Cut Quality in Rapid-Cutting of Glass Method via Femtosecond Laser Filamentation," J. Laser Micro Nanoeng. **10**(1), 59–63 (2015).
- 146. K. L. Wlodarczyk, A. Brunton, P. Rumsby, and D. P. Hand, "Picosecond laser cutting and drilling of thin flex glass," Opt. Lasers Eng. **78**(October), 64–74 (2016).
- 147. C. Moorhouse, "Advantages of Picosecond Laser Machining for Cutting-Edge Technologies Advantages of picosecond laser machining for cutting-edge technologies," Phys. Procedia 41(December 2013), 381–388 (2015).
- 148. C. Fornaroli, J. Holtkamp, and A. Gillner, "Laser-beam helical drilling of high quality micro holes," Phys. Procedia **41**, 661–669 (2013).
- 149. D. Brinkmeier, V. Onuseit, and T. Graf, "Feasibility assessment of parallelized helical drilling," Opt. Eng. **62**(03), 1–13 (2023).
- 150. H. Le, C. Pradhani, P. Penchev, V. Nasrollahi, T. Karkantonis, Y. Wang, S. Dimov, and J. A. Ramos-de-Campos, "Laser precession machining of cross-shaped terahertz bandpass filters," Opt. Lasers Eng. **149**(August 2021), 106790 (2022).
- 151. X. Hao, W. Xu, M. Chen, C. Wang, J. Han, L. Li, and N. He, "Laser hybridizing with micro-milling for fabrication of high aspect ratio micro-groove on oxygen-free copper," Precis. Eng. **70**(December 2020), 15–25 (2021).
- 152. X. Sun, J. Zheng, C. Liang, Y. Hu, and H. Zhong, "Improvement of rear damage of thin fused silica by liquid assisted femtosecond laser cutting," Appl. Phys. A **125**(7), 1–8 (2019).
- 153. S. Indrišiūnas, E. Svirplys, J. Jorudas, and I. Kašalynas, "Laser processing of transparent wafers with a algan/gan heterostructures and high-electron mobility devices on a backside," Micromachines **12**(4), (2021).
- 154. Naresh and P. Khatak, "Laser cutting technique: A literature review," Mater. Today Proc. **56**, 2484–2489 (2022).
- 155. A. Salleo, F. Y. Génin, M. D. Feit, A. M. Rubenchik, T. Sands, S. S. Mao, and R. E. Russo, "Energy deposition at front and rear surfaces during picosecond laser interaction with fused silica," Appl. Phys. Lett. **78**(19), 2840–2842 (2001).
- 156. B. Ma, K. Wang, J. Han, Z. Zhang, and X. Cheng, "Difference in laser-induced damage behavior between back and front surfaces," Laser Phys. **30**(3), (2020).
- 157. G. Račiukaitis, M. Brikas, P. Gečys, B. Voisiat, and M. Gedvilas, "Use of High Repetition Rate and High Power Lasers in Microfabrication:

- How to Keep the Efficiency High?," J. Laser Micro/Nanoengineering **4**(3), 186–191 (2009).
- 158. D. Crimella, T. Jwad, and A. G. Demir, "Microcutting of glass with high ablation efficiency by means of a high power ps-pulsed NIR laser," Opt. Laser Technol. **166**(June), 109645 (2023).
- 159. E. Markauskas and P. Gečys, "Thin water film assisted glass ablation with a picosecond laser," Procedia CIRP 74(March), 328–332 (2018).
- 160. E. Markauskas, L. Zubauskas, and P. Gečys, "Efficient milling and cutting of borosilicate glasses through a thin flowing water film with a picosecond laser," J. Manuf. Process. **68**(June), 898–909 (2021).
- 161. R. An, Y. Li, Y. Dou, H. Yang, and Q. Gong, "Simultaneous multimicrohole drilling of soda-lime glass by water-assisted ablation with femtosecond laser pulses," Opt. Express **13**(6), 1855 (2005).
- 162. D. Ashkenasi, T. Kaszemeikat, N. Mueller, A. Lemke, and H. J. Eichler, "Machining of glass and quartz using nanosecond and picosecond laser pulses," in *Laser Applications in Microelectronic and Optoelectronic Manufacturing (LAMOM) XVII*, G. Hennig, X. Xu, B. Gu, and Y. Nakata, eds. (2012), **8243**, p. 82430M.
- 163. U. Chaulagain, S. Karatodorov, M. Raclavsky, S. Lorenz, M. Lamac, M. Albrecht, V. Tomkus, J. Dudutis, M. Mackevičiūtė, P. Gečys, and J. Nejdl, "Tomographic characterization of gas jets for laser-plasma acceleration with increased sensitivity," in *International Conference on X-Ray Lasers* 2020, D. Bleiner, ed. (SPIE, 2021), (July), p. 9.
- 164. Y. Li, K. Itoh, W. Watanabe, K. Yamada, D. Kuroda, J. Nishii, and Y. Jiang, "Three-dimensional hole drilling of silica glass from the rear surface with femtosecond laser pulses," Opt. Lett. **26**(23), 1912 (2001).
- 165. S. G. Demos, R. A. Negres, R. N. Raman, M. D. Feit, K. R. Manes, and A. M. Rubenchik, "Relaxation dynamics of nanosecond laser superheated material in dielectrics," Optica **2**(8), 765 (2015).
- 166. M. D. Crisp, N. L. Boling, and G. Dubé, "Importance of Fresnel reflections in laser surface damage of transparent dielectrics," Appl. Phys. Lett. **21**(8), 364–366 (1972).
- 167. V. Tomkus, V. Girdauskas, J. Dudutis, P. Gečys, V. Stankevič, and G. Račiukaitis, "High-density gas capillary nozzles manufactured by hybrid 3D laser machining technique from fused silica," Opt. Express **26**(21), 27965 (2018).
- 168. E. Markauskas, L. Zubauskas, B. Voisiat, and P. Gečys, "Efficient Water-Assisted Glass Cutting with 355 nm Picosecond Laser Pulses," Micromachines 13(5), 785 (2022).
- 169. S. Schwarz, S. Rung, C. Esen, and R. Hellmann, "Enhanced ablation efficiency using GHz bursts in micromachining fused silica," Opt. Lett. **46**(2), 282 (2021).
- 170. Y. Yang, S. Schwarz, C. Esen, and R. Hellmann, "Influence of MHz bursts on the ablation efficiency of fused silica," J. Laser Appl. **35**(2), (2023).

- 171. S. M. Remund, M. Gafner, M. V. Chaja, A. Urniezius, S. Butkus, and B. Neuenschwander, "Milling applications with GHz burst: Investigations concerning the removal rate and machining quality," Procedia CIRP **94**, 850–855 (2020).
- 172. P. Balage, M. Lafargue, T. Guilberteau, G. Bonamis, C. Hönninger, J. Lopez, and I. Manek-Hönninger, "Femtosecond Laser Percussion Drilling of Silicon Using Repetitive Single Pulse, MHz-, and GHz-Burst Regimes," Micromachines **15**(5), 632 (2024).
- 173. J. Lopez, S. Niane, G. Bonamis, P. Balage, E. Audouard, C. Hönninger, E. Mottay, and I. Manek-Hönninger, "Percussion drilling in glasses and process dynamics with femtosecond laser GHz-bursts," Opt. Express 30(8), 12533 (2022).
- 174. P. Balage, G. Bonamis, M. Lafargue, T. Guilberteau, M. Delaigue, C. Hönninger, J. Qiao, J. Lopez, and I. Manek-Hönninger, "Advances in Femtosecond Laser GHz-Burst Drilling of Glasses: Influence of Burst Shape and Duration," Micromachines **14**(6), 1–10 (2023).
- 175. P. Balage, T. Guilberteau, M. Lafargue, G. Bonamis, C. Hönninger, J. Lopez, and I. Manek-Hönninger, "Pump-Probe Imaging of Ultrafast Laser Percussion Drilling of Glass in Single Pulse, MHz- and GHz-Burst Regimes," Adv. Mater. Interfaces **2400853**, 1–9 (2025).
- 176. Y. Zhang, T. Koike, R. Yoshizaki, G. Ren, A. Shibata, S. Kiriake, R. Hasegawa, I. Nagasawa, K. Nagato, N. Sugita, and Y. Ito, "Ultrahigh-speed laser drilling of transparent materials via transient electronic excitation," Sci. Adv. 11(24), (2025).
- 177. J. Del Hoyo, R. Meyer, L. Furfaro, and F. Courvoisier, "Nanoscale confinement of energy deposition in glass by double ultrafast Bessel pulses," Nanophotonics **10**(3), 1089–1097 (2021).
- 178. F. Hendricks, V. V Matylitsky, M. Domke, and H. P. Huber, "Timeresolved study of femtosecond laser induced micro-modifications inside transparent brittle materials," PROC SPIE **9740**, 1–8 (2016).
- 179. C. Javaux Léger, K. Mishchik, O. Dematteo-Caulier, S. Skupin, B. Chimier, G. Duchateau, A. Bourgeade, C. Hönninger, E. Mottay, J. Lopez, and R. Kling, "Effects of burst mode on transparent materials processing," in *Laser-Based Micro- and Nanoprocessing IX*, U. Klotzbach, K. Washio, and C. B. Arnold, eds. (2015), **9351**, p. 93510M.
- 180. J. Liu, J. Yang, H. Chen, J. Li, D. Zhang, J. Zhong, and X. Pan, "High-Quality Cutting of Soda–Lime Glass with Bessel Beam Picosecond Laser: Optimization of Processing Point Spacing, Incident Power, and Burst Mode," Appl. Sci. 14(5), (2024).
- 181. L. Rapp, R. Meyer, R. Giust, L. Furfaro, M. Jacquot, P. A. Lacourt, J. M. Dudley, and F. Courvoisier, "High aspect ratio micro-explosions in the bulk of sapphire generated by femtosecond Bessel beams," Sci. Rep. 6(1), 34286 (2016).
- 182. B. Zhang, X. Liu, and J. Qiu, "Single femtosecond laser beam induced

- nanogratings in transparent media Mechanisms and applications," J. Mater. **5**(1), 1–14 (2019).
- 183. P. G. Kazansky, H. Inouye, T. Mitsuyu, K. Miura, J. Qiu, K. Hirao, and F. Starrost, "Anomalous Anisotropic Light Scattering in Ge-Doped Silica Glass," Phys. Rev. Lett. **82**(10), 2199–2202 (1999).
- 184. Y. Shimotsuma, P. G. Kazansky, J. Qiu, and K. Hirao, "Self-organized nanogratings in glass irradiated by ultrashort light pulses," Phys. Rev. Lett. **91**(24), 1–4 (2003).
- 185. J. Morikawa, A. Orie, T. Hashimoto, and S. Juodkazis, "Thermal and optical properties of the femtosecond-laser-structured and stress-induced birefringent regions in sapphire," Opt. Express **18**(8), 8300 (2010).
- 186. R. Buividas, M. Mikutis, and S. Juodkazis, "Surface and bulk structuring of materials by ripples with long and short laser pulses: Recent advances," Prog. Quantum Electron. **38**(3), 119–156 (2014).
- 187. B. McMillen and Y. Bellouard, "On the anisotropy of stress-distribution induced in glasses and crystals by non-ablative femtosecond laser exposure," Opt. Express 23(1), 86 (2015).
- 188. A. Champion, M. Beresna, P. Kazansky, and Y. Bellouard, "Stress distribution around femtosecond laser affected zones: effect of nanogratings orientation," Opt. Express **21**(21), 24942 (2013).
- 189. D. Grojo, M. Gertsvolf, H. Jean-Ruel, S. Lei, L. Ramunno, D. M. Rayner, and P. B. Corkum, "Self-controlled formation of microlenses by optical breakdown inside wide-band-gap materials," Appl. Phys. Lett. **93**(24), 138–141 (2008).
- 190. Z. Guo, K. Hu, T. Cao, S. Liu, J. Yan, Z. Li, Q. Xu, P. B. Corkum, and J. Peng, "Energy deposition and incubation effects of nonlinear absorption of ultrashort laser pulses in dielectrics," Opt. Express **30**(7), 10317 (2022).
- 191. Z. Li, L. Wang, H. Fan, Y. Yu, Q. Chen, S. Juodkazis, and H.-B. Sun, "O-FIB: far-field-induced near-field breakdown for direct nanowriting in an atmospheric environment," Light Sci. Appl. 9(1), 41 (2020).
- 192. Y. Lei, M. Sakakura, L. Wang, Y. Yu, H. Wang, G. Shayeganrad, and P. G. Kazansky, "High speed ultrafast laser anisotropic nanostructuring by energy deposition control via near-field enhancement," Optica 8(11), 1365 (2021).
- 193. Z. Z. Li, H. Fan, L. Wang, X. Zhang, X. J. Zhao, Y. H. Yu, Y. S. Xu, Y. Wang, X. J. Wang, S. Juodkazis, Q. D. Chen, and H. B. Sun, "Superstealth dicing of transparent solids with nanometric precision," Nat. Photonics **18**(8), 799–808 (2024).
- 194. J. M. Guay, A. Villafranca, F. Baset, K. Popov, L. Ramunno, and V. R. Bhardwaj, "Polarization-dependent femtosecond laser ablation of poly-methyl methacrylate," New J. Phys. 14, (2012).
- 195. K. I. Popov, C. McElcheran, K. Briggs, S. Mack, and L. Ramunno, "Morphology of femtosecond laser modification of bulk dielectrics,"

- Opt. Express 19(1), 271 (2011).
- 196. L. Rapp, R. Meyer, L. Furfaro, C. Billet, R. Giust, and F. Courvoisier, "High speed cleaving of crystals with ultrafast Bessel beams," Opt. Express **25**(8), 9312 (2017).
- 197. K. Yamada, W. Watanabe, J. Nishii, and K. Itoh, "Anisotropic refractive-index change in silica glass induced by self-trapped filament of linearly polarized femtosecond laser pulses," J. Appl. Phys. **93**(4), 1889–1892 (2003).
- 198. J. Yu, H. Jiang, H. Yang, and Q. Gong, "Polarization effect during propagation of a femtosecond laser pulse in fused silica glass," J. Opt. Soc. Am. B **29**(8), 1937 (2012).
- 199. S. Rekštytė, T. Jonavičius, D. Gailevičius, M. Malinauskas, V. Mizeikis, E. G. Gamaly, and S. Juodkazis, "Nanoscale Precision of 3D Polymerization via Polarization Control," Adv. Opt. Mater. 4(8), 1209–1214 (2016).
- 200. E. G. Gamaly and A. V. Rode, "Coupling of polarisation of high frequency electric field and electronic heat conduction in laser created plasma," Opt. Laser Technol. **82**, 69–71 (2016).
- 201. V. Stankevič, G. Račiukaitis, F. Bragheri, X. Wang, E. G. Gamaly, R. Osellame, and S. Juodkazis, "Laser printed nano-gratings: Orientation and period peculiarities," Sci. Rep. 7(November 2016), 1–8 (2017).
- 202. X. Nie, W. W. Chen, A. A. Wereszczak, and D. W. Templeton, "Effect of loading rate and surface conditions on the flexural strength of borosilicate glass," J. Am. Ceram. Soc. **92**(6), 1287–1295 (2009).
- 203. H. Tada, P. C. Paris, and G. R. Irwin, "The Stress Analysis of Cracks Handbook," Stress Anal. Cracks Handbook, Third Ed. (2000).
- 204. M. Ciccotti, "Stress-corrosion mechanisms in silicate glasses," J. Phys. D. Appl. Phys. 42(21), (2009).
- 205. P. Dwivedi and D. J. Green, "Indentation Crack-Shape Evolution during Subcritical Crack Growth," J. Am. Ceram. Soc. **78**(5), 1240–1246 (1995).
- 206. J. Pocorni, D. Petring, J. Powell, E. Deichsel, and A. F. H. Kaplan, "The Effect of Laser Type and Power on the Efficiency of Industrial Cutting of Mild and Stainless Steels," J. Manuf. Sci. Eng. 138(3), (2016).
- 207. M. Gedvilas and G. Račiukaitis, "Spatial zigzag evolution of cracks in moving sapphire initiated by bursts of picosecond laser pulses for ultrafast wafer dicing," RSC Adv. **10**(55), 33213–33220 (2020).
- 208. J. M. Liu, "Simple technique for measurements of pulsed Gaussianbeam spot sizes," Opt. Lett. 7(5), 196 (1982).
- 209. X. Jia and X. Zhao, "Ultrafast laser direct drilling of high aspect ratio microchannels in fused silica: Insights on channel self-termination mechanisms," Opt. Laser Technol. **157**(July 2022), 108766 (2023).
- 210. J. Lopez, S. Niane, G. Bonamis, P. Balage, and Inka-Manek-Hönninger, "In-Situ Monitoring of Bottom-Up Percussion Drilling of

- Alkali-Free Alumina-Borosilicate Thin Glasses Using Single and Double Femtosecond Laser Pulses," J. Laser Micro Nanoeng. **17**(1), 50–57 (2022).
- 211. G. Lott, N. Falletto, P.-J. Devilder, and R. Kling, "Optimizing the processing of sapphire with ultrashort laser pulses," J. Laser Appl. **28**(2), 022206 (2016).
- 212. A. Houard, V. Jukna, G. Point, Y.-B. André, S. Klingebiel, M. Schultze, K. Michel, T. Metzger, and A. Mysyrowicz, "Study of filamentation with a high power high repetition rate ps laser at 1.03 μm," Opt. Express 24(7), 7437 (2016).
- 213. Z. Wu, H. Jiang, Q. Sun, H. Yang, and Q. Gong, "Filamentation and temporal reshaping of a femtosecond pulse in fused silica," Phys. Rev. A At. Mol. Opt. Phys. **68**(6), 8 (2003).
- 214. W. Liu, S. L. Chin, O. Kosareva, I. S. Golubtsov, and V. P. Kandidov, "Multiple refocusing of a femtosecond laser pulse in a dispersive liquid (methanol)," Opt. Commun. **225**(1–3), 193–209 (2003).
- 215. A. K. Dharmadhikari, J. A. Dharmadhikari, and D. Mathur, "Visualization of focusing-refocusing cycles during filamentation in BaF2," Appl. Phys. B Lasers Opt. **94**(2), 259–263 (2009).
- 216. K. Lim, M. Durand, M. Baudelet, and M. Richardson, "Transition from linear- to nonlinear-focusing regime in filamentation," (December), (2014).
- 217. J.-P. Bérubé, R. Vallée, M. Bernier, O. Kosareva, N. Panov, V. Kandidov, and S. L. Chin, "Self and forced periodic arrangement of multiple filaments in glass," Opt. Express 18(3), 1801 (2010).
- 218. V. V. Temnov, K. Sokolowski-Tinten, P. Zhou, A. El-Khamhawy, and D. Von Der Linde, "Multiphoton ionization in dielectrics: Comparison of circular and linear polarization," Phys. Rev. Lett. **97**(23), 1–4 (2006).
- 219. J. Dudutis, R. Stonys, G. Račiukaitis, and P. Gečys, "Glass dicing with elliptical Bessel beam," Opt. Laser Technol. **111**(July 2018), 331–337 (2019).
- 220. N. Bloembergen, "Role of Cracks, Pores, and Absorbing Inclusions on Laser Induced Damage Threshold at Surfaces of Transparent Dielectrics," Appl. Opt. **12**(4), 661 (1973).
- 221. F. Werr, A. Veber, M. Brehl, M. Bergler, D. Werner, U. Eppelt, L. Müllers, and D. de Ligny, "Surface Probing of Ultra-Short-Pulse Laser Filament Cut Window Glass and the Impact on the Separation Behavior," Adv. Eng. Mater. 22(9), 1–9 (2020).
- 222. K. Liao, W. Wang, X. Mei, and B. Liu, "High quality full ablation cutting and stealth dicing of silica glass using picosecond laser Bessel beam with burst mode," Ceram. Int. **48**(7), 9805–9816 (2022).
- 223. R. Meyer, R. Giust, M. Jacquot, J. M. Dudley, and F. Courvoisier, "Submicron-quality cleaving of glass with elliptical ultrafast Bessel beams," Appl. Phys. Lett. **111**(23), (2017).

- 224. A. Feuer, J. U. Thomas, C. Freitag, R. Weber, and T. Graf, "Single-pass laser separation of 8 mm thick glass with a millijoule picosecond pulsed Gaussian–Bessel beam," Appl. Phys. A Mater. Sci. Process. **125**(5), 1–6 (2019).
- 225. M. K. Bhuyan, O. Jedrkiewicz, V. Sabonis, M. Mikutis, S. Recchia, A. Aprea, M. Bollani, and P. Di Trapani, "High-speed laser-assisted cutting of strong transparent materials using picosecond Bessel beams," Appl. Phys. A Mater. Sci. Process. 120(2), 443–446 (2015).
- 226. F. Ahmed, M. Seop, L. Hitoshi, T. Sumiyoshi, and M. Kamata, "Display glass cutting by femtosecond laser induced single shot periodic void array," Appl. Phys. A **93**, 189–192 (2008).
- 227. F. Werr, U. Eppelt, L. Müllers, and D. de Ligny, "Ultra-Short-Pulse Laser Filaments for Float Glass Cutting: Influence of Laser Parameters on Micro Cracks Formation," Front. Phys. **10**(March), 1–19 (2022).
- 228. S. Butkus, D. Paipulas, R. Sirutkaitis, E. Gaižauskas, and V. Sirutkaitis, "Rapid Cutting and Drilling of Transparent Materials via Femtosecond Laser Filamentation," **9**(3), 213–220 (2014).
- 229. P. Liu, L. Deng, F. Zhang, H. Chen, J. Duan, and X. Zeng, "Study on high-efficiency separation of laminated glass by skillfully combining laser-induced thermal-crack propagation and laser thermal melting," Appl. Phys. A Appl. Phys. A-Mater 126(4), (2020).
- 230. J. Yang, J. Wei, D. Zhang, X. Pan, L. Shui, M. Jin, R. Che, and Y. Liu, "A simple structure laser three-focus scheme for thick glass separation," AIP Adv. 11(11), (2021).
- 231. L. J. Yang, Y. Wang, Z. G. Tian, and N. Cai, "YAG laser cutting sodalime glass with controlled fracture and volumetric heat absorption," Int. J. Mach. Tools Manuf. **50**(10), 849–859 (2010).
- 232. K. Yamamoto, N. Hasaka, H. Morita, and E. Ohmura, "Thermal stress analysis on laser scribing of glass," J. Laser Appl. **20**(4), (2008).
- 233. S. T. Chen and S. H. Liao, "Development of a diamond scribing wheel with unequal-pitch micro-penetration teeth," Mater. Manuf. Process. **40**(1), 69–79 (2024).
- 234. R. Hasegawa, S. Matsusaka, H. Hidai, A. Chiba, N. Morita, and T. Onuma, "In-process estimation of fracture surface morphology during wheel scribing of a glass sheet by high-speed photoelastic observation," Precis. Eng. 48, 164–171 (2017).
- 235. J. Wang, Z. Jia, and Y. B. Guo, "Shape-cutting of quartz glass by spark discharge-assisted diamond wire sawing," J. Manuf. Process. **34**(March), 131–139 (2018).
- 236. U. Simsir, "Prevention Of Chips Formed İn Circular Cutting Of Glass Plates With Water Jet Cutter," **6**(9), 3564–3568 (2022).
- 237. M. Sutowska, W. Kapłonek, D. Y. Pimenov, M. K. Gupta, M. Mia, and S. Sharma, "Influence of Variable Radius of Cutting Head Trajectory on Quality of Cutting Kerf in the Abrasive Water Jet Process for Soda– Lime Glass," Materials (Basel). 13(19), 4277 (2020).

SANTRAUKA

Ivadas

Stiklas yra plačiai naudojamas architektūroje, medicinoje, elektronikoje bei daugelyje kitų sričių [1]. Vis dėlto, prieš naudojimą, stiklas turi būti apdirbtas. Dėl savo trapumo, stiklo pjovimas kelia nemažai technologinių iššūkių [2,3].

Labiausiai paplitęs stiklo pjovimo būdas yra mechaninis raižymas ir atskyrimas, pasižymintis paprastumu, greitumu ir pigumu [4]. Tačiau raižymo metu suformuojami dideli paviršiaus apskeldėjimai. Taip pat ši technologija gali būti pritaikyta tik paprastų kontūrų pjovimui. Sudėtingiems kontūrams gali būti naudojamas pjovimas viela ar vandens srove. Tačiau šie alternatyvus mechaniniai pjovimo būdai yra žymiai lėtesni lyginant su raižymu. Tikslumas, kokybė, pjovimas sudėtingomis trajektorijomis ar sparta gali būti pasiekti apdirbant stiklą su lazeriais.

Lazerinis pjovimas įprastai atliekamas pluoštą fokusuojant į viršutinį bandinio paviršių. Tokiu būdu medžiaga yra pašalinama iš viršaus į apačią, o toks apdirbimo būdas vadinamas pjovimas nuo viršaus arba sutrumpintai TDC (angl. top-down cutting). Stiklams skaidriems lazerio spinduliuotei gali būti pritaikyti alternatyvūs pjovimo būdai. Didelio intensyvumo impulsai sufokusuoti į mikrometrinio dydžio dėmę gali sukelti netiesinę sugertį ir pažeidimus stiklo tūryje. Keičiant pluošto sąsmaukos poziciją, pažeidimai gali būti suformuojami skirtingame gylyje. Todėl stiklas gali būti apdirbtas pluoštą fokusuojant į apatinį bandinio paviršių ir šalinant medžiagą iš apačios į viršų. Pjovimas nuo apatinės pusės, arba sutrumpintai BUC (angl. bottom-up cutting), pasižymi didesniu efektyvumu, lyginant su TDC, bei leidžia suformuojant tūrinės modifikacijas. Lazerinis raižymas dažniausiai atliekamas formuojant pailgas modifikacijas su Beselio pluoštu arba šviesos gijomis. Šis stiklo apdirbimo būdas leidžia pasiekti m/s raižymo greičius [6].

Nuolatinė pažanga lazerinių šaltinių srityje skatina apdirbimo technologijų tobulėjimą. Įvairūs tyrimai rodo, jog lazeriniai šaltiniai, veikiantys MHz, GHz papliūpų ar dvigubų papliūpų režimais, gali pagerinti metalų [7,8], polimerų [11,12], dielektrikų [13,14] ir puslaidininkių [9,10] apdirbimą. Tačiau dauguma darbų yra atlikti medžiagas apdirbant nuo viršutinės pusės. Todėl vis dar trūksta darbų, tiriančių papliūpų režimo įtaką stiklo pjovimui nuo apatinės pusės, modifikacijų formavimui šviesos gijomis bei jų pritaikymui raižyme.

Šiame darbe buvo tiriama lazeriniu MHz, GHz bei dvigubu papliūpu režimu itaka stiklo apdirbimui, naudojant švelnaus fokusavimo sistema $(NA \sim 0.04)$. Spartus pluošto skenavimas buvo pasiektas naudojant galvanoskenerius ir fokusuojant pluoštą telecentriniu f-theta lęšiu. Pirmoje eksperimentinėje disertacijos dalyje, buvo vystoma sparti ir efektyvi kalcionatrio silikatinio stiklo (SLG, angl. soda-lime glass) pjovimo nuo apatinės pusės technologija, pasitelkiant papliūpų režimą ir optimizuojant proceso parametrus. Rezultatai palyginti su darbais demonstruojančiais stiklo pjovima (i) nuo viršaus (TDC); (ii) nuo viršaus su papildomu vandens sluoksniu (WATDC, angl. water-assisted top-down cutting) ir (iii) nuo apačios (BUC). Taip pat pademonstruotos plačios stiklo apdirbimo galimybės – pasvirojo cilindro, sudėtingų trajektorijų ir įvairaus storio (1–18.8 mm) stiklo pjovimas spartaus ir kokybiško apdirbimo režimu pritaikymas tam pačiam bei bandiniui, naudojant skirtingus proceso parametrus. Antroje dalyje, MHz, GHz bei dvigubų papliūpų režimai buvo pritaikyti modifikacijų formavimui lydyto kvarco (FS, angl. *fused silica*) ir SLG bandinių tūryje šviesos gijomis. Ištirta modifikaciju išilginių ilgių ir pozicijų bei skersinių ilgių ir kampu priklausomybė nuo lazerinių apdirbimo parametrų. Trečioje dalyje, atliktas 1.1 mm storio SLG raižymas naudojant modifikacijas suformuotas su šviesos gijomis pasitelkus dvigubos papliūpos režimą. Remiantis turima informacija, šiame darbe pademonstruotas didžiausias iki šiol pasiektas stiklo raižymo greitis.

Darbo tikslas ir uždaviniai

Šio darbo tikslas – ištirti lazerinių papliūpų poveikį stiklo pjovimui nuo apačios, tūrinių modifikacijų formavimui šviesos gijomis ir jų pritaikymui stiklo raižymui. Tyrimo uždaviniai buvo (i) išvystyti sparčią kalcio-natrio silikatinio stiklo pjovimo nuo apatinės pusės technologiją, pasitelkiant papliūpų režimą; (ii) įvertinti lazerinių papliūpų poveikį modifikacijoms, suformuotoms lydytame kvarce ir kalcio-natrio silikatiniame stikle su šviesos gijomis; (iii) ištirti 1.1 mm storio kalcio-natrio silikatinio stiklo raižymą su šviesos gijomis suformuotomis modifikacijomis su poliarizacija valdomais įtrūkiais.

Praktinė nauda ir naujumas

Darbe buvo ištirtas naujas kalcio-natrio silikatinio stiklo pjovimo nuo apatinės pusės taikymas, pasitelkiant GHz papliūpų režimą. Atliekant pjovimą nuo

apatinės pusės su 1030 nm bangos ilgiu ir pikosekundinių impulsų GHz papliūpomis pavyko pasiekti daugiau nei eile efektyvesnį pjovimą lyginant su tyrimais taikančiais tradicinę tiesioginę abliaciją su pavieniais impulsais. Aukštas pjovimo efektyvumas pasiektas medžiagą skaldant į µm dydžio daleles. Efektyvus pjovimas skaldant taip pat pasiekiamas naudojant 532 nm bangos ilgio nanosekundinius impulsus. Tačiau lazerio veikimas fundamentiniu bangos ilgiu yra pranašesnis, nes išvengiama konversija į aukštesnes harmonikas, o tai leidžia išnaudoti visą lazerio galią. Be to, veikiant fundamentiniu bangos ilgiu, užtikrinamas didesnis sistemos stabilumas, nes yra išvengiamas netiesinio kristalo pažeidimas.

Darbe pademonstruotras stiklo pjovimas naudojant kintamus proceso parametrus. Keičiant subimpulsų per papliūpą skaičių, tam pačiam bandiniui buvo pritaikyti didelio našumo ir aukštos kokybės apdirbimo režimai.

Naudojant švelnų fokusavimą (NA ~0.04) ir ultratrumpų impulsų papliūpas pavyko suformuoti tūrines modifikacijas su skersiniais įtrūkiais lydyto kvarco ir kalcio-natrio silikatinio stikluose. Pademonstruotas įtrūkių kampo valdymas poliarizacija ir asimetriniu pluoštu. Inovatyvus įtrūkių valdymas poliarizacija pritaikytas 1.1 mm storio kalcio-natrio silikatinio stiklo raižymui. Atstumas tarp modifikacijų, o kartu ir raižymo greitis buvo padidinti orientuojant įtrūkius pagal pluošto skenavimo trajektoriją. Naudojant galvanoskenerio ir telecentrinio f-theta lęšio sistemą buvo pasiektas 10 m/s raižymo greitis. Mūsų turimomis žiniomis, tai didžiausias iki šiol pademonstruotas stiklo raižymo greitis.

Ginamieji teiginiai

- 1. Kalcio-natrio silikatinis stiklas gali būti efektyviai apdirbtas naudojant pikosekundinių impulsų GHz papliūpas, išlaikant aukštą paviršiaus kokybę, taikant didesnį subimpulsų papliūpoje skaičių pjovimui nuo apatinės pusės ir formuojant kontroliuojamus įtrūkius tūryje, bei naudojant mažesnį subimpulsų papliūpoje skaičių netoli viršutinio ir apatinio paviršių, siekiant atlikti tikslią abliaciją.
- 2. Šviesos gijos suformuotos su ultratrumpaisiais impulsais naudojant papliūpų (GHz arba MHz) ir dvigubų papliūpų režimus ir švelnaus fokusavimo sąlygas (NA ~0.04) gali sukurti pailgas tūrines modifikacijas lydytame kvarce (<1.4 mm) ir kalcio-natrio silikatiniame stikle (<0.9 mm) su poliarizacija valdomais skersiniais įtrūkiais.

3. Švelniai sufokusuoto pluošto nukreipimas su galvanometriniu skeneriu, kartu su dvigubos papliūpos režimo taikymu, šviesos gijomis formuojant pailgas tūrines modifikacijas, kurių skersinė orientacija, nulemta poliarizacijos, yra lygiagreti pluošto skenavimo krypčiai, leidžia pasiekti aukštą (iki 10 m/s) raižymo greitį vienu skenavimu 1.1 mm storio kalcio-natrio silikatiniame stikle.

Publikacijos

Pagrindiniai rezultatai publikuoti 3-ijuose moksliniuose žurnaluose [A1–A3]. Autorė pristatė rezultatus 5-iose tarptautinėse konferencijose [D1–D5].

Autorės indėlis

Autorė atliko didžiąją dalį eksperimentų, duomenų analizių ir vizualizacijų. Taip pat parengė mokslinių straipsnių rankraščius [A1–A3].

Bendraautorių indėlis

- Dr. Paulius Gečys vadovavo visam tiriamojo darbo procesui.
- Dr. Juozas Dudutis konsultavo mokslinių tyrimų klausimais, padėjo su pluošto apibudinimo matavimais, sumodeliavo bandinių atskyrimo stiprio priklausomybę nuo pažeidimo zonos ilgio.
- Aleksandras Kondratas atliko tūrinių pažeidimų suformuotų kalcio-natrio silikatiniame stikle apibudinimą. Taip pat pamatavo bandinių atskyrimo stiprį bei įvertino suraižytų ir atskirtų bandinių kokybę.
- Dr. Julijanas Želudevičius padėjo išmatuoti ultratrumpųjų impulsų papliūpų laikines savybes.
- Light Conversion suteikė galimybę atlikti darbą su jų pagamintais lazeriais.

Eksperimentinė įranga

Tyrimas atliktas naudojant eksperimentinę schemą pateiktą 2-ajame disertacijos skyriuje. Eksperimentai atlikti su tiesine arba apskritimine poliarizacija, pasitelkus atitinkamai $\lambda/2$ ir $\lambda/4$ bangines plokšteles. Maždaug ~8 mm diametro pluoštas buvo fokusuojamas su 100 mm židinio nuotolio telecentriniu f-theta lęšiu. Taigi eksperimentai atlikti naudojant švelnų fokusavimą (NA ~0.04). Pluošto padėtis X ir Y ašyse buvo keičiama su galvanometriniais skeneriais, kurių greitis siekė iki 9 m/s (3-iąjai disertacijos daliai, išskyrus 3.2 poskyrį), 6 m/s (3.2 poskyriui) arba 10 m/s (4-ąjai ir 5-ąjai disertacijos dalims). Galvanoskenerių ir f-theta lęšio padėtis Z ašyje buvo keičiama su linijiniu pozicionavimo staliuku.

Tyrimai atlikti su Carbide serijos lazeriais naudojant parametrus pateiktus 1-oje lentelėje. Stiklas buvo apdirbamas su MHz, GHz arba dvigubos papliūpos režimais. Paprastumo dėlei, MHz ir GHz papliūpų režimai bus pateikti nurodant subimpulsų (vidinių impulsų papliūpoje) skaičių, atitinkamai šalia N arba P raidės. Dvigubų papliūpų režimas P10N5 atitiks 10-ies impulsų paketą, kuriame impulsai pasikartoja pikosekundžių eilės intervalais, o visas paketas kartojasi 5 kartus su nanosekundžių eilės pertraukomis. Papliūpų laikinės savybės pateiktos 2.1 skyriuje.

Lazerio pluošto erdvinis intensyvumo pasiskirstymas XY plokštumoje išmatuotas skirtingose Z pozicijose aplink pluošto sąsmauką. Pluoštas buvo asimetrinis su eliptiškumu siekiančiu 1.5. Aukščiau sąsmaukos, pluošto elipsės ilgoji ašis buvo nukreipta maždaug -40 deg kampu. Sąsmaukos pozicijoje pluoštas buvo arti apskritiminio, o diametras siekė ~20 μm . Žemiau sąsmaukos, pluošto ilgoji ašis pakrypo ~60 deg kampu.

1 lentelė. Eksperimentuose naudotų lazerių parametrai. Čia τ_p yra impulso trukmė, λ – bangos ilgis, P_{ave} – vidutinė lazerio galia, f_{B} – papliūpų pasikartojimo dažnis, E_{B} – papliūpos energija, $f_{\text{B-intra}}$ – subimpulsų pasikartojimo dažnis.

1	τ _p , ps	P_{ave} ,	$f_{\rm B}$,	$E_{\rm B}$, $\mu {\rm J}$	Subimpulsų	Papliūpų	Eksperimentas
		W	kHz		periodas (f _{B-intra})	režimas	
M^2	5–20	40	200	<180	404 ps (2.5 GHz)	P25N1,	Pjovimas nuo apatinės
m,						P30N1	pusės (SLG)
1030 nm,	0.221	80	100	<170	465 ps (2.2 GHz)	P(1-20)N1,	Vienašūvės
103					16 ns (62.5 MHz)	P1N(1-20)	modifikacijos (FS)
7							
	0.176-8	40	100	<350	470 ps (2.1 GHz)	P(1-10)N5,	Vienašūvės
Carbide,					15.8 ns (63.3 MHz)	P10N(1-10)	modifikacijos (SLG)
Ca	0.176-4	40	100	200;	470 ps (2.1 GHz)	P10N5	Raižymas (SLG)
				300	15.8 ns (63.3 MHz)		

Pjovimas nuo apatinės pusės

Pjovimas nuo apatinės pusės (BUC) atliktas 4.8 mm storio SLG bandiniuose pjaunant 20 mm diametro apskritimus. Pjovimo pradžioje, pluošto sąsmauka pozicionuojama žemiau apatinio bandinio paviršiaus. Tuomet XY plokštumoje pluoštas pradedamas skenuoti spiralės trajektorija. Tuo pačiu metu pastoviu greičiu keliama pluošto sąsmaukos padėtis. Procesas atliekamas tol, kol medžiaga perpjaunama kiaurai.

Pjovimas buvo atliekamas su P25N1 ir P30N1 papliūpų režimais, naudojant skirtingą impulsų trukmę (5–20 ps), papliūpų energiją (<180 μJ), atstumą tarp šūvių ir linijų (5–45 μm) ir vertikalų greitį (<0.3 mm/s). Eksperimento metu buvo siekiama kiekvienai impulso trukmės bei papliūpos energijos kombinacijai surasti optimalų atstumą tarp šūvių ir linijų, kuris leistų pasiekti didžiausią vertikalų greitį.

Norint pasiekti didžiausią pjovimo greitį, impulsų trukmė turi būti parenkama atsižvelgiant į didžiausią galimą lazerio papliūpos energiją. Naudojant didesnes papliūpų energijas, palanku naudoti ilgesnes subimpulsų trukmes, padidinti subimpulsų skaičių bei atstumą tarp šūvių ir linijų. Optimizavus parametrus, su pikosekundiniais impulsais GHz papliūpose buvo pasiektas efektyvus (0.13 mm/J) ir greitas (4.2 mm/s) 4.8 mm storio SLG pjovimas. Vidutinis paviršiaus apskeldėjimas siekė 90 μ m ir 400 μ m atitinkamai viršutiniam ir apatiniam paviršiams. Vidutinis pjūvio sienelių šiurkštumas R_a sieke 2.3 μ m.

Šiame darbe gauti rezultatai buvo palyginti su kitais pjovimo būdais lazeriu pašalinant medžiagą (TDC, WATDC ir BUC). Kadangi pjovimo greitis ir efektyvumas tiesiogiai priklauso nuo bandinio storio, papildomai atliktas 1 mm storio SLG pjovimas. Parodyta, jog su BUC technologija pasiekiamas daugiau nei eile didesnis pjovimo greitis ir efektyvumas lyginant su TDC ir WATDC būdais. Darbe pasiektas pjovimo efektyvumas buvo palyginamas pjovimui su nanosekundiniais impulsais ir 532 nm bangos ilgiu. Abiem atvejais medžiaga yra pašalinama skaldymo būdu, kuris pasižymi didesniu efektyvumu nei išgarinimas. Tačiau dirbant su fundamentiniu lazerio bangos ilgiu galima išnaudoti visą lazerio galią. Tuo metu konversijos į aukštesnes harmonikas metu prarandama dalis energijos. Šiame darbe pademonstruoti santykiniai pjovimo greičiai ir efektyvumai buvo atitinkamai 8–134 ir 3.2–64 kartų didesni lyginant su kitais TDC, WATDC ir BUC darbais, atliktais su ~1 μm bangos ilgiu.

Darbe pademonstruotos plačios BUC pritaikymo galimybės – atliktas įvairaus storio (1–18.8 mm), sudėtingos trajektorijos (Lietuvos kontūrų) bei pasvirojo cilindro formos elemento pjovimas iš 4.8 mm storio stiklo. Pasvirojo cilindro pjovimas atliktas kiekvienoje Z pozicijoje pastumiant pluošto skenavimo zoną per Δx . Didžiausias išpjauto pasvirojo cilindro kampas siekė 35 deg. Pastebėta, jog didinant cilindro kampą, ima prastėti šoninių sienelių kokybė – 35 deg kampo cilindrinio elemento vidutinis sienelių paviršiaus šiurkštumas (R_a) siekė 5.7 μ m.

Tyrimai parodė, jog lazeriai su GHz papliūpomis gali reikšmingai padidinti SLG pjovimo greitį, lyginant su klasikiniu tiesioginės abliacijos pjovimu pavieniais impulsais. Tačiau greitas ir efektyvus pjovimas lemia suprastėjusią bandinių kokybę. Visgi šiuolaikinės lazerinės sistemos leidžia greitai keisti apdirbimo parametrus, todėl tą patį bandinį galima apdirbti tiek sparčiu, tiek aukštos kokybės režimais. Toks apdirbimo metodas buvo pademonstruotas pjaunant elementą sparčiu (2.3 mm³/s) ir formuojant nuožulnas aukštos kokybės (0.4–0.7 mm³/s) režimais. Spartaus ir aukštos kokybės režimų panaudojimas tam pačiam bandiniui parodo, kad BUC technologija turi potencialą būti taikoma optinių elementų gamyboje.

Tūrinių modifikacijų formavimas

Tūrinės modifikacijos buvo formuojamos pluoštą fokusuojant į 1.45 mm (FS) ir 1 mm (SLG) gylį. Kiekviena modifikacija buvo suformuota su vienu šūviu. Eksperimentai atlikti 100 x 100 x 4.8 mm³ SLG ir 150 x 150 x 6.3 mm³ FS stikluose. Išilginėms modifikacijoms matuoti papildomai naudoti 20 x 1 x 6.3 mm³ FS bandiniai su poliruotomis sienelėmis.

Tūrinės modifikacijos buvo apibudinamos matuojant jų skersinį (XY plokštuma, statmenai pluošto sklidimo krypties) ilgį ir kampą bei išilginį (YZ plokštuma, išilgai pluošto sklidimo krypties) ilgį bei pradžios ir pabaigos padėtis. Skersiniai ilgiai ir kampai buvo matuoti tokioje Z pozicijoje, kurioje jie buvo ilgiausi. Svarbu paminėti, jog į kelias dalis padalintos išilginės modifikacijos buvo matuotos nuo pirmos modifikacijos pradžios iki paskutinės modifikacijos galo.

Tyrimai atskleidė papliūpų svarbą, tūrinių modifikacijų formavimui naudojant femtosekundinius impulsus ir švelnų fokusavimą (NA ~0.04). Modifikacijų FS ir SLG bandiniuose nepavyko suformuoti naudojant pavienių impulsų režimą, net naudojant smailines galias viršijančias kritinę savifokusacijos vertę. Tačiau modifikacijas pavyko suformuoti taikant papliūpų ar dvigubos papliūpos režimus. FS bandinyje prireikė bent 5-ių

subimpulsų MHz ir bent 4-ių subimpulsų GHz papliūpose. SLG stikle modifikacijų formavimui prireikė dvigubos papliūpos režimo su 20 ar daugiau impulsų.

Išilginių modifikacijų homogeniškumas buvo įvertintas tik FS bandiniuose. Tolygios modifikacijos buvo suformuotos naudojant GHz papliūpas su 8-iais ar daugiau subimpulsų. Modifikacijos buvo padalintos į kelias dalis, taikant 5-is ar mažiau subimpulsų GHz papliūpoje ar taikant MHz papliūpas. Tai parodo subimpulsų pasikartojimo dažnio ir jų skaičiaus svarbą norint suformuoti tolygias išilgines modifikacijas. Nepaisant to, subimpulsų pasikartojimo dažnio įtaka išilginiams ilgiams ir padėtims buvo minimali. Išilginiai ilgiai FS bandinyje siekė ~1.4 mm naudojant 170 μJ papliūpos energiją su 7–10 (MHz) ir 6–10 (GHz) subimpulsais papliūpose. SLG stikle ilgiausia 0.9 mm modifikacija buvo suformuota su P10N3 dvigubos papliūpos režimu naudojant 350 μJ papliūpos energiją ir 176 fs trukmės impulsus.

Tiek FS, tiek SLG atveju didesnė papliūpos energija lėmė ilgesnius išilginius ilgius. Be to, didesnė papliūpos energija leido suformuoti modifikacijas naudojant platesnį subimpulsų skaičiaus intervalą. Optimalus subimpulsų skaičiaus intervalas egzistuoja todėl, kad šiuo parametru keičiamas ir akumuliacinių ciklų skaičius ir subimpulsų energija. Didesnis subimpulsų skaičius lemia mažesnę subimpulsų energiją bei smailinę galią ir silpnesnę netiesinę sąveiką su medžiaga. Tuo metu mažesnis subimpulsų skaičius lemia mažesnį kaupiamųjų ciklų skaičių, kuris yra būtinas norint suformuoti modifikacijas.

Išilginių modifikacijų padėtis buvo matuojama tik FS stikle. Didesnė subimpulsų energija lėmė modifikacijų formavimąsi arčiau viršutinio bandinio paviršiaus. Parodyta, jog modifikacijų priekio padėtis gali būti tiksliai (su 10% paklaidomis) apskaičiuota su subimpulsų energija naudojant Dawes'o ir Marburger'io ir lešio formules.

Skersiniai kampai priklausė nuo tiesinės poliarizacijos arba pluošto asimetriškumo, priklausomai nuo subimpulsų energijos. Modifikacijos formavosi pagal (FS) arba statmenai (SLG) tiesinės poliarizacijos naudojant mažas subimpulsų energijas. Padidinus subimpulsų energiją, modifikacijos ėmė krypti link -45°. Toks kampas atitiko pluošto elipsės ilgosios ašies orientaciją virš sąsmaukos pozicijos, išmatuotą mažos energijos pluoštui. Modifikacijos suformuotos su MHz papliūpomis išsiskyrė nuo kitų, kadangi didinant subimpulsų energiją virš 10 μJ , modifikacijos ėmė vėl krypti link tiesinės poliarizacijos.

Skersinių ilgių priklausomybė nuo Z pozicijos buvo išmatuota modifikacijoms suformuotoms FS bandinyje naudojant P10N1 ir P1N10 režimus. Su didesnėmis papliūpos energijomis suformuotų skersinių

modifikacijų kryptis Z ašyje priklausė tiek nuo pluošto, tiek nuo poliarizacijos. Modifikacijų priekyje (arčiau viršutinio paviršiaus) skersiniai kampai sutapo su pluoštu, o modifikacijos pabaigoje (arčiau apatinio paviršiaus) skersiniai kampai sutapo su tiesinės poliarizacijos kampu. Skersiniai kampai išliko panašūs naudojant poliarizaciją orientuotą paraleliai pluošto. Modifikacijų, suformuotų su mažesne papliūpos energija, skersiniai kampai sutapo su tiesine poliarizacija ir skirtingame gylyje išlaikė panašią kryptį. Skersiniai ilgiai skirtingose Z pozicijose išliko panašūs, kai modifikacijos buvo formuojamos naudojant mažą papliūpos energiją ir poliarizaciją, nukreiptą 45 deg arba didesniu kampu nuo pluošto elipsės ilgosios ašies.

Daugeliu atvejų skersinės modifikacijos pailgėjo, kai buvo padidinta papliūpos energija ir padidintas subimpulsų skaičius iki 10 (FS) ar 50 (SLG). Verta paminėti, jog didesnis subimpulsų skaičius taip pat lėmė skersinių modifikacijų pokytį iš vienakrypčių į chaotiškas. FS bandiniuose, naudojant GHz papliūpas pavyko suformuoti 46 μm skersinius ilgius – tai 1.7 karto ilgesnės modifikacijos nei naudojant MHz papliūpas. SLG stikle, naudojant P10N10 režimą su 176 fs trukmės impulsais ir 350 μJ papliūpos energija, pavyko suformuoti 114 μm skersinius ilgius.

Impulsų trukmės poveikis ištirtas modifikacijoms suformuotoms SLG bandiniuose su P10N5 režimu. Didėjant subimpulsų trukmei nuo kelių šimtų femtosekundžių iki pikosekundžių, vienakryptės modifikacijos tapo chaotiškomis. Didesnė papliūpos energija ir trumpesnė subimpulsų trukmė lėmė ilgesnes skersines ir išilgines modifikacijų dimensijas. Su 176 fs trukmės subimpulsais ir 350 μJ papliūpos energija pavyko suformuoti modifikacijas su skersiniais ir išilginiais ilgiais siekiančiais atitinkamai 90 μm ir 840 μm.

Kalcio-natrio silikatinio stiklo raižymas

Raižymo eksperimentai atlikti 76 x 25 x 1.1 mm³ SLG bandiniuose naudojant P10N5 režimą su 100 kHz papliūpų pasikartojimo dažniu. Pradžioje, į tam tikrą gylį sufokusuotas pluoštas buvo skenuojamas linija lygiagrečia 25 mm kraštinei. Antrame žingsnyje atliekamas bandinių atskyrimas 4-ių taškų lenkimo sistema. Laužiamas paviršius identifikuojamas kaip tas, kuriam su lenkimo sistema suformuojami tempiamieji įtempiai.

Raižymas atliktas su tiesine poliarizacija pasukta statmenai pluošto skenavimo linijos. Tokiu būdu skersinės modifikacijos orientuojamos paraleliai raižymo linijos.

Iš pradžių raižymas atliktas pluoštą sufokusavus į apatinį bandinio paviršių ir skenuojant pluoštą vieną kartą. Bandinių atskyrimas atliktas laužiant apatinį paviršių. Tyrimai atlikti naudojant skirtingą skenavimo greitį (4–10 m/s), 200 ir 300 μJ papliūpos energijas ir 176 fs, 1 ps, 2 ps ir 4 ps subimpulsų trukmes. Nepastebėta jokia viršutinio paviršiaus apskeldėjimų dydžio priklausomybė nuo skenavimo greičio ar subimpulsų trukmės. Atskirtų bandinių viršutinio paviršiaus apskeldėjimų dydis siekė iki 60 μm. Tuo metu apatinio paviršiaus apskeldėjimų dydis priklausė nuo naudojamos subimpulsų trukmės ir papliūpos energijos. Apatinio paviršiaus apskeldėjimai vidutiniškai siekė 30 μm, naudojant 300 μJ papliūpos energiją su 176 fs bei 1 ps subimpulsų trukmėmis. Ilgesnės subimpulsų trukmės bei mažesnė papliūpos energija lėmė didesnius apskeldėjimus.

Bandinių, suraižytų 6–10 m/s greičiu su 300 μ J papliūpos energija, šoniniai paviršiai buvo suformuoti iš veidrodinių ir modifikuotų zonų, kurių šiurkštumas (R_a) ir banguotumas (W_a) siekė 3.4 μ m. Bandinių, suraižytų lėtesniu 4–5 m/s greičiu, šoniniai paviršiai pasižymėjo prastesne kokybe dėl papildomai susiformavusių įstrižų pažeidimų.

Darbe ištirtas raižymas, pluošta fokusuojant į skirtinga bandinio gylį. Bandiniai buvo atskirti laužiant paviršių, esantį arčiau suformuotų modifikacijų. Tyrimai parodė, jog mažiausias bandinių atskyrimo stipris pasiekiamas, kai modifikacijos liečia laužiamą paviršių. Laužimo stipris gali būti toliau sumažintas, ilginant modifikacijos zona. Bandiniai, kuriems buvo laužiamas viršutinis paviršius pasižymėjo didesniu atskyrimo stipriu lyginant su bandiniais laužtais per apatinį paviršių. Analizuojant šoninius bandinių pastebėta, jog eksperimentu metu nepavyko paviršius. suformuoti modifikacijų liečiančių viršutinį paviršių. Tai įvyksta todėl, kad savifokusacija yra kaupiamasis procesas, dėl kurio šviesos gijos susiformuoja tik po tam tikro atstumo. Mažiausias atskyrimo stipris pasiektas raižant bandinius su pluoštu sufokusuotu i apatini bandinio paviršiu. Fokusuojant žemiau – suformuojamos trumpesnės modifikacijos, o fokusuojant aukščiau – modifikacijos neliečia apatinio paviršiaus.

Tyrimo metu pademonstruotas stabilus bandinių, raižytų 4–10 m/s greičiu, atskyrimas. Atliekant raižymą vienu skenavimu, mažiausias bandinių atskyrimo stipris (18 MPa) pasiektas naudojant 6 m/s greitį, 176 fs trukmės impulsus ir 300 μJ papliūpos energiją. Bandinių atskyrimo stipris padidėjo 1.5 karto, raižant su mažesne 200 μJ papliūpos energija. Pademonstruota, jog modifikacijų zonos ilgis gali būti padidintas, pluoštą skenuojant du kartus skirtingame gylyje. Toks raižymo metodas leido sumažinti bandinių atskyrimo stiprį iki ~12 MPa. Visgi, svarbu atkreipti dėmesį, kad tokiu būdu raižymas atliekamas dvigubai lėčiau. Bandinių raižymui dvejomis linijomis

palankiau naudoti 200μJ papliūpos energiją lyginant su 300 μJ, dėl geresnės šoninio paviršiaus kokybės.

Eksperimentiniai bandinių atskyrimo stipriai buvo palyginti su teorinėmis vertėmis gautomis su inertiniu ir subkritiniu įtrūkių formavimosi modeliais. Bandinių atskyrimo stipris atitiko teorinę kreivę – ilgesnė modifikacijų zona lėmė mažesnį bandinių atskyrimo stiprį. Bandinių, su modifikuotos zonos ilgiu siekiančiu 0.6 mm, atskyrimo stipris skyrėsi per 25% nuo inertinio modelio. Skirtumas tarp eksperimentinių ir teorinių verčių padidėjo, kai buvo vertinami bandiniai su ilgesne modifikacijos zona.

Lyginant su kitais darbais, šiame darbe pademonstruotas didžiausias stiklo pjovimo greitis, tiesinis bei santykinis efektyvumai.

Pagrindiniai rezultatai ir išvada

Pirmasis ginamasis teiginys suformuluotas šių rezultatų pagrindu:

- Naudojant 1030 nm bangos ilgio pikosekundinių impulsų GHz papliūpas galima pasiekti greitą (4.2 mm/s) ir efektyvų (0.13 mm/J)
 4.8 mm storio kalcio-natrio silikatinio stiklo (SLG) pjovimą dėl medžiagos pašalinimo skaldant.
- Greitas pjovimo režimas pasižymi prasta bandinių kokybe. Vidutinis šoninio paviršiaus šiurkštumas R_a siekė 2.3 μm, o maksimalių apskeldėjimų ant viršutinio ir apatinio paviršių vidurkiai siekė atitinkamai 400 μm ir 90 μm.
- 3. Keičiant apdirbimo parametrus tam pačiam kalcio-natrio silikatinio stiklo bandiniui buvo pritaikyti ir spartaus ir aukštos kokybės režimai. Didelio našumo režimas, pasiektas naudojant didesnį subimpulsų papliūpoje skaičių, leido greitai išpjauti bandinį, o 300 μm pločio nuožulnos, suformuotos aukštos kokybės režimais, pasiektais naudojant mažesnį subimpulsų skaičių papliūpoje, leido pašalinti piovimo metu susidariusius apskeldėjimus.

Antrasis ginamasis teiginys suformuluotas šių rezultatų pagrindu:

4. Papliūpos ir dvigubos papliūpos režimai leidžia suformuoti pailgas modifikacijas su skersiniais matmenimis lydyto kvarco (FS) bei SLG tūriuose, naudojant femtosekundinius impulsus ir švelnų fokusavimą

(NA ~0.04). Modifikacijos nebuvo pastebėtos, taikant klasikinį pavieniu impulsu režima tomis pačiomis salygomis.

- Tiek FS, tiek SLG, ilgesni skersiniai ir išilginiai ilgiai buvo suformuoti naudojant didesnę papliūpų energiją, išskyrus tuos atvejus, kai buvo pažeidžiamas viršutinis paviršius. Išilginiai ilgiai siekė 1.4 mm (FS) ir 0.9 mm (SLG), o skersiniai ilgiai siekė 46 μm (FS) ir 114 μm (SLG).
- 6. Priklausomai nuo subimpulsų energijos, skersinių modifikacijų kampas priklausė nuo tiesinės poliarizacijos arba pluošto eliptiškumo, apibūdinant modifikacijas Z pozicijoje, atitinkančioje ilgiausias skersinės modifikacijas. Naudojant mažas subimpulsų energijas, skersinės modifikacijos buvo orientuotos paraleliai (FS) arba statmenai (SLG) poliarizacijos. Didėjant subimpulsų energijai, skersinės modifikacijos ėmė krypti link pluošto elipsės ilgosios ašies. Išimtiniu atveju, kai FS bandinyje modifikacijos buvo formuotos naudojant MHz papliūpas, skersinės modifikacijos ėmė vėl krypti link poliarizacijos, padidinus subimpulsų energiją virš 10 μJ.
- 7. Modifikacijų, suformuotų FS su P10N1 ir P1N10 papliūpų režimais, naudojant didesnę papliūpų energiją, skersiniai kampai priklausė nuo Z pozicijos. Modifikacijų skersiniai kampai atitiko pluošto kryptį priekyje ir poliarizacijos kryptį modifikacijos gale. Skersinių modifikacijų kryptis skirtingame gylyje išliko pastovi, kai modifikacijos buvo formuojamos poliarizacija valdomais režimais arba orientuojant poliarizaciją pagal pluoštą.

Trečiasis ginamasis teiginys suformuluotas šių rezultatų pagrindu:

8. Stabilus 1.1 mm storio SLG bandinių, suraižytų 4–10 m/s greičiu, atskyrimas buvo pasiektas, formuojant modifikacijas šviesos gijomis su P10N5 dvigubos papliūpos režimu, 100 kHz papliūpų pasikartojimo dažniu ir 0.04 skaitine apertūra. Mūsų žiniomis tai greičiausias iki šiol pademonstruotas stiklo raižymas. Tokį greitį pavyko pasiekti skersines modifikacijas orientuojant pagal raižymo liniją, nustatant poliarizaciją statmenai jai.

Pagrindinė išvada:

9. Lazeriai su ultratrumpų impulsų GHz papliūpomis suteikia išskirtinį lankstumą stiklo pjovimui nuo apatinės pusės, kadangi subimpulsų skaičius papliūpoje daro įtaką proceso efektyvumui, spartai ir kokybei. GHz papliūpų režimas leidžia dinamiškai keisti subimpulsų skaičių apdirbimo metu, taip leidžiant skirtingas bandinio vietas apdirbti arba aukštos kokybės arba didelio našumo režimu. Tas pats lazerinis šaltinis gali būti naudojamas formuojant poliarizacija valdomas modifikacijas šviesos gijomis, kurios gali būti taikomos raižymui, pasiekiant iki 10 m/s greitį 1.1 mm storio SLG stikle. Tos pačios sistemos pritaikymas stiklo raižymui šviesos gijomis ir pjovimui nuo apatinės pusės parodo unikalų ultratrumpų impulsų GHz papliūpų lazerių lankstumą stiklo apdirbimo taikymams.

PADĖKA

Visų pirma noriu padėkoti Juozui, Pauliui ir Gediminui už galimybę dirbti laboratorijoje. Mentorių Juozo ir Pauliaus pastabos ir komentarai lydėjo kiekvieną mano darbą ir padarė didžiausią įtaką man kaip jaunajai mokslininkei. Ačiū stalo kaimynams Modestui ir Laimiui, kurie stipriai palengvino doktorantūros ir magistrantūros studijas. Ačiū Aleksandrui, prisidėjusiam prie dalies eksperimentų. Ačiū Vidmantui, Gediminui ir Valdui parodžiusiems dujinių purkštukų virtuvę. Džiaugiuosi, jog turėjau galimybę detaliau susipažinti su šia sritimi.

Už malonią darbo aplinką dėkoju kolegoms Edgarui, Arnui, Valdemarui, Andriui, Rodrigui, Mantui, Simui, Evaldui, Mindaugui, Kerniui, Vitai, Romualdui ir Karoliui. Ačiū Augustinui ir Saulei, rimčiausiems stalo teniso varžovams. Taip pat noriu padėkoti draugams, kurie netiesiogiai prisidėjo prie šios disertacijos atsiradimo. Nevardinsiu, bet, drauge, jeigu skaitai – čia apie tave.

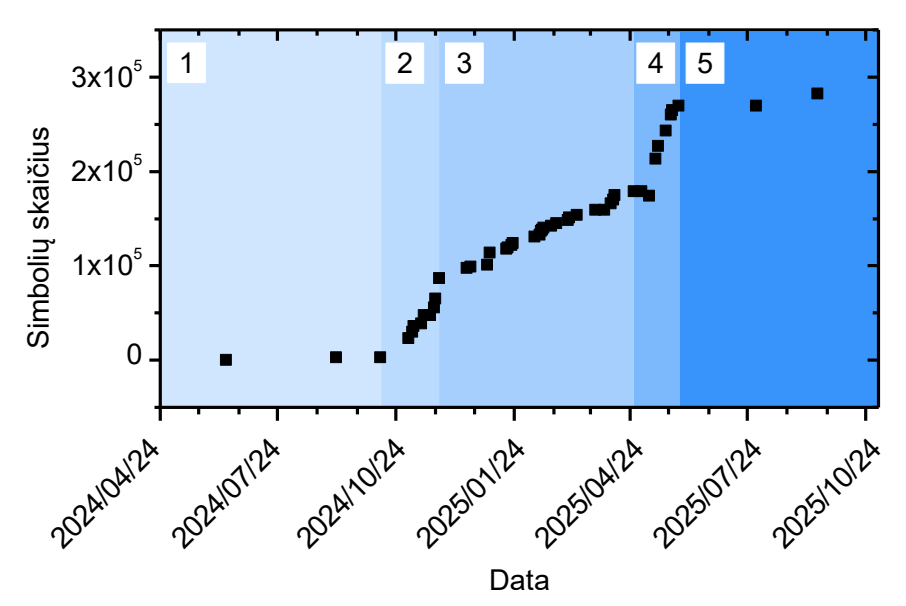
Ačiū tėvams ir Domui už visapusišką palaikymą.

Disertacijos rašymas

Disertacijos rašymas užtruko ilgiau nei metus. Norėdama pamatyti progresą ir nepamesti motyvacijos, žymėjausi atliktus darbus bei parašytų simbolių skaičių (įskaitant tarpus). Todėl galima išanalizuoti duomenis ir pasižiūrėti kaipgi man sekėsi rašyti.

Disertacijos simbolių skaičiaus priklausomybė nuo laiko yra pateikta 1 paveiksle. Galima išskirti penkis rašymo etapus. Pirmajame rašymo etape buvo suformuotas planas, išsikelti darbo tikslai. Pirmas etapas užtruko 4 mėnesius, o rašymo sparta siekė 27 sym/d. Su tokia sparta, minimalus disertacijos simbolių skaičius (160 tūkst.) būtų pasiektas per maždaug 16 metų. Išvada: reikėjo pasitempti ir iš tikrųjų pradėti rašyti. Antrajame etape buvo aprašomi eksperimentiniai duomenys. Tai vienas iš sparčiausių etapų, nes per 45 dienas simbolių skaičius pakilo iki 87 tūkst. (1580 sym/d). Po šio smagaus etapo reikėjo pereiti prie 3-iojo etapo – teorijos. Tamsusis etapas truko 130 dienų, su 621 sym/d sparta. 4-ajame etape buvo pridėtas literatūros šaltinių sąrašas, rašoma santrauka lietuvių kalba, atliekami paskutiniai pataisymai prieš darbo siuntimą recenzentams. Nuo to laiko, kai pridėjau literatūros šaltinių sąrašą, kompiuteris ėmė strigti. Apie mėnesį trukęs 4-asis etapas pasižymėjo didele 3166 sym/d sparta. Paskutinis 5-asis etapas truko

apie 3 mėnesius. Jo metu buvo atsižvelgiama į recenzentų pastabas. Kadangi šiame etape buvo daugiau taisymo nei rašymo – sparta tebuvo 109 sym/d. Tai tokia buvo mano rašymo istorija. Ačiū, kad skaitėt ir iki kitų kartų!



1 pav. Disertacijos simbolių skaičiaus kitimas laike. Skirtingi rašymo etapai išskirti skaičiais ir mėlynais atspalviais. Kiekviename etape simbolių skaičius buvo aproksimuotas tiesiškai, norint nustatyti vidutinį parašytų simbolių skaičių per dieną (sym/d).

CURRICULUM VITAE

Name: Miglė

Surname: Mackevičiūtė

Place of birth: Panevėžys, Lithuania

E-mail: migle.mackeviciute@ftmc.lt

Education

2021 - now	Center for Physical Sciences and Technology
	PhD studies in Materials Engineering
2019 - 2021	Vilnius University
	Master's degree in Materials Technology
2015 - 2019	Vilnius University
	Bachelor's degree in Physics
2011 - 2015	Juozas Balčikonis gymnasium

Juozas Balčikonis gymnasium High school education

Work experience

2022 - now	Center for Physical Sciences and Technology
	Junior researcher
2019 - 2022	Center for Physical Sciences and Technology
	Engineer
2017 - 2020	Altechna
	Metrologist

NOTES

NOTES

Vilniaus universiteto leidykla Saulėtekio al. 9, III rūmai, LT-10222 Vilnius El. p. info@leidykla.vu.lt, www.leidykla.vu.lt bookshop.vu.lt, journals.vu.lt Tiražas 20 egz.